Design and testing of a high through flow fan for a high altitude application

Master Thesis

Author(s):
Shahin, Hosam

Publication date:
2007

Permanent link:
https://doi.org/10.3929/ethz-a-006100540

Eidgenössische Technische Hochschule Zürich
Swiss Federal Institute of Technology Zurich

Hosam Shahin

Design and Testing of a High Through Flow Fan for a High Altitude Application

Master Thesis

Institute of Energy and Technology - Turbomachinery Laboratory
Swiss Federal Institute of Technology (ETH) Zurich

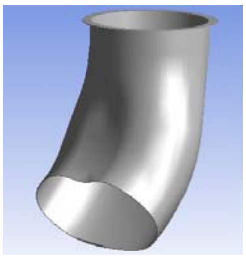

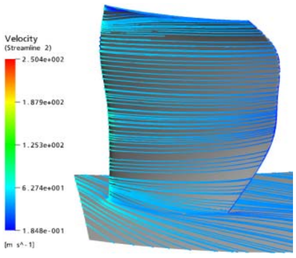

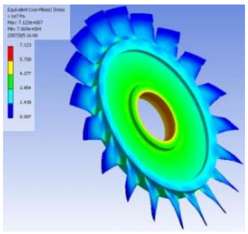

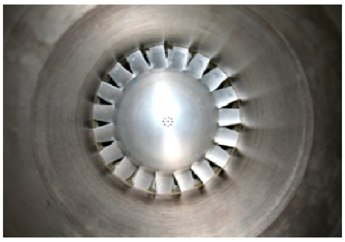

Supervision

Behnam H. Beheshti
Prof. Dr. Reza S. Abhari

October 2007

Proposal

Design and Testing of a High-Through Flow Fan for High-Altitude Applications

During a long duration stratospheric flight, high altitude airships should be able to endure a high temperature rise and a volume increase up to 100% if no cooling system is applied. In a novel design for a high altitude airship with dual blimps, an accurate temperature control would be achievable if cold ambient air is pumped between the outer and the inner layers. Calculation for a full size airship indicates that an appropriate temperature control requires two axial fans each providing a 0.6 kg/s air mass flow rate (equivalent to 7.5 m^3/s). The pressure ratio should be kept as low as possible (1.02 - 1.05) to avoid damages of the blimps. The current project is focused on design and manufacturing of a high through flow axial fan with a low pressure ratio for a high altitude application. This project includes the following goals:

1. Aerodynamic design of a single stage axial fan (rotor and stator)
2. CFD simulation and optimization of the designed fan
3. Thermo-mechanical and vibration analysis
4. Design of inlet and outlet ducts for the axial fan
5. Design of a mechanism for integration of the fan into the airship
6. Manufacturing and testing of a small scale model

Based on the results of this thesis, two full-scale fans will be manufactured and integrated to the airship for a real flight.

Contact:
Dr. Behnam H. Beheshti
044 632 86 94
behnamh@ethz.ch

Abstract

The global interest in using lighter-than-air ships for extended operation at near space, 18 to 100 km (59,000 to 328,000 feet) above the sea level, is growing extensively. Near space altitudes are higher than that at which most airplanes fly but lower than that of satellite orbits. Although near-space flight is potentially less expensive and more flexible than space-based flight, except for a relatively brief time, near space altitudes remain mostly unused, due to the poor performance of aeronautical systems at these altitudes. However, a High Altitude Airship (HAA) in near space can remain stationary over a ground target area and can provide the possibility of continuous coverage, thereby fulfilling the needs of many civil and military missions heretofore accomplished using satellites. Near-space airships are now more feasible due to recent advances in lightweight materials and solar-power technology. Nevertheless, to-date, no near-space vehicle has demonstrated the capability of remaining in the air for a one-year duration. Although a near-space vehicle is above meteorological phenomena such as cloud, rain and storm, the prevailing winds can have a profound impact on the vehicle's performance. Metrological data show that at altitudes of 20 to 21 km (65,000 to 69,000 ft) the wind speed is relatively low, less than 7 m/s during summer time, and thus most HAAs are designed for operation at these altitudes.

The ability to remain stationary in the presence of variable winds is one of the primary technical challenges for modern HAA. Many near-space systems use a solar-electric-based propulsion system (i.e. propellers driven by electric motors). For economic operation in long duration flight, it is critical to minimize the propulsive power requirements for station keeping. In a novel design for a high altitude airship with dual blimps, an accurate temperature control would be achievable if cold ambient air is pumped between the outer and the inner layers. Calculation for a full size airship indicates that an appropriate temperature control requires two axial fans each providing a 0.6 kg/s air mass flow rate (equivalent to 7.5 m^3/s). The pressure ratio should be kept as low as possible (1.02-1.05) to avoid damages of the blimps.

The purpose of the present work is to design and manufacture a high through flow axial fan with a low pressure ratio for a high altitude application and to design an efficient and aerodynamic compressor inlet duct. This HAA is

under development for commercial telecommunications applications, and is envisaged to operate at an altitude of 21 km for a year. In this study, the focus is on the compressor development as well as on the effect of wind (speed and direction) on the compressor inlet duct. The approach in the present work is computational and experimental. CFD is used to model the flow field through the bent inlet duct and compressor separately, and to predict the compressor performance. A bent compressor inlet duct is considered in order to profit from the available wind speeds at high altitudes to lower the power consumption and to prevent the fan from stalling. Data from experiments in a test facility for a manufactured fan model are used to assess the CFD methodology and to validate the compressor performance.

Acknowledgments

I would like to express my sincere thanks to Prof. Dr. Reza S. Abhari, head of the Turbomachinery Laboratory at the Swiss Federal Institute of Technology (ETH) Zurich for supervising this thesis, for his suggestions and for giving me the opportunity to work on an exciting and challenging topic. I also want to thank him for giving me previously the possibility to work together with Michel Mansour and Christian Lenherr as a Junior Lab Assistant. All together, this was a tremendous learning.

I feel deeply grateful to my supervisor Behnam Beheshti for his support and his strong engagement during the whole period, the constructive discussions and always accessible guidance. His exemplary way of assistance and his friendly nature made such an enjoyable and salutary time at the institute possible.
Furthermore, I would like to sincerely thank Albert Kammerer and Thomas Behr for all their efforts, support and the discussions throughout the whole period and especially during the experimental phase. With their expert knowledge in turbomachinery and machining they were a great help while designing, drafting and manufacturing. Their scientific way of solving disparate problems allowed me to learn a lot. Without their advice, suggestions and guidance, this work would not have been possible in such a short time frame.

I had the chance to have access to a very precious source of knowledge and experience. I feel deeply thankful to André Burdet for all his support and guidance as well as for all the personal discussions and all the excellent advise.

Special thanks go to Thomas Künzle, who manufactured every single piece of the test rig with great commitment and precision. He has a profound knowledge in machining and brilliant ideas for solving technical issues. It was a pleasure to work with him. Also, I would like to thank Christoph Räber for his advice and all suggestions as well as Armin Zemp for his support while testing.

I would like to express my gratitude to all members of the LSM for their friendliness and support. Many thanks to the following people who advised me during work: Martin Bruderer, Bob Mischo, Christian Lenherr, Michel Mansour, Cornel Reshef, Bob Rollinger and Luca Porreca.

Specially, I would like to thank Marlene Hegner for all her excellent advice and help in all sort of issues.

I also want to thank Niklaus Güpfert and Fabian Wittmer for their loyal fellowship throughout the whole thesis, the very nice breaks and discussions.

Finally, I would like to express my thanks to my parents, Sayed and Aaysha Shahin, to my brother Ramzy, to Hagar Mahmoud and to my best friends, David Paz, Andreas Trottmann and Akram Abdellatif for their understanding, patience and support.

Hosam Shahin
Zurich, October 2007

Table of Contents

Appendices

List of Figures

Chapter 1

Introduction

1.1 Objectives and Approach

The global interest in using lighter-than-air ships for extended operation at near space, 18 to 100 km (59,000 to 328,000 feet) above the sea level, is growing extensively. Near space altitudes are higher than that at which most airplanes fly but lower than that of satellite orbits. Although near-space flight is potentially less expensive and more flexible than space-based flight, except for a relatively brief time, near space altitudes remain mostly unused, due to the poor performance of aeronautical systems at these altitudes. However, a High Altitude Airship (HAA) in near space can remain stationary over a ground target area and can provide the possibility of continuous coverage, thereby fulfilling the needs of many civil and military missions heretofore accomplished using satellites. Near-space airships are now more feasible due to recent advances in lightweight materials and solar-power technology. Nevertheless, to-date, no near-space vehicle has demonstrated the capability of remaining in the air for one-year duration. Although a near-space vehicle is above meteorological phenomena such as cloud, rain and storm, the prevailing winds can have a profound impact on the vehicle's performance. Metrological data show that at altitudes of 20 to 21 km (65,000 to 69,000 ft) the wind speed is relatively low, less than 7 m/s during summer time, and thus most HAAs are designed for operation at these altitudes.

The ability to remain stationary in the presence of variable winds is one of the primary technical challenges for modern HAA. Many near-space systems use a solar-electric-based propulsion system (i.e. propellers driven by electric motors). For economic operation in long duration flight, it is critical to minimize the propulsive power requirements for station keeping. In a novel design for a high altitude airship with dual blimps, an accurate temperature control would be achievable if cold ambient air is pumped between the outer and the inner layers. Calculation for a full size airship indicates that an appropriate temperature control requires two axial fans each providing a 0.6 kg/s air mass flow rate (equivalent to 7.5 m^3/s). The pressure ratio should be kept as low as possible (1.02-1.05) to avoid damages of the blimps.

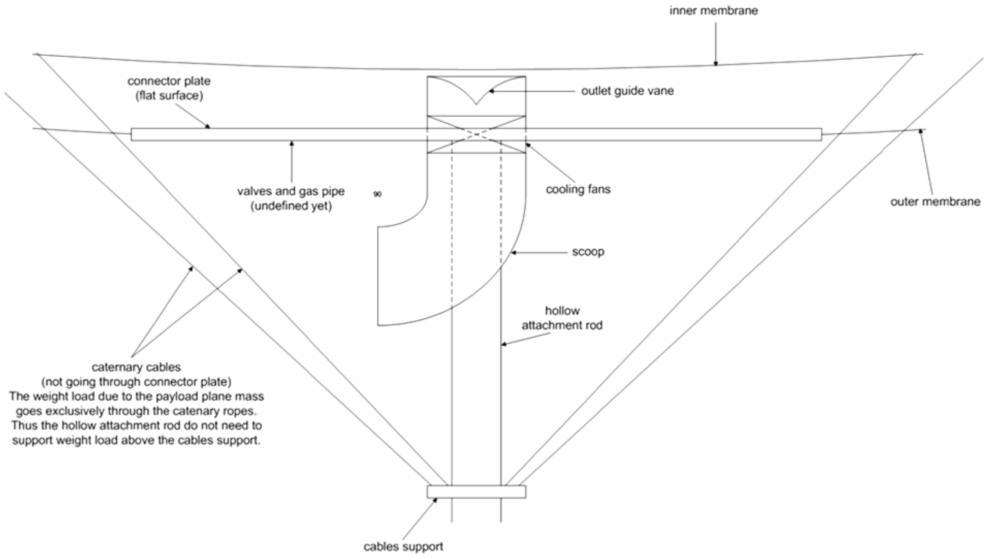

Fig. 1.1 Dual Blimp HAA, where the cooling Fans are carried by a supportive plate.

A possible design of such a dual blimp HAA is shown in Fig. 1.1, where the fans are attached to a supportive plate. A bent compressor inlet duct is considered in order to profit from the available wind speeds at high altitudes to lower the power consumption and to prevent the fan from stalling.

The purpose of the present work is to design and manufacture a high through flow axial fan with a low pressure ratio for a high altitude application and to design an efficient and aerodynamic compressor inlet duct. This HAA is under development for commercial telecommunications applications, and is envisaged to operate at an altitude of 21 km for a year. In this study, the focus is on the compressor development as well as on the effect of wind (speed and direction) on the compressor inlet duct. The approach in the present work is computational and experimental. CFD is used to model the flow field through the bent inlet duct and compressor separately, and to predict the compressor performance. Data from experiments in a test facility for a manufactured fan model are used to assess the CFD methodology and to validate the compressor performance. In the following, the CFD analysis is first presented. Then the experimental facility is described. The results of the computational and experimental study of the compressor are presented in each chapter and finally, the conclusions are summarized.

Chapter 2

Theoretical Background

2.1 Axial Flow Compressors and Fans

As turbomachines classified are all devices in which energy is transferred either to, or from, a continuously flowing fluid by the dynamic action of one or more moving blade rows. The word turbo or turbinis is of Latin origin and implies that which spins or whirls around. Essentially, a rotating blade row, a rotor or an impeller changes the stagnation enthalpy of the fluid moving through it by either doing positive or negative work, depending upon the effect required of the machine. These enthalpy changes are intimately linked with the pressure changes occurring simultaneously in the fluid.

Two main categories of turbomachine are identified: firstly, those which absorb power to increase the fluid pressure or head (ducted fans, compressors and pumps);

secondly, those that produce power by expanding fluid to a lower pressure or head (hydraulic, steam and gas turbines).

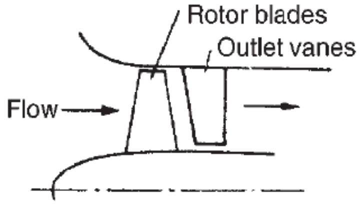

(a) Single stage axial flow compressor or pump

Fig. 2.1 Single Stage Axial Flow Compressor (Dixon, 1998).

Most of the pressure increasing turbomachines in use are of the radial-flow type and vary from fans that produce pressure rises equivalent to a few millimetres of water to pumps producing heads of many hundreds of meters of water. The term pump is used when referring to machines that increase the pressure of a flowing liquid. The term fan is used for machines imparting only a small increase in pressure to a flowing gas as shown in Fig. 2.1. In this case the pressure rise is usually so small that the gas can be considered as being incompressible.

A compressor gives a substantial rise in pressure to a flowing gas. For purposes of definitions, the boundary between fans and compressors is often taken as that where the density ratio across the machine is 1.05. Sometimes, but more rarely, the term blower is used instead of fan.

2.1.1 Moment of Momentum

In dynamics much useful information is obtained by employing Newton's second law in the form where it applies to the moments of forces. This form is of central importance in the analysis of the energy transfer process in turbomachines.

For a system of mass *m*, the vector sum of the moments of all external forces acting on the system about some arbitrary axis *A-A* fixed in space is equal to the time rate of change of angular momentum of the system about that axis, i.e.

$$\tau_A = m\frac{d}{dt}(rc_\theta), \tag{Eq. 2.1}$$

where *r* is distance of the mass centre from the axis of rotation measured along the normal to the axis and c_θ the velocity component mutually perpendicular to both the axis and radius vector r.

For a control volume the law of moment of momentum can be obtained. Fig. 2.2 shows the control volume enclosing the rotor of a generalised turbomachine. Swirling fluid enters the control volume at radius r_1 with tangential velocity $c_{\theta 1}$ and leaves at radius r_2 with tangential velocity $c_{\theta 2}$. For one-dimensional steady flow

$$\tau_A = \dot{m}(r_2 c_{\theta 2} - r_1 c_{\theta 1}), \tag{Eq. 2.2}$$

which states that, the sum of the moments of the external forces acting on the fluid temporarily occupying the control volume is equal to the net time rate of efflux of angular momentum from the control volume.

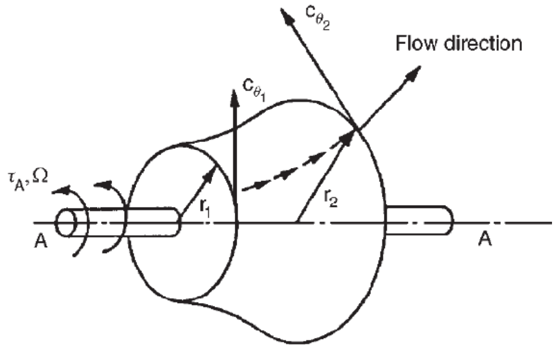

Fig. 2.2 Control Volume for a generalised Turbomachine (Dixon, 1998).

2.1.2 Euler's Pump Equations

For a compressor rotor running at angular velocity Ω, the rate at which the rotor does work on the fluid is

$$\tau_A = \dot{m}(U_2 c_{\theta 2} - U_1 c_{\theta 1}), \qquad \text{(Eq. 2.3)}$$

where the blade speed $U = \Omega r$.
Thus the work done on the fluid per unit mass or specific work, is

$$\Delta W_c = \frac{\dot{W}_c}{\dot{m}} = \frac{\tau_A \Omega}{\dot{m}} = U_2 c_{\theta 2} - U_1 c_{\theta 1} > 0. \qquad \text{(Eq. 2.4)}$$

This equation is referred to as the *Euler's Pump Equation*.

2.1.3 Rothalpy

In a compressor, the specific work done on the fluid equals the rise in stagnation enthalpy. Thus, combining equations (2.8) and (2.12a) yields

$$\Delta W_c = \frac{\dot{W}_c}{\dot{m}} = U_2 c_{\theta 2} - U_1 c_{\theta 1} = h_{02} - h_{01}. \qquad \text{(Eq. 2.5)}$$

This relationship is true for steady, adiabatic and irreversible flow. After rearranging of Eq. (2.5) and writing $h = h_0 + \frac{1}{2}c^2$, results

$$h_1 + \frac{1}{2}c_1^2 - U_1 c_{\theta 1} = h_2 + \frac{1}{2}c_2^2 - U_2 c_{\theta 2} = I \qquad \text{(Eq. 2.6)}$$

According to the above reasoning a new function *I* has been defined having the same value at exit from the impeller as at entry. The function *I* has acquired the widely used name rothalpy, a contraction of rotational stagnation enthalpy, and is a fluid mechanical property of importance in the study of relative flows in rotating systems. As the value of rothalpy is apparently unchanged between entry and exit of the impeller, it is deduced that it must be constant along the flow lines between these two stations. Thus, the rothalpy can be written generally as

$$I = h + \frac{1}{2}c^2 - U c_\theta. \qquad \text{(Eq. 2.7)}$$

The same reasoning can be applied to the thermo mechanical flow through a turbine with the same result.

2.1.4 Velocity Diagrams of a Compressor Stage

The velocity diagrams for a stage are given in Fig. 2.3. The convention is adopted throughout this chapter of accepting all angles and swirl velocities in this figure as positive. As for axial turbine stages, a “normal” compressor stage is one where the absolute velocities and flow directions at stage outlet are the same as at stage inlet. The flow from a previous stage (or from the guide vanes) has a velocity c_1 and direction α_1. Subtracting vectorially the blade speed U gives the inlet relative velocity w1 at angle β_1 (the axial direction is the datum for all angles). Relative to the blades of the rotor, the flow is turned to the direction β_2 at outlet with a relative velocity w_2. Clearly, by adding vectorially the blade speed U on to w_2 gives the absolute velocity from the rotor, c_2 at angle α_2. The stator blades deflect the flow towards the axis and the exit velocity is c_3 at angle α_3. For the normal stage $c_3 = c_1$ and $\alpha_3 = \alpha_1$. As drawn in Fig. 2.3, both the relative velocity in the rotor and the absolute velocity in the stator are diffused. The relative amount of diffusion of kinetic energy in the rotor and stator rows significantly influences the stage efficiency.

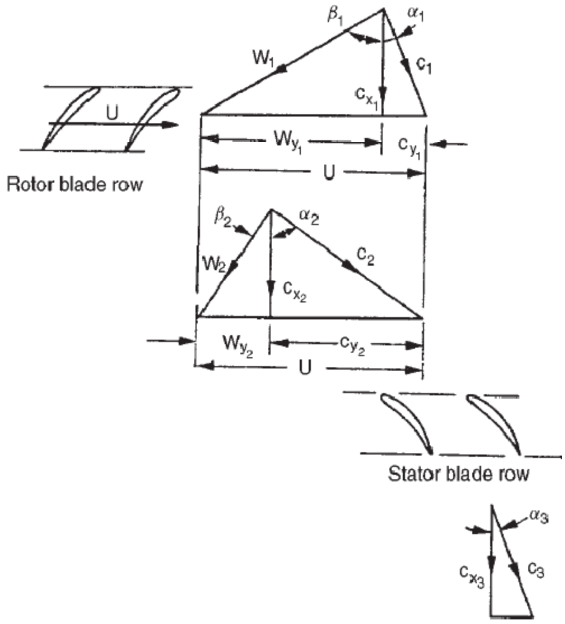

Fig. 2.3 Velocity Diagrams for a Compressor Stage (Dixon, 1998).

2.1.5 Thermodynamics of a Compressor Stage

The specific work done by the rotor on the fluid, from the steady flow energy equation (assuming adiabatic flow) and momentum equation is

$$\Delta W_c = \frac{\dot{W}_c}{\dot{m}} = h_{02} - h_{01} = U(c_{\theta 2} - c_{\theta 1}). \qquad \text{(Eq. 2.8)}$$

For all axial turbomachines

$$h_{0rel} = h + \frac{1}{2}w^2 \qquad \text{(Eq. 2.9)}$$

is constant in the rotor, therefore

$$h_1 + \frac{1}{2}w_1^2 = h_2 + \frac{1}{2}w_2^2 \qquad \text{(Eq. 2.10)}$$

This is valid, as long there is no radial shift of the streamlines across the rotor (i.e. $U_1 = U_2$.

Across the stator, h_0 is constant, and

$$h_2 + \frac{1}{2}c_2^2 = h_3 + \frac{1}{2}c_3^2. \qquad \text{(Eq. 2.11)}$$

The compression process for the complete stage is represented on a Mollier diagram in Fig. 2.4, which is generalised to include the effects of irreversibility.

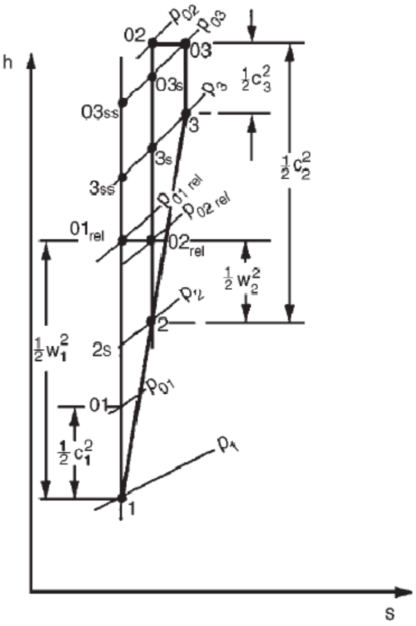

Fig. 2.4 Mollier Diagram for an Axial Compressor Stage (Dixon, 1998).

2.1.6 Reaction Ratio

For the case of incompressible and reversible flow it is permissible to define the reaction *R*, as the ratio of static pressure rise in the rotor to the static pressure rise in the stage

$$R = \frac{(p_2 - p_1)}{(p_3 - p_1)}. \qquad \text{(Eq. 2.12)}$$

If the flow is both compressible and irreversible a more general definition of *R* is the ratio of the rotor static enthalpy rise to the stage static enthalpy rise,

$$R = \frac{(h_2 - h_1)}{(h_3 - h_1)}. \qquad \text{(Eq. 2.13)}$$

Or expressed in angles,

$$R = \frac{1}{2} + \frac{(tan\beta_2 - tan\alpha_1)c_x}{2U}. \qquad \text{(Eq. 2.14)}$$

Choice of Reaction

The reaction ratio is a design parameter which has an important influence on stage efficiency. Stages having 50% reaction are widely used as the adverse (retarding) pressure gradient through the rotor and stator rows is equally shared. This choice of reaction minimises the tendency of the blade boundary layers to separate from the solid surfaces, thus avoiding large stagnation pressure losses.
If $R = 0.5$ then $\alpha_1 = \beta_2$ (Eq. 2.14), and the velocity diagram is symmetrical. The stage enthalpy rise is equally distributed between the rotor and stator rows.

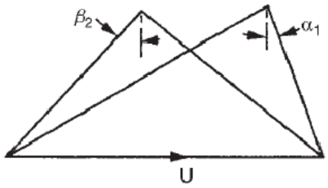

(a) R > 50%
$\beta_2 > \alpha_1$

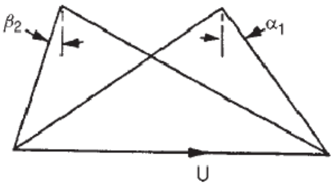

(a) R < 50%
$\beta_2 < \alpha_1$

Fig. 2.5 Asymmetry of Velocity Diagrams for Reactions greater or less than 50% (Dixon, 1998).

If $R > 0.5$ then $\alpha_1 < \beta_2$ and the velocity diagram is skewed to the right as shown in Fig. 2.5a. The static enthalpy rise in the rotor exceeds that in the stator (this is also true for the static pressure rise).
If $R < 0.5$ then $\alpha_1 > \beta_2$and the velocity diagram is skewed to the left as indicated in Fig. 2.5b. Clearly, the stator enthalpy (and pressure) rise exceeds that in the rotor.

2.1.7 Performance of Compressors

The performance of compressible flow machines is usually described in terms of groups of variables. These characteristics are dependent on other variables such as the conditions of pressure and temperature at the compressor inlet and physical properties of the working fluid. To study the performance of a compressor completely, it is necessary to plot the total pressure coefficient $\pi = \frac{P_{02}}{P_{01}}$ against the mass flow parameter $\frac{\dot{m}\sqrt{T_{01}}}{P_{01}}$ for fixed speed intervals of $\frac{N}{\sqrt{T_{01}}}$. Fig. 2.6 represents a typical performance map. Notice that the subscript 1 is used to denote conditions as inlet. One of the most striking features of these performance characteristics is the strong dependence shown by the compressor upon $\frac{N}{\sqrt{T_{01}}}$.

For the compressor, efficient operation at constant $\frac{N}{\sqrt{T_{01}}}$ lies to the right of the line marked "*surge*". The phenomenon of surge is discussed in section 2.1.8. In brief, for multistage compressors it commences approximately at the point (for constant $\frac{N}{\sqrt{T_{01}}}$) where the pressure ratio flattens out to its maximum value. The surge line denotes the limit of stable operation of a compressor, unstable operation being characterised by a severe oscillation of the mass flow rate through the machine. The choked regions of the compressor characteristics may be recognised by the vertical portions of the constant speed lines. No further increase in $\frac{\dot{m}\sqrt{T_{01}}}{P_{01}}$ is possible, since the Mach number across some section of the machine has reached unity and the flow is said to be choked.

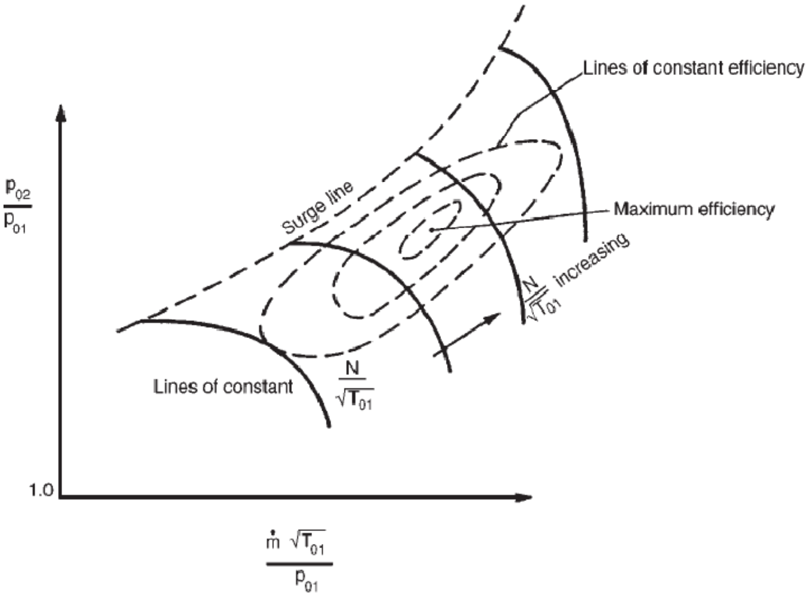

Fig. 2.6 Overall Characteristic of a Compressor (Dixon, 1998).

2.1.8 Efficiency of compressors

The isentropic efficiency η_c of a compressor is broadly defined as,

$$\eta_c = \frac{\text{useful energy input to fluid in unit time}}{\text{power input to rotor}}$$

The power input to the rotor is always less than the power supplied at the coupling because of external energy losses in the bearings and glands, etc.
Thus, the overall efficiency of the compressor or pump is

$$\eta_o = \frac{\text{useful energy input to fluid in unit time}}{\text{power input to coupling of shaft}}$$

Hence the mechanical efficiency is

$$\eta_m = \frac{\eta_o}{\eta_c} \qquad \text{(Eq. 2.15)}$$

Fig. 2.7 shows a Mollier diagram on which the actual compression process is represented by the state change 1 - 2 and the corresponding ideal process by 1 - 2s. For an adiabatic compressor the only meaningful efficiency is the total-to-total efficiency which is

$$\eta_c = \frac{\text{minimal adiabatic work input per unit time}}{\text{actual adiabatic work input to rotor per unit time}} = \frac{h_{02s} - h_{01}}{h_{02} - h_{01}} \qquad \text{(Eq. 2.16)}$$

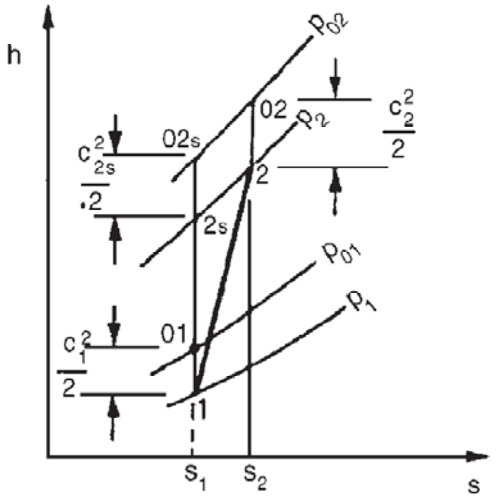

Fig. 2.7 Compression Process (Dixon, 1998).

2.1.9 The Inherent Unsteadiness of the Flow within Turbomachines

Turbomachines can only work the way they do because of unsteady flow effects taking place within them. The fluid dynamic phenomena that are associated with the unsteady flow in turbomachines have been examined by Greitzer (1986). Basically Greitzer, and others before him, in considering the fluid mechanical process taking place on a fluid particle in an isentropic flow, deduced that stagnation enthalpy of the particle can change only if the flow is unsteady. Dean (1959) appears to have been the first to record that without an unsteady flow inside a turbomachine, no work transfer can take place. Paradoxically, both at the inlet to and outlet from the machine the conditions are such that the flow can be considered as steady.

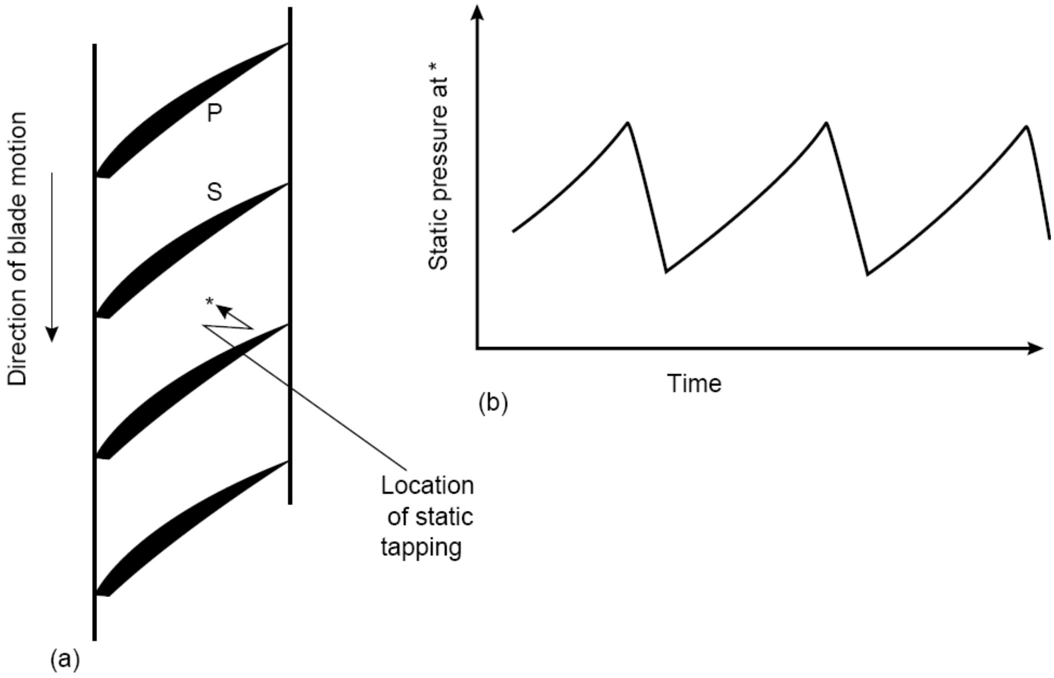

Fig. 2.8 Measuring Unsteady Pressure Field of an Axial Compressor Rotor. (a) Pressure is measured at Point * on the Casing. (b) Fluctuating Pressure measured at Point * (Dixon, 1998).

A physical situation considered by Greitzer is the axial compressor rotor as depicted in Fig. 2.8a. The pressure field associated with the blades is such that the pressure increases from the suction surface (S) to the pressure surface (P). This pressure field moves with the blades and, to an observer situated at the point * (in the absolute frame of reference), a pressure that varies with time would be recorded, as shown in Fig. 2.8b. Therefore, fluid particles passing through the rotor would experience a positive pressure increase with time (i.e. $\partial p/\partial t > 0$). From this fact it can then be shown that the stagnation enthalpy of the fluid particle also increases because of the unsteadiness of the flow, i.e.

$$\frac{Dh_0}{Dt} = \frac{1}{\rho}\frac{\partial p}{\partial t} \quad \text{(Eq. 2.17)}$$

where *D/Dt* is the rate of change following the fluid particle.

2.1.10 Stall and Surge

A salient feature of a compressor performance map, such as Fig. 2.6, is the limit to stable operation known as the *surge line*. This limit can be reached by reducing the mass flow (with a throttle valve) whilst the rotational speed is maintained constant. When a compressor goes into surge the effects are usually quite dramatic. Generally, an increase in noise level is experienced, indicative of a pulsation of the air flow and of mechanical vibration. Commonly, there are a small number of predominant frequencies superimposed on a high background noise. The lowest frequencies are usually associated with a Helmholtz-type of resonance of the flow through the machine, with the inlet and/or outlet volumes. The higher frequencies are known to be due to rotating stall and are of the same order as the rotational speed of the rotor.

Rotating stall is a phenomenon of axial-compressor flow which has been the subject of many detailed experimental and theoretical investigations and the matter is still not fully resolved. An early survey of the subject was given by Emmons *et al*. (1959). Briefly, when a blade row (usually the rotor of a compressor reaches the "stall point", the blades instead of all stalling together as might be expected, stall in separate patches and these stall patches, moreover, travel around the compressor annulus (i.e. they rotate). That stall patches must propagate from blade to blade has a simple physical explanation. Consider a portion of a blade row, as illustrated in Fig. 2.9 to be affected by a stall patch. This patch must cause a partial obstruction to the flow which is deflected on both sides of it. Therefore, the incidence of the flow on to the blades on the right of the stall cell is reduced but, the incidence to the left is increased. As these blades are already close to stalling, the net effect is for the stall patch to move to the left. The motion is then self-sustaining.

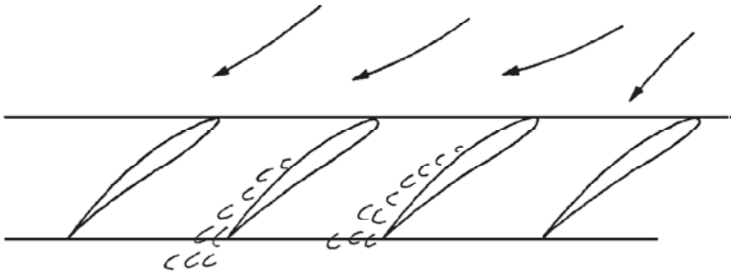

Fig. 2.9 Model illustrating Mechanism of Stall Cell Propagation: Partial blockage due to stall patch deflects flow, increasing incidence to the left and decreasing incidence to the right (Dixon, 1998).

There is a strong practical reason for the wide interest in rotating stall. Stall patches travelling around blade rows load and unload each blade at some frequency related to the speed and number of the patches. This frequency may be close to a natural frequency of blade vibration and there is clearly a need for accurate prediction of the conditions producing such a vibration. Several cases of blade failure due to resonance induced by rotating stall have been reported, usually with serious consequences to the whole compressor.

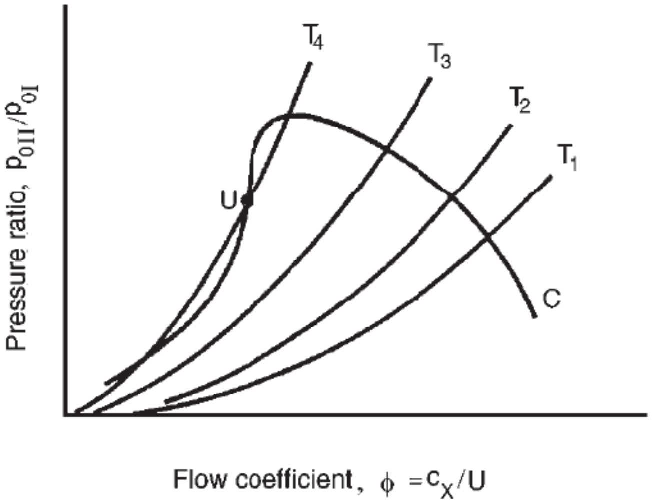

Fig 2.10 Stability of Operation of a Compressor (Horlock 1958).

It is possible to distinguish between surge and propagating stall by the unsteadiness, or otherwise, of the total mass flow. The characteristic of stall propagation is that the flow passing through the annulus, summed over the whole area, is steady with time. The stall cells merely redistribute the flow over the annulus. Surge, on the other hand, involves an axial oscillation of the total mass flow, a condition highly detrimental to efficient compressor operation.

The conditions determining the point of surge of a compressor have not yet been completely determined satisfactorily. One physical explanation of this breakdown of the flow is given by Horlock (1958). Fig. 2.10 shows a constant rotor speed compressor characteristic (*C*) of pressure ratio plotted against flow coefficient. A second set of curves (T_1, T_2, etc.) are superimposed on this figure showing the pressure loss characteristics of the throttle for various fixed throttle positions. The intersection of curves *T* with compressor curve C denotes the various operating points of the combination. A state of flow stability exists if the throttle curves at the point of intersection have a greater (positive) slope than the compressor curve. That this is so may be illustrated as follows. Consider the operating point at the intersection of T_2 with *C*. If a small reduction of flow should momentarily occur, the compressor will produce a greater pressure rise and the throttle resistance will fall. The flow rate must, of necessity, increase so that the original operating point is restored. A similar argument holds if the flow is temporarily augmented, so that the flow is completely stable at this operating condition.

If now, the operating point is at point *U*, unstable operation is possible. A small reduction in flow will cause a greater reduction in compressor pressure ratio than the corresponding pressure ratio across the throttle. As a consequence of the increased resistance of the throttle, the flow will decrease even further and the operating point *U* is clearly unstable. By inference, neutral stability exists when the slopes of the throttle pressure loss curves equal the compressor pressure rise curve.

Tests on low pressure ratio compressors appear to substantiate this explanation of instability. However, for high rotational speed multistage compressors the above argument does not seem sufficient to describe surging. With high speeds no stable operation appears possible on constant speed curves of positive slope and surge appears to occur when this slope is zero or even a little negative. A more complete understanding of surge in multistage compressors is only possible from a detailed study of the individual stages performance and their interaction with one another.

2.1.11 Choking

When the velocity of fluid in a passage reaches the speed of sound at any cross section, the flow becomes choked (air ceases to flow). When a cascade is choked, no further increase in mass flow through the cascade is possible, the mass flow remains constant. The choked regions of the compressor characteristics may be recognised by the vertical portions of the constant speed lines.

2.1.12 Vibration and Noise

Blade vibration and noise are conveniently considered together for two reasons. Both are unsteady processes and each can be a serious nuisance. Of the two the problem of blade vibration is likely to be far more worrying to the designer because high levels of vibration can lead to part or all of the blades breaking off. Enormous amounts of downstream damage are then likely to occur possibly causing total destruction of the compressor. Noise is a less serious threat to the compressor itself and only in exceptional cases is the level of pressure fluctuation high enough to cause mechanical damage.

Vibration

Blade vibrations in compressors and turbines have many features in common and in axial turbines vibration was a problem before the first axial compressor was built. Campbell's (Campbell, 1924) work on axial turbines carries over to today's compressors and is remembered in the Campbell diagram. The vulnerability of turbomachines to vibration, particularly axial machines, is not surprising in view of the use of long slender blades, the large gas loads, the proximity of moving and stationary components and the small amount of mechanical damping.

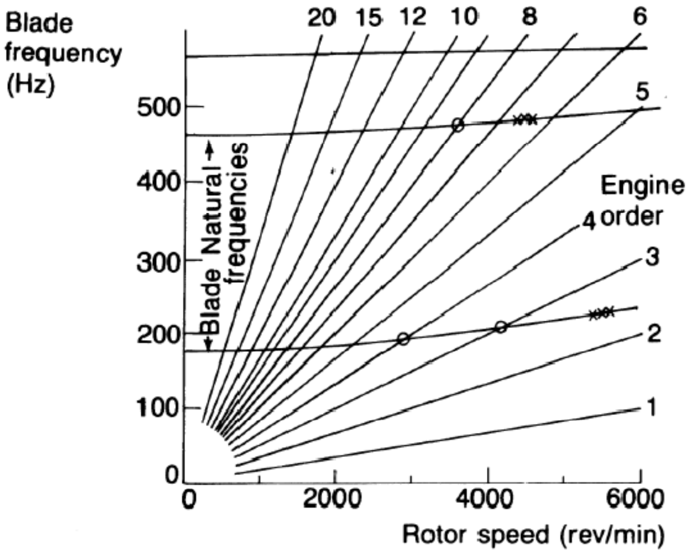

Fig. 2.11 Campbell Diagram for a Rotor Blade (circles indicate for forced resonances, crosses show either rotational stall or flutter) (Cumpsty, 2004).

There are two quite different types of vibration to be considered. Forced vibration and flutter. The former, which is easier to understand and to obviate, arises from the movement of the rotor through disturbances which are usually stationary, for example wakes or potential fields of an upstream stator, the wake of some upstream element such as a strut or the inlet distortion. It can also arise from the excitation produced by passing through rotating stall cells. Forced vibration becomes a problem when the excitation frequency coincides with a natural frequency of the blades. Flutter, on the other hand, is a self- excited oscillation or instability at or close to the natural frequency of the mechanical system which does not require any disturbance of finite amplitude to excite it.

Forced Vibration

The Campbell diagram (Fig. 2.11) is a convenient way to view the possible coincidence of blade natural frequency with excitation of the rotor blades by non-uniformities of the flow. Some of the engine orders are more important than others. The lowest engine orders tend to produce quite high excitation because the flow around the annulus is never truly uniform. There are several reasons for this. The inlet flow has non- uniform stagnation pressure because of ingested distortion or intake boundary layer effects or has static pressure distortion due to such effects as upstream bends. Inlet distortion tends to produce excitations at the low engine orders, the precise excitation being obtained from a Fourier analysis of the circumferential pattern. Struts upstream of downstream excite the blades at engine orders corresponding to their number and harmonics thereof. Upstream obstructions cause excitation by their potential flow effect and by their wakes. Downstream bodies can only affect the rotor by the potential flow effect. The potential flow effect decreases approximately exponentially with distance in the flow direction. The effect of the wake decreases more slowly than the potential effect and downstream of an obstruction the wake is usually more important.

2.2 Theoretical Analysis of Axial Compressors

2.2.1 Theory of Radial Equilibrium

The flow in an annular passage in which there is no radial component of velocity, whose streamlines lie in circular, cylindrical surfaces and which is axisymmetric, is commonly known as radial equilibrium flow. An analysis called the radial equilibrium method, widely used for three-dimensional design calculations in axial compressors and turbines, is based upon the assumption that any radial flow which may occur, is completed within a blade row, the flow outside the row then being in radial equilibrium. Fig. 2.12 illustrates the nature of this assumption.

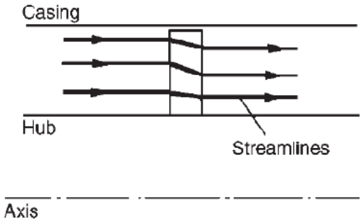

Fig. 2.12 Radial Equilibrium Flow through a Rotor Blade Row (Dixon, 1998).

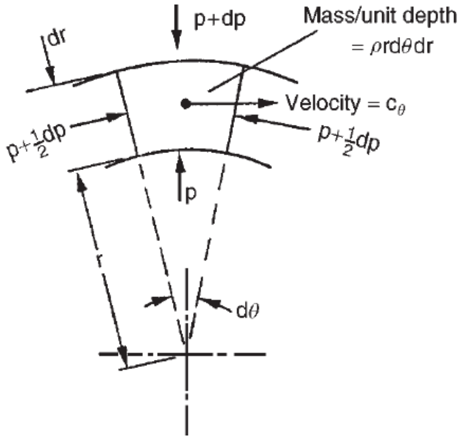

Fig. 2.13 A Fluid Element in Radial Equilibrium ($c_r = 0$) (Dixon, 1998).

Consider a small element of fluid of mass dm, shown in Fig. 2.13, of unit depth and subtending an angle $d\theta$ at the axis, rotating about the axis with tangential velocity, c_θ at radius *r*. The element is in radial equilibrium so that the pressure forces balance the centrifugal forces

$$(p + dp)(r + dr)d\theta - prd\theta - \left(p + \frac{1}{2}dp\right)drd\theta = \frac{dmc_\theta^2}{r}. \qquad \text{(Eq. 2.18)}$$

Writing $dm = \rho rd\theta dr$ and ignoring terms of the second order of smallness the above equation reduces to,

$$\frac{1}{\rho}\frac{dp}{dr} = \frac{c_\theta^2}{r}. \qquad \text{(Eq. 2.19)}$$

The stagnation enthalpy is written ($c_r = 0$)

$$h_0 = h + \frac{1}{2}(c_x^2 + c_\theta^2) \qquad \text{(Eq. 2.20)}$$

therefore,

$$\frac{dh_0}{dr} = \frac{dh}{dr} + c_x\frac{dc_x}{dr} + c_\theta\frac{dc_\theta}{dr}. \qquad \text{(Eq. 2.21)}$$

Substituting the thermodynamic relation

$$T\frac{ds}{dr} = \frac{dh}{dr} - \frac{1}{\rho}\frac{dp}{dr}, \qquad \text{(Eq. 2.22)}$$

combining equations 2.19, 2.21 and 2.22 and eliminating dp/dr and dh/dr, the radial equilibrium equation is obtained,

$$\frac{dh_0}{dr} - T\frac{ds}{dr} = c_x\frac{dc_x}{dr} + \frac{c_\theta}{r}\frac{d(c_\theta r)}{dr}. \qquad \text{(Eq. 2.23)}$$

2.2.2 Free Vortex Flow

This is a flow where the product of radius and tangential velocity remains constant (i.e. $rc_\theta = K$, a constant). The term “vortex-free” might be more appropriate as the vorticity (to be precise, the axial vorticity component) is then zero.

Consider the case of a compressor stage in which $rc_{\theta 1} = K_1$ before the rotor and $rc_{\theta 2} = K_2$ after the rotor, where K_1, K_2 are constants. The work done by the rotor on unit mass of fluid is

$$\Delta W = U(c_{\theta 2} - c_{\theta 1}) = \Omega r\left(\frac{K_2}{r} - \frac{K_1}{r}\right) = constant. \qquad \text{(Eq. 2.24)}$$

Therefore, the work done is equal at all radii.

The Reaction introduced in chapter 2.1.6 for a normal stage (α_1 = α_3) with c_x constant across the stage becomes

$$R = 1 - \frac{k}{r^2}, \qquad \text{(Eq. 2.25)}$$

where

$$k = \frac{K_1 + K_2}{2\Omega}. \qquad \text{(Eq. 2.26)}$$

As k is positive, the reaction increases from hub to tip. Likewise, static pressure increases from hub to tip as c_θ^2/r is always positive (Eq. 2.19).

The simplicity of the flow under free-vortex conditions is, superficially, very attractive to the designer and many compressors have been designed to conform to this flow. Characteristic of this flow are the large fluid deflections near the inner wall and high Mach numbers near the outer wall, both effects being deleterious to efficient performance.
A further serious disadvantage is the large amount of rotor twist from hub to tip which adds to the expense of blade manufacture. Many types of vortex design have been proposed to overcome some of the disadvantages set by free-vortex design and several of these are compared by Horlock (1958). A radial equilibrium solution for the work and axial velocity distribution of one of these vortex flows in an axial compressor stage is given below.

2.2.3 Forced Vortex Flow

This is sometimes called "solid-body" rotation because c_θ varies directly with *r*. At entry to the rotor assume enthalpy h_{01} and entropy *s* is constant and $c_{\theta 1} = K_1 r$.

With Eq. 2.23

$$\frac{d}{dr}\left(\frac{c_{x1}^2}{2}\right) = -K_1 \frac{d}{dr}(K_1 r^2) \qquad \text{(Eq. 2.27)}$$

and after integrating,

$$c_{x1}^2 = constant - 2K_1^2 r^2 \qquad \text{(Eq. 2.28)}$$

After the rotor $c_{\theta 2} = K_2 r$ and $h_{02} - h_{01} = U(\,c_{\theta 2} - \,c_{\theta 1}) = \Omega(K_2 - K_1)r^2$. Therefore, as the work distribution is non-uniform, the radial equilibrium in the form Eq. 2.23 is required for the flow after the rotor.

$$\frac{dh_{02}}{dr} = 2\Omega(K_2 - K_1)r = \frac{d}{dr}\left(\frac{c_{x2}^2}{2}\right) + K_2 \frac{d}{dr}(K_2 r^2). \qquad \text{(Eq. 2.29)}$$

After rearranging and integrating

$$c_{x2}^2 = constant - 2[K_2^2 - \,\Omega(K_2 - K_1)]r^2. \qquad \text{(Eq. 2.30)}$$

The constants of integration in equations 2.28 and 2.30 can be found from the continuity of mass flow, i.e.

$$\frac{\dot{m}}{2\pi\rho} = \int_{r_h}^{r_t} c_{x1} r dr = \int_{r_h}^{r_t} c_{x2} r dr,$$

which applies to the assumed incompressible flow.

2.3 Computational Fluid Dynamics

Computational Fluid Dynamics (CFD) is a computer-based tool for simulating the behaviour of systems involving fluid flow, heat transfer and other related physical processes. It works by solving the equations of fluid flow in a special form over a region of interest, with specified known conditions on the boundary of that region.

2.3.1 History of CFD

Computers have been used to solve fluid flow problems for many years. Numerous programs have been written to solve either specific problems, or specific classes of problems. From the mid-1970's, the complex mathematics required to generalise the algorithms began to be understood, and general purpose CFD solvers were developed. These began to appear in the early 1980's and required what were then very powerful computers, as well as an in- depth knowledge of fluid dynamics, and large amounts of time to set up simulations. Consequently, CFD was a tool used almost exclusively in research. Recent advances in computing power, together with powerful graphics and interactive 3D- manipulation of models have made the process of creating a CFD model and analysing results much less labour intensive, reducing time and, hence, cost. Advanced solvers contain algorithms which enable robust solutions of the flow field in a reasonable time. As a result of these factors, Computational Fluid Dynamics is now an established industrial design tool, helping to reduce design timescales and improve processes throughout the engineering world. CFD provides a cost-effective and accurate alternative to scale model testing, with variations on the simulation being performed quickly, offering obvious advantages.

2.3.2 Mathematics of CFD

The set of equations which describe the processes of momentum, heat and mass transfer are known as the Navier-Stokes equations. These partial differential equations were derived in the early nineteenth century and have no known general analytical solution but can be discretised and solved numerically. Equations describing other processes, such as combustion, can also be solved in conjunction with the Navier-Stokes equations. Often, an approximating model is used to derive these additional equations, turbulence models being a particularly important example. There are a number of different solution methods which are used in CFD codes. The most common is known as the finite volume technique. In this technique, the region of interest is divided into small sub regions, called control volumes. The equations are discretised and solved iteratively for each control volume. As a result, an approximation of the value of each variable at specific points throughout the domain can be obtained. In this way, one derives a full picture of the behaviour of the flow.

2.3.3 CFD Methodology

CFD may be used to determine the performance of a component at the design stage, or it can be used to analyse difficulties with an existing component and lead to its improved design. For example, the pressure drop through a component may be considered excessive:

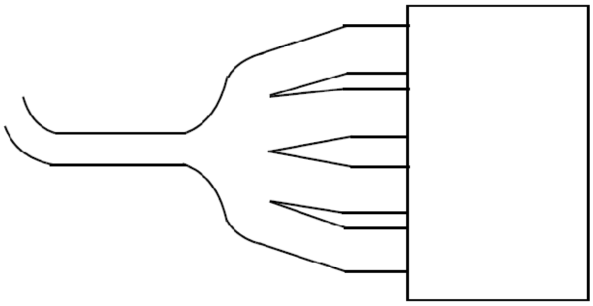

Fig. 2.14 Example Component (ANSYS, 2007).

The first step is to identify the region of interest:

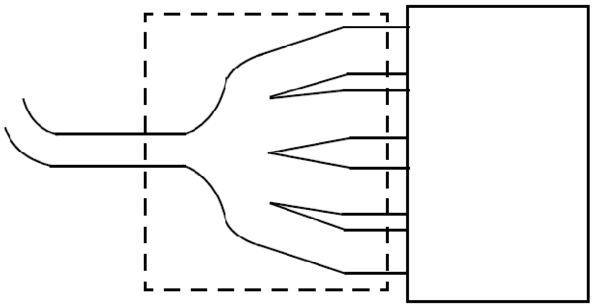

Fig. 2.15 Region of Interest (ANSYS, 2007).

The geometry of the region of interest is then defined and the mesh is created. After importing the mesh into the pre-processor, other elements of the simulation including the boundary conditions (inlets, outlets, etc.) and fluid properties are defined:

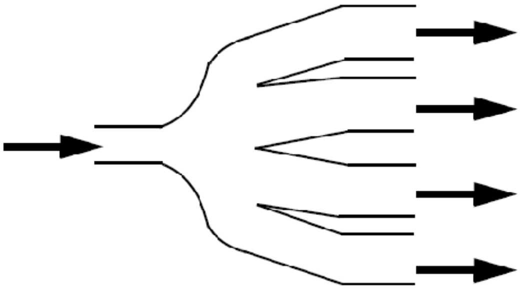

Fig. 2.16 Region of Interest with applied Boundary Conditions (ANSYS, 2007).

The flow solver is run to produce a file of results which contain the variation of velocity, pressure and any other variables throughout the region of interest. The results can be visualised and can provide an understanding of the behaviour of the fluid throughout the region of interest:

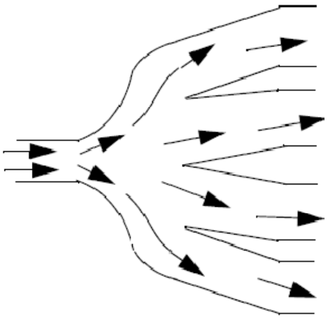

Fig. 2.17 Flow Field through Region of Interest (ANSYS, 2007).

This may lead to design modifications which can be tested by changing the geometry of the CFD model and seeing the effect. The process of performing a single CFD simulation is split into five components:

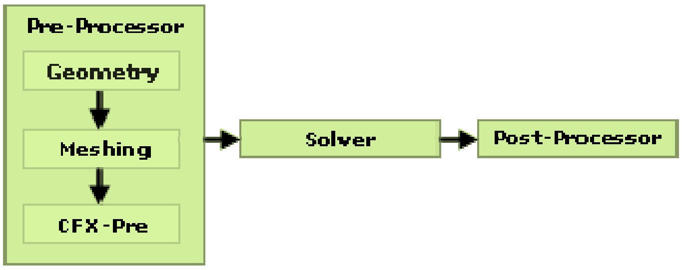

Fig. 2.18 Capabilities of the ANSYS CFX Software Package.

Geometry / Mesh

This interactive process is the first pre-processing stage. The objective is to produce a mesh for input to the physics pre-processor. Before a mesh can be produced, a closed geometric solid is required. The geometry and mesh can be created in CAD2Mesh or any of the other geometry/mesh creation tools. The basic steps involve:

1. Defining the geometry of the region of interest
2. Creating regions of fluid flow, solid regions and surface boundary names
3. Setting properties for the mesh

Physics Definition

This interactive process is the second pre-processing stage and is used to create input required by the Solver. The mesh files are loaded into the physics pre-processor. The physical models that are to be included in the simulation are selected. Fluid properties and boundary conditions are specified.

Solver

The Solver produces the required results in a non-interactive/batch process. The problem is solved as follows:

1. The partial differential equations are integrated over all the control volumes in the region of interest. This is equivalent to applying a basic conservation law (e.g. for mass or momentum) to each control volume.

2. These integral equations are converted to a system of algebraic equations by generating a set of approximations for the terms in the integral equations.

3. The algebraic equations are solved iteratively.

An iterative approach is required because of the non-linear nature of the equations, and as the solution approaches the exact solution, it is said to converge. For each iteration an error or residual is reported as a measure of the overall conservation of the flow properties. How close the final solution is to the exact solution depends on a number of factors, including the size and shape of the control volumes and the size of the final residuals. Complex physical processes, such as combustion and turbulence, are often modelled using empirical relationships. The approximations inherent in these models also contribute to differences between the CFD solution and the real flow. The solution process requires no user interaction and is, therefore, usually carried out as a batch process. The solver produces a results file which is then passed to the post-processor.

Post-Processor

The post-processor is the component used to analyse, visualise and present the results interactively. Post-processing includes anything from obtaining point values to complex animated sequences. Examples of some important features of post-processors are:

- Visualisation of the geometry and control volumes
- Vector plots showing the direction and magnitude of the flow
- Visualisation of the variation of scalar variables (variables which have only magnitude, not direction, such as temperature, pressure, ...) through the domain
- Quantitative numerical calculations
- Animation Charts showing graphical plots of variables
- Hardcopy output

2.3.4 Governing Equations

The software in use for the present work is the commercial ANSYS CFX 10.0 software containing the pre-processor, the solver and a post-processing tool. The governing equations are implemented in the code as they are described on the following pages.

Transport Equations

The instantaneous equations of mass, momentum and energy conservation can be written as follows in a stationary frame of reference:
Continuity:

$$\frac{\partial \rho}{\partial t} + \nabla \cdot \left(\rho \vec{U}\right) = 0$$

Momentum equations:

$$\frac{\partial\left(\rho \vec{U}\right)}{\partial t} + \nabla \cdot \left(\rho \vec{U} \otimes \vec{U}\right) = -\nabla p + \nabla \cdot \tau + \vec{s}_M$$

Where the stress tensor τ is related to the strain rate by

$$\tau = \mu(\nabla \vec{U} + \left(\nabla \vec{U}\right)^T - \frac{2}{3}\delta \nabla \cdot \vec{U}$$

Total Energy Equation:

$$\frac{\partial(\rho h_0)}{\partial t} - \frac{\partial p}{\partial t} + \nabla \cdot \left(\rho \vec{U} h_0\right) = \nabla \cdot (\lambda \nabla T) + \nabla \cdot \left(\vec{U} \cdot \tau\right) + \vec{U} \cdot \vec{s}_M + \vec{s}_E$$

where h_o is the total Enthalpy. The term $\nabla \cdot (\overline{U} \cdot \tau)$ represents the work due to viscous stresses and is called the viscous work term. The term $\overline{U} \cdot \overline{s}_M$ represents the work due to external momentum sources and is currently neglected.

Equations of State

The flow solver calculates pressure and static enthalpy. Finding density requires that we select the thermal equation of state and finding temperature requires that we select the constitutive relation. The selection of these two relationships is not necessarily independent and is also a modelling choice. The thermal equation of state is described as a function of both temperature and pressure:

$$\rho = \rho(p, T)$$

The specific heat capacity c_p, may also be described as a function of temperature and pressure:

$$c_p = c_p(p, T)$$

For an ideal gas, the density is defined by the ideal gas law and, in this case c_p, can be a function of only temperature:

$$c_p = c_p(T)$$

Ideal Gas Equation of State

For an ideal gas, the relationship is described by the ideal gas law:

$$\rho = \frac{w(p + p_{ref})}{R_0 T}$$

where w is the molecular weight of the gas and R_o is the universal gas constant.

2.3.5 Turbulence Models

Turbulence consists of fluctuations in the flow field in time and space. It is a complex process, mainly because it is three dimensional, unsteady and consists of many scales. It can have a significant effect on the characteristics of the flow. Turbulence occurs when the inertia forces in the fluid become significant compared to viscous forces, and is characterised by a high Reynolds Number. In principle, the Navier-Stokes equations describe both laminar and turbulent flows without the need for additional information. However, turbulent flows at realistic Reynolds numbers span a large range of turbulent length and time scales, and would generally involve length scales much smaller than the smallest finite volume mesh, which can be practically used in a numerical analysis. The Direct Numerical Simulation (DNS) of these flows would require computing power which is many orders of magnitude higher than available in the foreseeable future.

To enable the effects of turbulence to be predicted, a large amount of CFD research has concentrated on methods which make use of turbulence models. Turbulence models have been specifically developed to account for the effects of turbulence without recourse to a prohibitively fine mesh and Direct Numerical Simulation. Most turbulence models are statistical turbulence model. The two exceptions to this are the Large Eddy Simulation model and the Detached Eddy Simulation model.

Statistical Turbulence Models and the Closure Problem

When looking at time scales much larger than the time scales of turbulent fluctuations, turbulent flow could be said to exhibit average characteristics, with an additional time-varying, fluctuating component. For example, a velocity component may be divided into an average component and a time varying component. In general, turbulence models seek to modify the original unsteady Navier-Stokes equations by the introduction of averaged and fluctuating quantities to produce the Reynolds Averaged Navier-Stokes (RANS) equations. These equations represent the mean flow quantities only, while modelling turbulence effects without a need for the resolution of the turbulent fluctuations. All scales of the turbulence field are being modelled. Turbulence models based on the RANS equations are known as Statistical Turbulence Models due to the statistical averaging procedure employed to obtain the equations. Simulation of the RANS equations greatly reduces the computational effort compared to a Direct Numerical Simulation and is generally adopted for practical engineering calculations. However, the averaging procedure introduces additional unknown terms containing products of the fluctuating quantities, which act like additional stresses in the fluid. These terms, called 'turbulent' or 'Reynolds' stresses, are difficult to determine directly and so become further unknowns. The Reynolds (turbulent) stresses need to be modelled by additional equations of known quantities in order to achieve "closure." Closure implies that there is a sufficient number of equations for all the unknowns, including the Reynolds-Stress tensor resulting from the averaging procedure. The equations used to close the system define the type of turbulence model.

Reynolds Averaged Navier Stokes (RANS) Equations

As described above, turbulence models seek to solve a modified set of transport equations by introducing averaged and fluctuating components. For example, a velocity $\overrightarrow{U}$ may be divided into an average component and a time varying component:

$$U(t) = \overline{U} + u'(t)$$

The averaged component is given by:

$$\overline{U} = \frac{1}{\Delta t}\int_{t}^{t+\Delta t} U(t)dt$$

where Δt is a time scale that is large relative to the turbulent fluctuations, but small relative to the time scale to which the equations are solved.

Substituting the time averaged quantities into the original transport equations results in the Reynolds-averaged equations given below:

Continuity:

$$\frac{\partial \rho}{\partial t} + \nabla \cdot \left(\rho \vec{U}\right) = 0$$

Momentum equations:

$$\frac{\partial\left(\rho \vec{U}\right)}{\partial t} + \nabla \cdot \left(\rho \vec{U} \otimes \vec{U}\right) = \nabla(\tau - \rho\overline{u' \otimes u'}) + \vec{s}_M$$

Scalar Transport:

$$\frac{\partial(\rho\phi)}{\partial t} + \nabla \cdot \left(\rho \vec{U} \phi\right) = \nabla \cdot (\Gamma \nabla \phi - \rho\overline{u'\phi}) + \vec{s}_E$$

The continuity equation has not been altered but the momentum and scalar transport equations contain turbulent flux terms additional to the molecular diffusive fluxes. These are the Reynolds stress $\rho\overline{u' \otimes u'}$, and the

Reynolds flux $\rho\overline{u'\phi}$. These terms arise from the non-linear convective term in the non- averaged equations.

They reflect the fact that convective transport due to turbulent velocity fluctuations will act to enhance mixing over and above that caused by thermal fluctuations at the molecular level. At high Reynolds numbers, turbulent velocity fluctuations occur over a length scale much larger than the mean free path of thermal fluctuations, so that the turbulent fluxes are much larger than the molecular fluxes.

The Reynolds-averaged energy equation is:

$$\frac{\partial(\rho h_0)}{\partial t} + \nabla \cdot \left(\rho \vec{U} h_0 + \rho\overline{u'h} - \lambda \nabla T\right) = \frac{\partial p}{\partial t}$$

where the mean total enthalpy is given by:

$$h_0 = h + \frac{1}{2}U^2 + k$$

In addition to the mean flow kinetic energy, the total enthalpy now contains a contribution from the turbulent kinetic energy *k*, given by:

$$k = \frac{1}{2}\overline{u'^2}$$

Turbulence models close the Reynolds-averaged equations by providing models for the computation of the Reynolds stresses and Reynolds fluxes.

Eddy Viscosity Turbulence Models

One proposal suggests that turbulence consists of small eddies which are continuously forming and dissipating, and in which the Reynolds stresses are assumed to be proportional to mean velocity gradients. This defines an 'eddy viscosity model'. The eddy viscosity hypothesis assumes that the Reynolds stresses can be related to the mean velocity gradients and Eddy (turbulent) Viscosity by the gradient diffusion hypothesis, in a manner analogous to the relationship between the stress and strain tensors in laminar Newtonian flow:

$$-\mathrm{\rho}\overline{u' \otimes u'} = -\frac{2}{3}\rho k\delta - \frac{2}{3}\mu_t \nabla \cdot \vec{U}\delta + \mu_t(\nabla\vec{U} + \left(\nabla\vec{U}\right)^T)$$

Here μ_t is the Eddy Viscosity or Turbulent Viscosity. This has to be prescribed. Analogous to the eddy viscosity hypothesis is the eddy diffusivity hypothesis, which states that the Reynolds fluxes of a scalar are linearly related to the mean scalar gradient:

$$-\rho\overline{u'\phi} = \Gamma_\mathrm{t}\nabla\phi$$

here, Γ_t is the Eddy Diffusivity and has to be prescribed. The Eddy Diffusivity can be written as:

$$\Gamma_\mathrm{t} = \frac{\mu_t}{\mathrm{Pr_t}}$$

Where $\mathrm{Pr_t}$ is the turbulent Prandtl number. Eddy diffusivities are then prescribed using the turbulent Prandtl number.

The above equations can only express the turbulent fluctuation terms of functions of the mean variables if the turbulent viscosity is known. Both the $k - \varepsilon$ and $k - \omega$ two-equation turbulence models provide this variable.

Subject to these hypotheses, the Reynolds averaged momentum and scalar transport equations become:

$$\frac{\partial(\rho\vec{U})}{\partial t} + \nabla \cdot \left(\rho\vec{U} \otimes \vec{U}\right) = \vec{B} - \nabla p' + \nabla \cdot (\mu_{eff}\left(\nabla\vec{U} + \left(\nabla\vec{U}\right)^T\right))$$

$$\frac{\partial(\rho\phi)}{\partial t} + \nabla \cdot \left(\rho\vec{U}\phi - \Gamma_{eff}\nabla\phi\right) = \vec{S}$$

where $\vec{B}$ is the sum of the body forces, μ_{eff} is the effective viscosity and Γ_{eff} is the effective diffusivity, defined by:

$$\mu_{eff} = \mu + \mu_t$$

and:

$$\Gamma_{eff} = \Gamma + \Gamma_t$$

p' is a modified pressure, defined by:

$$p' = p + \frac{2}{3}\rho k + \nabla \cdot \vec{U}(\frac{2}{3}\mu_{eff} - \zeta)$$

where ζ is the bulk viscosity.
The Reynolds averaged energy equation becomes:

$$\frac{\partial(\rho h_0)}{\partial t} - \frac{\partial p}{\partial t} + \nabla \cdot \left(\rho \vec{U} h_0\right) = \nabla \cdot (\lambda \nabla T + \frac{\mu_t}{\mathrm{Pr_t}} \nabla h) + \vec{s}_E$$

It has to be remarked that although the transformation of the molecular diffusion term may be inexact if enthalpy depends on variables other than temperature, the turbulent diffusion term is correct, subject to the eddy diffusivity hypothesis. Moreover, as turbulent diffusion is usually much larger than molecular diffusion, small errors in the latter can be ignored.

Two Equation Turbulence Models

Two-equation turbulence models are very widely used, as they offer a good compromise between numerical effort and computational accuracy. Two-equation models are much more sophisticated than the zero equation models. Both the velocity and length scale are solved using separate transport equations (hence the term ‘two-equation’). The $k - \varepsilon$ and $k - \omega$ two-equation models use the gradient diffusion hypothesis to relate the Reynolds stresses to the mean velocity gradients and the turbulent viscosity. The turbulent viscosity is modelled as the product of a turbulent velocity and turbulent length scale. In two-equation models, the turbulence velocity scale is computed from the turbulent kinetic energy, which is provided from the solution of its transport equation. The turbulent length scale is estimated from two properties of the turbulence field, usually the turbulent kinetic energy and its dissipation rate. The dissipation rate of the turbulent kinetic energy is provided from the solution of its transport equation.

The $\boldsymbol{k-\varepsilon}$ Turbulence Model

k is the turbulence kinetic energy and is defined as the variance of the fluctuations in velocity. It has dimensions of (L^2T^2). ε is the turbulence eddy dissipation (the rate at which the velocity fluctuations dissipate), and has dimensions of *k* per unit time (L^2T^3). The $k-\varepsilon$ model introduces two new variables into the system of equations.
The continuity equation is then:

$$\frac{\partial \rho}{\partial t} + \nabla \cdot \left(\rho \vec{U}\right) = 0$$

and the momentum equation becomes:

$$\frac{\partial\left(\rho \vec{U}\right)}{\partial t} + \nabla \cdot \left(\rho \vec{U} \otimes \vec{U}\right) - \nabla \cdot \left(\mu_{eff} \nabla \vec{U}\right) = \nabla p' + \nabla \cdot \left(\mu_{eff}\left(\nabla \vec{U} + \left(\nabla \vec{U}\right)^{T}\right)\right)$$

where $\vec{B}$ is the sum of body forces, μ_{eff} is the effective viscosity accounting for turbulence and *p'* is the modified pressure given by:

$$p' = p + \frac{2}{3}\rho k$$

The $k-\varepsilon$ model is based on the eddy viscosity concept, so that:

$$\mu_{eff} = \mu + \mu_t$$

where μ_t is the turbulence viscosity. The $k-\varepsilon$ model assumes that the turbulence viscosity is linked to the turbulence kinetic energy and dissipation via the relation:

$$\mu_t = C_\mu \rho \frac{k^2}{\varepsilon}$$

where C_μ is a constant.
The values of *k* and ε come directly from the differential transport equations for the turbulence kinetic energy and turbulence dissipation rate:

$$\frac{\partial(\rho k)}{\partial t} + \nabla \cdot \left(\rho \vec{U} k\right) = \nabla \cdot \left[\left(\mu + \frac{\mu_t}{\sigma_k}\right)\nabla k\right] + P_k - \rho\varepsilon$$

$$\frac{\partial(\rho \varepsilon)}{\partial t} + \nabla \cdot \left(\rho \vec{U} \varepsilon\right) = \nabla \cdot \left[\left(\mu + \frac{\mu_t}{\sigma_\varepsilon}\right)\nabla \varepsilon\right] + \frac{\varepsilon}{k}\left(C_{\varepsilon 1} P_k - C_{\varepsilon 2}\rho\varepsilon\right)$$

where $C_{\varepsilon 1}$, $C_{\varepsilon 2}$, σ_k and σ_ε are constants.

P_k is the turbulence production due to viscous and buoyancy forces, which is modelled using:

$$P_k = \mu_t \nabla\vec{U} \cdot \left(\nabla\vec{U} + \nabla\vec{U}^T\right) - \frac{2}{3}\nabla \cdot \vec{U}\left(3\mu_t \nabla \cdot \vec{U} + \rho k\right) + P_{k0}$$

One of the advantages of the $k - \omega$ formulation is the near wall treatment for low-Reynolds number computations. The model does not involve the complex non-linear damping functions required for the $k - \omega$ model and is therefore more accurate and more robust. A low-Reynolds $k - \omega$ model would typically require a near wall resolution of $y^+ < 0.2$, while a low-Reynolds number $k - \omega$ model would require at least $y^+ < 2$. In industrial flows, even $y^+ < 2$ cannot be guaranteed in most applications and for this reason, a new near wall treatment was developed for the $k - \omega$ models. It allows for smooth shift from a low-Reynolds number form to a wall function formulation.

The $k - \omega$ model assumes that the turbulence viscosity is linked to the turbulence kinetic energy and turbulent frequency via the relation

$$\mu_t = \rho \frac{k}{\omega}$$

The $k - \omega$ Turbulence Model

The starting point of the present formulation is the $k - \omega$ model developed by Wilcox. It solves two transport equations, one for the turbulent kinetic energy, *k*, and one for the turbulent frequency ω. The stress tensor is computed from the eddy-viscosity concept.

k-equation:

$$\frac{\partial(\rho k)}{\partial t} + \nabla \cdot \left(\rho\vec{U}k\right) = \nabla \cdot \left[\left(\mu + \frac{\mu_t}{\sigma_k}\right)\nabla k\right] + P_k - \beta' \rho k \omega$$

ω -equation:

$$\frac{\partial(\rho \omega)}{\partial t} + \nabla \cdot \left(\rho\vec{U}\omega\right) = \nabla \cdot \left[\left(\mu + \frac{\mu_t}{\sigma_\omega}\right)\nabla \omega\right] + \frac{\alpha\omega}{k} P_k - \beta\rho\omega^2)$$

In addition to the independent variables, the density ρ and the velocity vector $\vec{U}$ are treated as known quantities from the Navier-Stokes method. P_k is the production rate of turbulence, which is calculated as in the $k - \varepsilon$ model.

The model constants are given by:

$$\beta' = 0.09 \qquad \alpha = 5/9$$

$$\beta = 0.075 \qquad \sigma_k = 2$$

$$\sigma_\omega = 2$$

The unknown Reynolds stress tensor τ is calculated from:

$$\tau = \mu_t 2s - \rho \frac{2}{3} \delta k$$

Modelling the Flow near the Wall

The wall distance is used in various functions that control the transition between near-wall and free-stream models. The wall-function approach in the commercial code used for the present work, ANSYS CFX, is an extension of the method of Launder and Spalding (Launder et al., 1974). In the log-law region, the near wall tangential velocity is related to the wall-shear-stress τ_ω, by means of a logarithmic relation. In the wall-function approach, the viscosity affected sub layer region is bridged by employing empirical formulas to provide near wall boundary conditions for the mean flow and turbulence transport equations. These formulas connect the wall conditions (e.g., the wall-shear-stress) to the dependent variables at the near-wall mesh node which is presumed to lie in the fully-turbulent region of the boundary layer. The logarithmic relation for the near wall velocity is given by:

$$u^+ = \frac{U_t}{u_\tau} = \frac{1}{\kappa} \ln(y^+) + C$$

where:

$$y^+ = \frac{\rho \Delta y u_\tau}{\mu} = \frac{1}{\kappa} \ln(y^+) + C$$

and:

$$u_\tau = (\frac{\tau_\omega}{\rho})^{1/2}$$

u^+ is the near wall velocity, u_τ is the friction velocity, U_t is the known velocity tangent to the wall at a distance of Δy from the wall, y^+ is the dimensionless distance from the wall, τ_ω is the wall shear stress, κ is the von Karman constant and *C* is a log-layer constant depending on wall roughness.

The equation for the near wall velocity u^+ has the problem that it becomes singular at separation points where the tangential velocity approaches zero. In the logarithmic region, an alternative velocity scale u^* can be used instead of u^+:

$$u^* = C_\mu^{1/4} k^{1/2}$$

This scale has the useful property that it does not go to zero if U_t goes to zero. In turbulent flow is never completely zero. Based on this definition, the following explicit equation for u_τ can be obtained:

$$u_\tau = \frac{U_t}{\frac{1}{\kappa}\ln(y^*) + C}$$

The absolute value of the wall shear stress is then obtained from:

$$\tau_\omega = \rho u^* u_\tau$$

where:

$$y^* = \frac{\rho u^* \Delta y}{\mu}$$

One of the major drawbacks of the wall-function approach is that the predictions depend on the location of the point nearest to the wall and are sensitive to the near-wall meshing; refining the mesh does not necessarily give a unique solution of increasing accuracy (Grotjans et al., 1998). The problem of inconsistencies in the wall-function, in the case of fine meshes, can be overcome with the use of the Scalable Wall Function formulation developed by CFX. It can be applied on arbitrarily fine meshes and allows to perform a consistent mesh refinement independent of the Reynolds number of the application. The basic idea behind the scalable wall-function approach is to limit the y^* value used in the logarithmic formulation by a lower value of $y^* = \max(y^*, 11.06)$. 11.06 is the intersection between the logarithmic and the linear near wall profile. The computed y^* is therefore not allowed to fall below this limit. Therefore, all mesh points are outside the viscous sub layer and all fine mesh inconsistencies are avoided.

Numerical Discretization

Analytical solutions to the Navier Stokes equations exist for only the simplest of flows under ideal conditions. To obtain solutions for real flows, a numerical approach must be adopted whereby the equations are replaced by algebraic approximations which may be solved using a numerical method.

Segregated solvers employ a solution strategy where the momentum equations are first solved, using a guessed pressure, and an equation for a pressure correction is obtained. Because of the ‘guess-and-correct’ nature of the linear system, a large number of iterations are typically required in addition to the need for judiciously selecting relaxation parameters for the variables. ANSYS CFX uses a coupled solver, which solves the hydrodynamic equations as a single system. This solution approach uses a fully implicit discretization of the equations at any given time step. For steady state problems, the time-step behaves like an ‘acceleration parameter’, to guide the approximate solutions in a physically based manner to a steady-state solution. This reduces the number of iterations required for convergence to a steady state, or to calculate the solution for each time step in a time dependent analysis. All numerical approximation schemes are prone to a degree of error. Some errors are a result of truncation of additional terms in series expansions. Others are a result of the order of the differencing scheme used for the approximation.

Numerical Diffusion

Numerical diffusion is usually exhibited by difference equations where the advection term has been approximated using an odd-order scheme which is first order accurate. The effect of this over a whole flow domain is that the features of the flow are smeared out. This phenomenon is sometimes called ‘gradient smearing’. The effect varies according to the alignment of the mesh with the flow direction. It is therefore relatively straightforward to achieve highly accurate solutions to simple flow problems, such as flow in a duct where alignment of the mesh with the predominant flow is relatively simple. However, for situations in which the flow is predominantly not aligned with the mesh, numerical diffusion effects limit the accuracy of the solution.

Numerical Dispersion

Numerical dispersion is usually exhibited by discretised equations whose advection term has been approximated using schemes that are even-order accurate. Dispersion results in oscillations or ‘wiggles’ in the solution particularly where there are steep flow gradients (e.g., across a shock).

Chapter 3

Compressor Inlet Duct (Scoop) Design

3.1 Introduction

The airship is exposed at an altitude of 21 km to wind speeds in summer up to 7 m/s and in winter up to 40 m/s. As the fan with a diameter of 60 cm is attached horizontally to the supportive plate of the airship, as illustrated in Fig. 3.1, it is also exposed to these winds. This leads to a non-axial fan inlet flow and therefore impacts the efficiency, since the fan is designed to work at the best when the flow is axial. The compressor underlies a power limitation set by the battery equipment of the airship, which does not allow drawing more energy to run the compressor at its design point, while accepting the efficiency loss resulting from the wind.

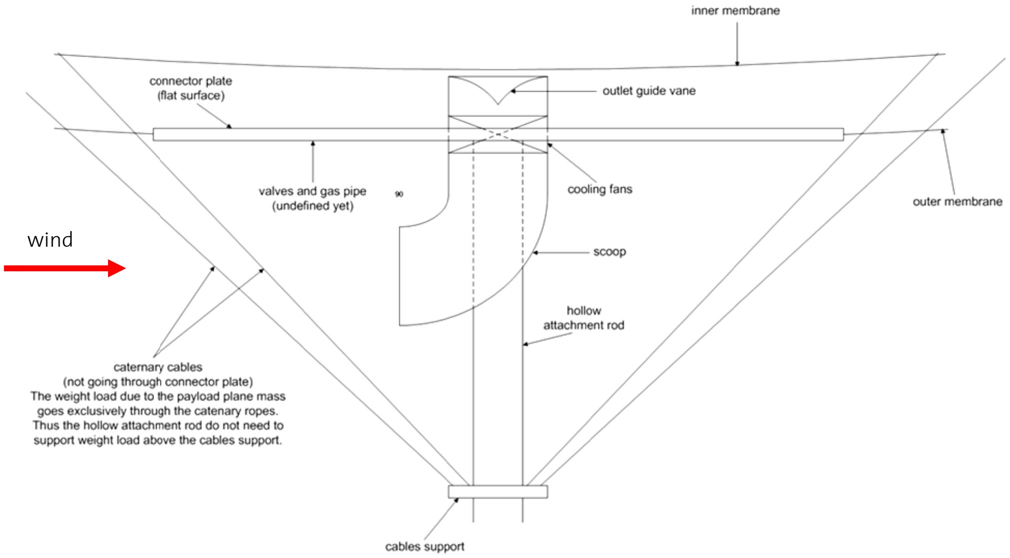

Fig. 3.1 Cooling fans mounted on a platform underneath the balloon.

The best way to cope with the wind and to get rid of the efficiency loss, is to utilize it. The idea is to attach a scoop in front of the fan that faces the wind, which acts as a tube that turns the flow towards the axial direction, as shown above in Fig. 3.1. Like this, the compressor benefits from the wind as an already existing velocity component and needs less power to suck in the necessary mass flow.

This is a beneficial way to guide the air, but again not a loss-less design. The flow inside the scoop separates due to the turning, which leads to a total pressure drop as well as a non-uniform velocity distribution at the exit, just in front of the compressor inlet. But the losses due to the scoop are expected to be smaller than those without the scoop attached in front of the compressor, especially for the windy conditions in winter.

3.1.1 Approaches and Design Steps

The duty of the scoop is to provide a beneficial way to guide the air towards the axis of the fan, while utilizing the existing wind at 21'000 km altitude.

The goal is to have an aerodynamic design of a very efficient scoop, that minimizes the flow separation, as well as the total pressure drop and the non-uniformity of the flow.

The idea is to create a benchmark for further shape modifications. Starting from a simple cylindrical 90 degree bend that turns the flow. The flow inside the scoop is modelled using CFD. Fig. 3.2 shows the simple cylindrical starting geometry. The geometry consists of a straight inlet section, a bent section and a straight outlet section. This gives three possibilities to play with the geometry in order to achieve an efficient preliminary design and to identify the trends. These are the length of the straight inlet and outlet section as well as the curvature radius of the bent section.

3.2 Preliminary Compressor Inlet Duct Design

In order to keep the number of geometries and meshes low, a deliberate way of parameter modification is thought out.

The bent section is modified first. The curvature radius is increased, starting from a reasonable value of 0.5 m, while keeping the inlet section length and the total height of the scoop constant. This leads to a shortened straight outlet section.

A maximum curvature radius of 0.7 m was found to be an optimum in terms of scoop dimensions and weight as well as flutter and vibrations. A bigger radius would structurally not make sense, although the losses would become smaller.

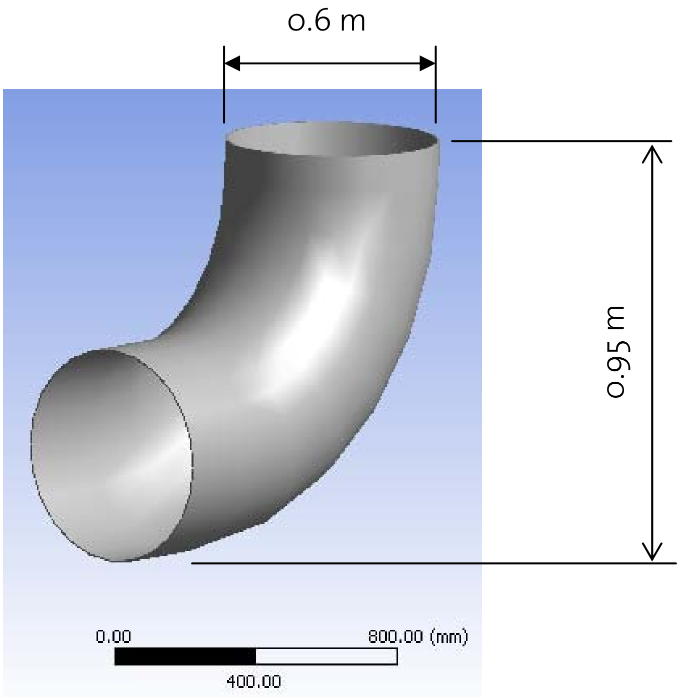

Fig. 3.2 Compressor Inlet Duct Starting Geometry: 90 ° bent.

Second, for the case of 0.7 m curvature, the outlet section length is modified to match the length of the 0.5 m outlet section. This results of course in an increased scoop total height.
The increase in outlet section height is intended to demonstrate a better turning of the exit flow towards the axial direction of the fan and to quantify this improvement. But there are two side effects. One is again the increased geometry size in terms of weight, flutter and vibrations; the other is the increase in total pressure loss, which is still better than for the starting geometry with a 0.5 m curvature radius.
Therefore, a straight outlet section length of 0.25 m is found to be a good compromise between almost axial flow and minimal total pressure losses. The computed inlet duct total height would be 0.95 m and the total width is 0.6 m.

Third, as expected, the leave out of the entire inlet section does not affect the flow much. Like this, the scoop dimensions and the weight become smaller, which is also from the structural point of view a favourable design, since the scoop becomes stiffer. This leads to the idea, having an even shorter inlet section, which is discussed in chapter 3.5.

3.3 CFD Analysis

3.3.1 Grid Generation

The primary, as well as most time consuming and crucial step to generate numerical results, is grid generation. The grid is used to discretize the governing equations in space. The accuracy of the flow solution is therefore coupled to the grid quality. The number of available grid types is important. Depending on the application, one of the following is chosen: multi-block structured, unstructured hexahedral, tetrahedral, hybrid grids consisting of hexahedral, tetrahedral, pyramidal and prismatic cells. In this work, ANSYS ICEM CFD is used for mesh generation. Above all capabilities to handle complex geometries, starting from a CAD geometry and to produce the corresponding structured meshes, render this tool well suited to the current applications. Grid generation is a highly iterative procedure and grid optimization is necessary. The next section gives information about the type of grid used in this work, as well as a description of the generation technique.

Used Technique

After preparing the 3-D blade configuration in Unigraphics NX4, the geometry is imported into ICEM for mesh generation. This is done through the ICEM Direct CAD interface for Unigraphics. This interface allows a definition of solid bodies, surfaces to be extracted, relevant curves and points, directly in the CAD environment. The different geometry families can be easily selected and a geometry definition file for ICEM can be written. Since this interface is not available, the export must be done using a third-party formats (e.g. Parasolid), which require redefinition of the different geometry families under ICEM. Another disadvantage of using third-party format is the required geometry cleanup, which is very small when exporting through the interface. Once this geometry file is available, ICEM can be run to start generating the grid. The first step here, as previously mentioned, is the geometry cleanup. In order to do this, the automatic repair tool is applied, where multiple curves, missing curves and holes in the surface are determined. Here, new surfaces can be introduced, others can be deleted, using the different tools in ICEM.

Then an optional step can be taken and is recommended. Sometimes ICEM generates one volume mesh for two different bodies. The mesh is valid, but separate access to the two bodies is needed. A remedy to this problem is to define different bodies clearly in the ICEM environment by defining material points within the bodies.

The choice of the grid is influenced by the type and complexity of the geometry, as well as the turbulence model used. The geometry to be analysed is not really complex and predestined for a block-structured grid. This is beneficial, since the hexahedral elements produce less elements for the same number of nodes than for example tetrahedral elements.

Blocking

The first step after geometry treatment is the definition of the mesh sizes on the different surfaces. The second step is to apply the multi blocking technique, necessary to get a high quality surface mesh. The control volume is divided into several blocks in order to obtain a smooth O-grid inside the cylindrical duct as shown in Fig. 3.3.

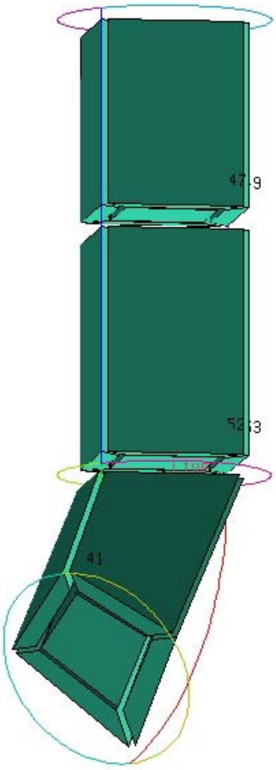

Fig. 3.3 Inlet Duct Multi Blocking.

For the present grid, the points of the surface mesh are chosen to be mapped leading to a structured mesh, where the volume is filled with hexahedras. Finally the so-called pre-mesh is converted into a primary mesh. This mesh then has to be optimized in terms of quality, aspect ratio and skewness using a smoothing tool in ICEM. The mesh for cylindrical inlet duct contains 790’387 nodes and 777’600 cells. The mesh is then imported into the pre-processing environment to set the boundary conditions. The y^+ values are in the required range for the turbulence model and solver used in the present work as discussed in chapter 3.3.3. Fig. 3.4 shows the block-structured and clustered (O-grid) mesh of the compressor duct inlet and Fig. 3.5 is showing a side view of the duct mesh.

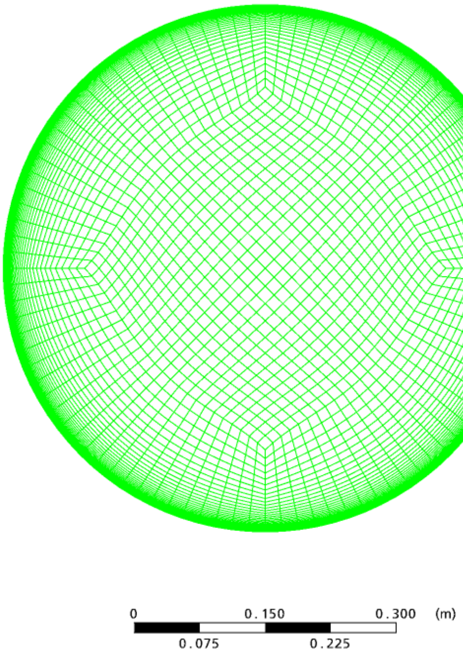

Fig. 3.4 Multi Block Structured Grid: Duct Inlet/Outlet.

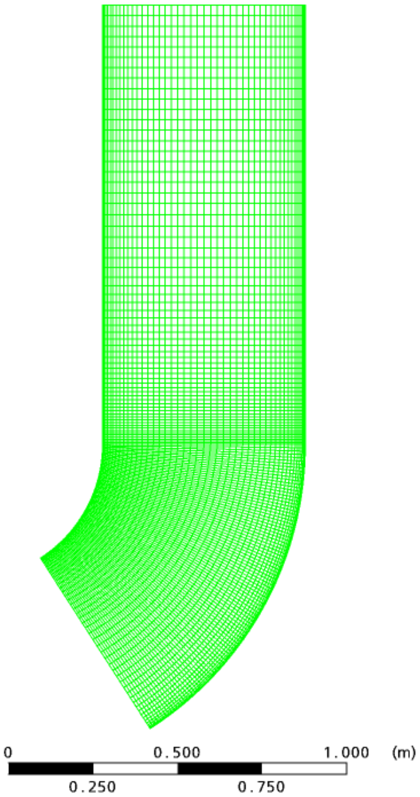

Fig. 3.5 Multi Block Structured Grid: Side View.

3.3.2 Boundary Conditions

In pre-processing the different fluid and solid domains are defined, before setting the boundary conditions and the solver parameters. At the end, the solver definition file is created.

At the beginning, the type of simulation is fixed to steady-state. Then the fluid domain is defined (Table 1) by selecting its different regions and the following parameters are set:

Parameter	Value
Fluid	Air ideal gas
Reference Pressure	5000 Pa
Heat transfer model	isothermal
Turbulence model	k-ω

Table 1 Definition of Fluid and Turbulence Model.

The next step is to set the boundary conditions for the control volume as summarized in Table 2. The particular combination of total pressure at the inlet and mass flow at the outlet yields stable results. The mass flow is given by the compressor specifications.

Boundary	Parameter	Value
Inlet	Boundary type	Subsonic Flow
	Flow Direction (65.67 °)	$\begin{bmatrix} 1 \\ 0 \\ 0.45205 \end{bmatrix}$
	Total Pressure	0 Pa
	Static Temperature	216 K
	Turbulence Intensity	5 %

Outlet	Boundary type	Subsonic Flow
	Mass Flow Rate	0.6 kg/s

Table 2 Inlet Duct Boundary Conditions.

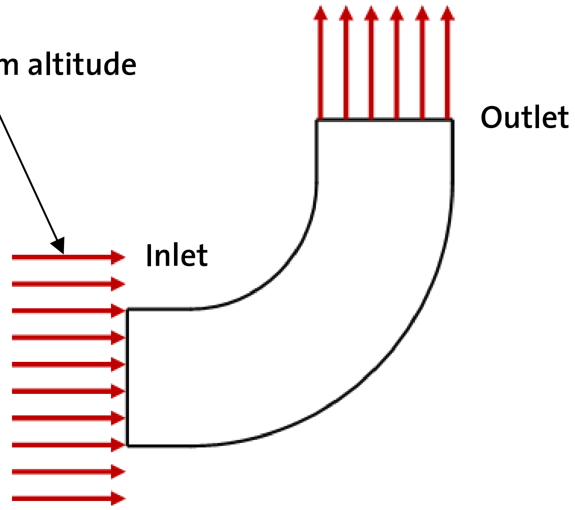

Fig. 3.6 Compressor Inlet Duct Topology and Boundary Conditions.

Fig. 3.6 shows a sketch of the topology and the boundary conditions. At the inlet a Dirichlet boundary condition is enforced. Here a uniform flow enters the calculation domain with a chosen free-stream velocity, static pressure and temperature. The flow direction is normal to the inlet section, given by the horizontal wind direction.

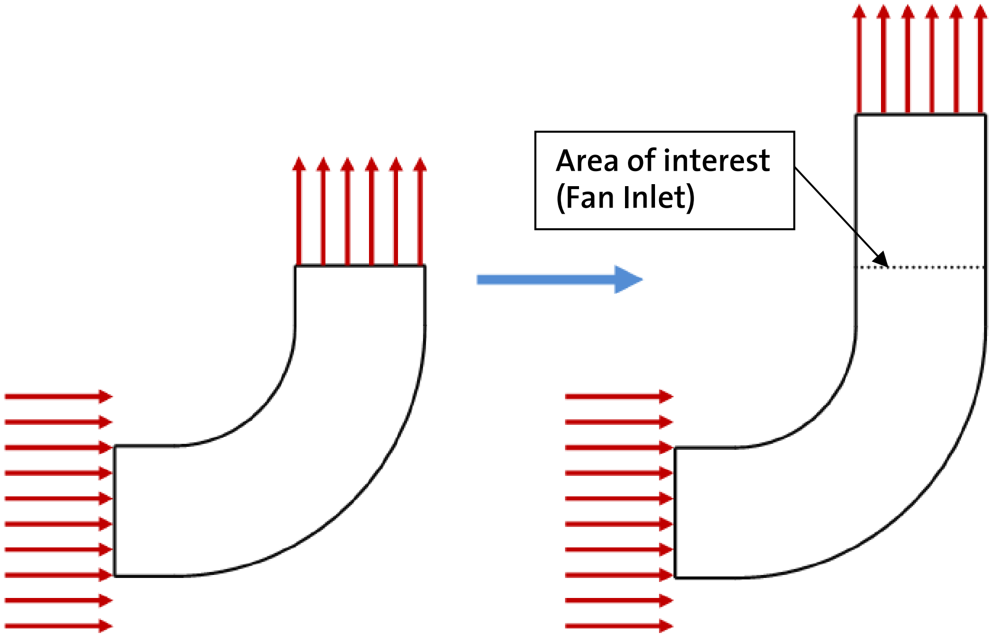

Fig. 3.7 Compressor Inlet Duct: Outlet Boundary Condition shifted further downstream.

The surface of the scoop is modelled as an isothermal no-slip wall. A characteristic boundary condition is employed at the outlet of the computational domain. The first computations showed unexpected flow behaviour at the outlet. Therefore, as can be seen in Fig. 3.7, the straight outlet section is extended in order to move the outlet section respectively the boundary condition further downstream to avoid any falsification in the area of interest, which is the location of the fan, by the opposed outlet boundary condition.

In the case of the trimmed scoop, which is described as a design optimization in chapter 3.4, the effect of the horizontal wind component has to be taken into account and to be computed. The inlet flow is then no longer normal to the inlet section.

3.3.3 Turbulence Model

One of the advantages of the k-ω formulation is the near wall treatment for low-Reynolds number computations. The model does not involve the complex non-linear damping functions required for the k-ε model and is therefore more accurate and more robust. A low-Reynolds k-ε model would typically require a near wall resolution of $y^+ < 0.2$, while a low-Reynolds number k-ω model would require at least $y^+ < 2$. In industrial flows, even $y^+ < 2$ cannot be guaranteed in most of applications and for this reason, a new near wall treatment was developed for the k-ω models. It allows for smooth shift from a low-Reynolds number form to a wall function formulation.

The turbulence model k-ω as well as the turbulence model k-ε is used for the simulations. In the case of the k-ω model, the solver is automatically switching between the two-layer-model and wall functions, depending on the y^+ value.

3.3.4 Turbulence Model Validation

It is found that the results for the simulations using the two turbulence models are different, where the k-ω turbulence model shows a much more distinct boundary layer prediction. Gontsov et al. performed an experimental investigation on a 90 degree bend, where they measured the pressure distribution along the wall. The 90 degree bend they have used is very similar to the present scoop geometry. Therefore, their experimental configuration (Fig. 3.8) is modelled and solved numerically in order to compare and to validate the numerical results with the experimental data.

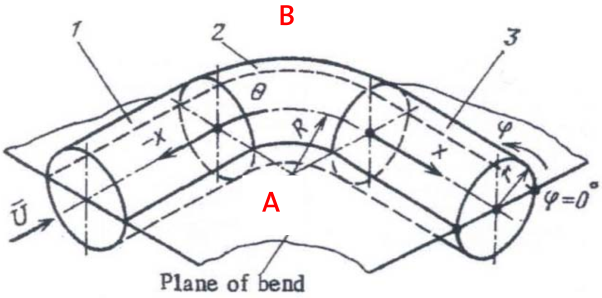

Fig. 3.8 Experimental Setup by Gontsov et. al.: 1) Delivery pipe 2) bend 3) discharge pipe.

Fig. 3.9 shows the comparison of the numerical results obtained by two different turbulence models with the available experimental data by Gontsov et. al. The pressure coefficient C_p is computed for the flow in a bend as follows:

$$C_p = \frac{P - P_{01}}{P_{01} - P_1}$$

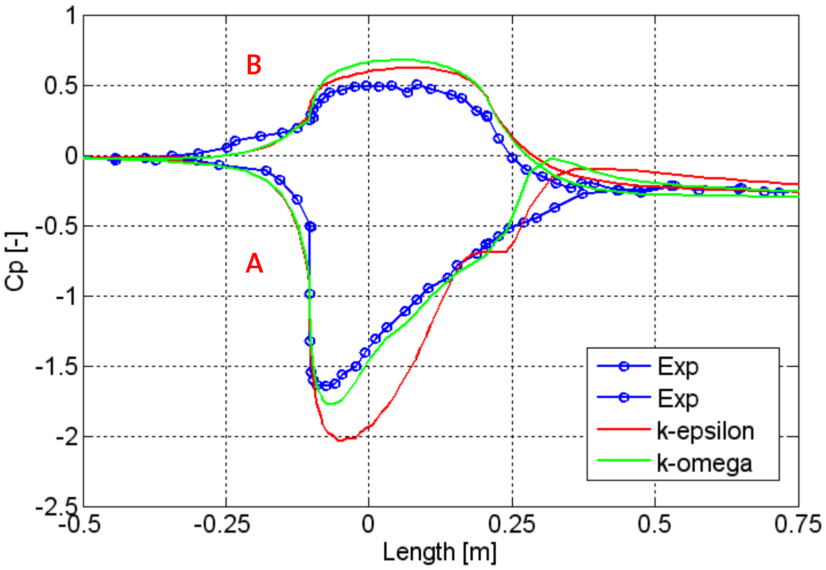

Fig. 3.9 Pressure Distribution on the walls along the length of the experimental section: Comparison of Numerical Results with available Experimental Data by Gontsov et. al.

Along branch A (Fig. 3.8), the flow strongly separates due to the bend. This is exactly the area of interest that has to be resolved as accurate as possible by the turbulence model. It can be seen that the results for the *k-ω* turbulence model are in good agreement with the experimental data, whereas the results obtained for the branch A by the *k-ε* model are quite different from the experimental data. Note, based on this validation all further numerical investigations for the duct are performed using the k-ω turbulence model.

3.3.5 Convergence Quantification

Solver Residual

The residual is a measure of the local imbalance of each conservative control volume equation. It is the most important measure of convergence as it relates directly to whether the equations have been solved. The residual is calculated using only the spatial flux terms and essentially represents a discrete conservation balance. The following residual plot representatively shows the convergence history of the stationary simulations:

According to the CFX Solver Guidelines a decrease of the RMS residuals (Fig. 3.10) of the main kinematic properties of at least three orders of magnitudes is required.

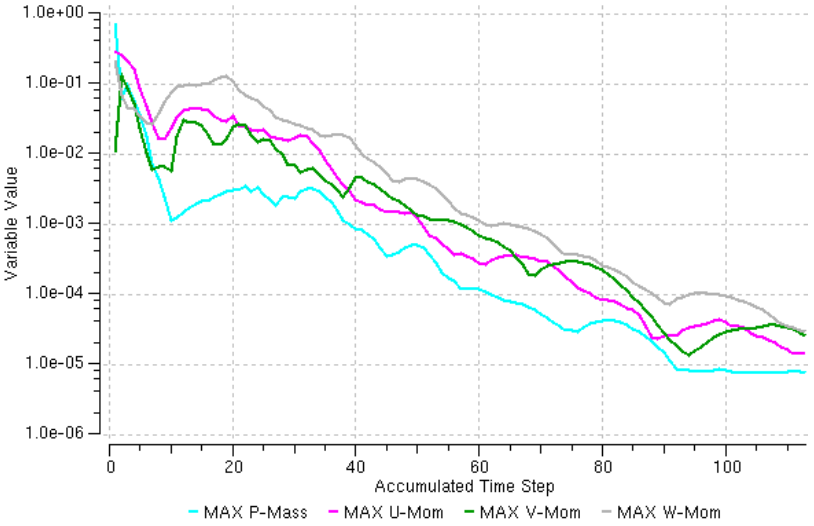

Fig. 3.10 Solver RMS Residuals.

3.4 Preliminary Results

The first simulations are performed using the two turbulence models, k-ω and k-ε. Although both show the same trends, the k-ω model shows a much more distinct boundary layer development, which seems to be more realistic. This supports the decision taken to compute all the simulations using the k-ω model, as validated in the previous chapter.

The total pressure losses become smaller with an increasing curvature. The reason is that for higher curvature the maximum velocities are smaller and thus, the boundary layer development is smaller. In all cases there is no swirl at all, only little streamline curvature can be seen.

A maximum curvature radius of 0.7 mm is found to be an optimum in terms of scoop dimensions and weight as well as flutter and vibrations. A bigger radius does structurally not make sense, although the losses would become smaller.

An outlet section length of 0.25 m is found to be a good compromise between almost axial flow and minimal total pressure losses.

The leave out of the entire inlet section does not affect the flow much. So, the scoop dimensions and the weight become smaller, which is also a favourable design from the structural point of view, since the scoop becomes more rigid.

The flow through the duct is visualized by streamlines in Fig. 3.11. Due to the turning, two big recirculation zones are generated, right in front of the location of the fan inlet. This results in a big spot of diffused velocity at the area of interest, hitting the fan as shown in Fig. 3.14. Such a distorted fan inlet flow may cause the fan to stall.

The same can be found when looking at the boundary layer development in Fig. 3.12. The flow widely separates due to the turning and a non-axial flow is the result. This means, the fan is receiving the flow at an angle, and not axially, as this is the ideal case. The inlet flow direction is shown in Fig. 3.13 for the area of interest. Therefore, the fan receives the flow at an angle of approximately 5 °.

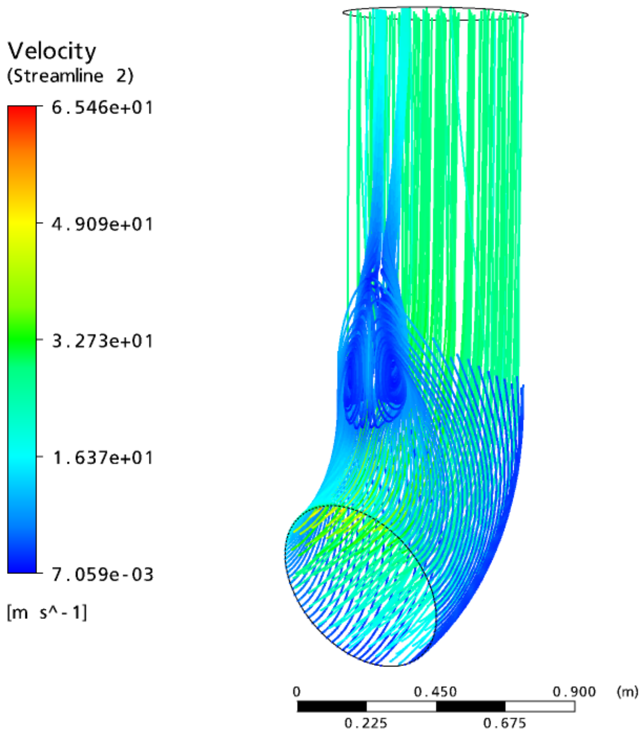

Fig. 3.11 Flow through the Duct, visualized by Streamlines.

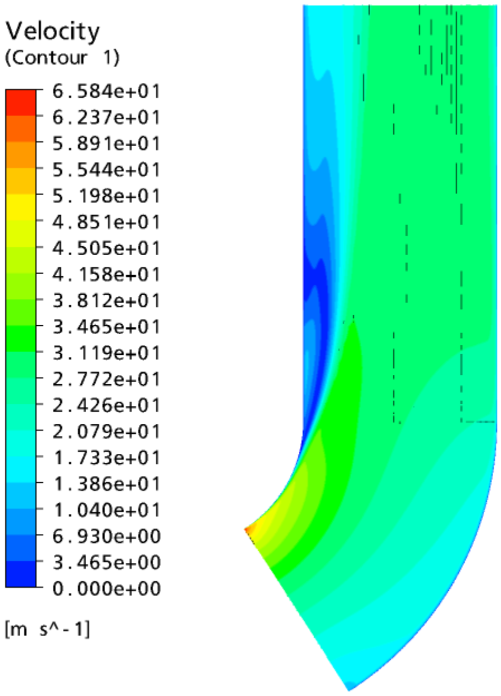

Fig. 3.12 Contour Plots of Flow through the Duct.

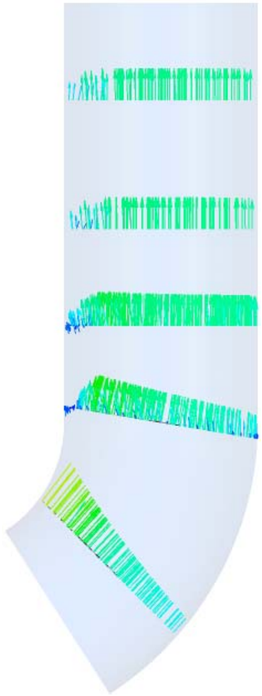

Fig. 3.13 Fan Inlet Flow Directions.

Fig. 3.14 shows the exit plane of the scoop at the location of interest according to Fig. 3.7. Here, the size and the extent of the spot of diffused velocity and the non-uniformity of the flow is clearly seen.

Based on the worked out bench mark, the next design step can be started, which is a shape optimization of the scoop cross sections. The next chapter shows how the inlet duct geometry is optimized in order to further reduce the total pressure losses as well as the emergence of the spot of diffused velocity.

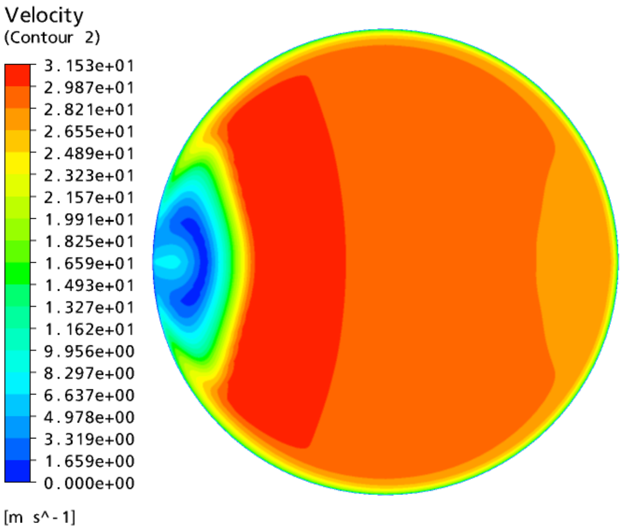

Fig. 3.14 Fan Inlet Flow Field: Spot of diffused Velocity.

3.5 Design Optimization

By means of a simple case of a bent tube with a cylindrical cross-section, a preliminary scoop design is worked out so far to obtain a benchmark for further shape modifications. This chapter explains how the cylindrical inlet cross-section is modified to obtain an efficient aerodynamic scoop design. An idea about how to modify the inlet area is gained by observing scoop inlet cross-sections of airplanes or fighters. It could be seen that the trend is somewhere between a rectangular and an elliptical shape as shown in Fig. 3.15.

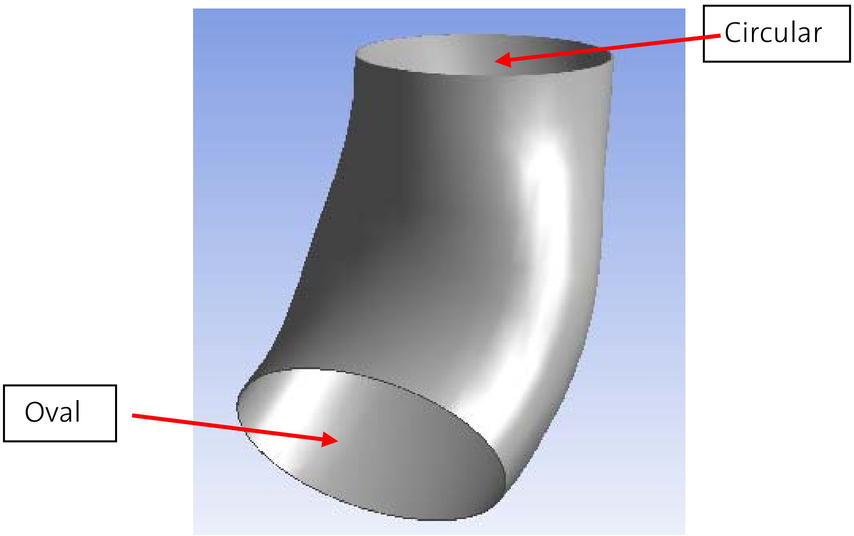

Fig. 3.15 Further optimized Compressor Inlet Duct.

A kidney shaped inlet cross-section can be a solution for further aerodynamic optimization and minimizing the flow separation.
In order to quantify the advantage of the kidney over the elliptic shape, the CFD simulations are performed for both shapes. The kidney shaped inlet is derived from the elliptic shape as can be seen in Fig. 3.16.

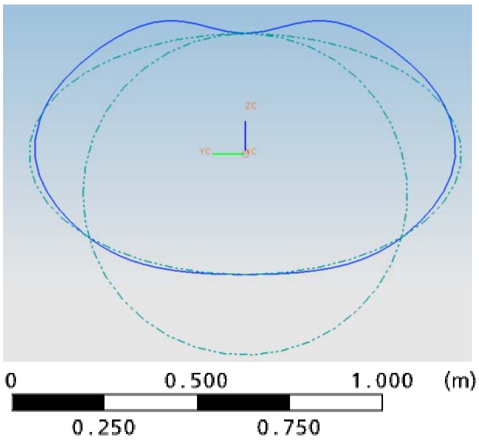

Fig. 3.16 Kidney shaped Inlet Section on the Basis of an Ellipsoid.

It has to be mentioned that only the inlet cross-section shape is modified. The outlet cross-section has to be maintained cylindrical, since this is the interface to the cylindrical casing of the fan. Along the mean line of the scoop, the cross-sections are changing the shape smoothly from kidney shaped at the inlet to cylindrical at the outlet.

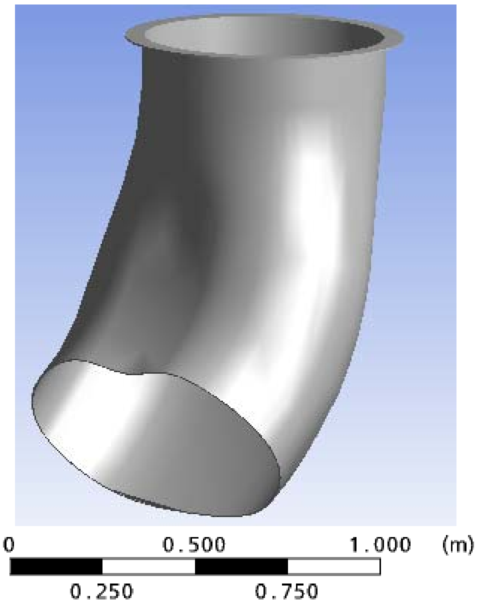

Fig. 3.17 Final optimized Compressor Inlet Duct: Kidney-shaped.

As already mentioned in the previous chapter, the leave out of the entire straight inlet section does not affect the flow much. This leads to the idea to shorten the scoop further, i.e. to shorten the bent section. This leads into smaller scoop dimensions as well as a lower weight. The scoop geometry is trimmed at several locations and studied with CFD. To see how the flow behaves through the scoop, the numerical simulations are performed for wind speeds of 2 and 7 m/s, two marginal cases, as the average wind speed in summer is around 5 m/s. The optimized kidney-shaped compressor inlet duct topology is depicted in Fig. 3.18.
All boundary conditions and solver settings remain the same. Only a new multi-block-structured grid is generated for the new stator geometry as shown in Fig. 3.19 and Fig. 3.20. The CFD results are presented in the following section.

Fig. 3.18 Final optimized Compressor Inlet Duct Topology: Kidney-shaped.

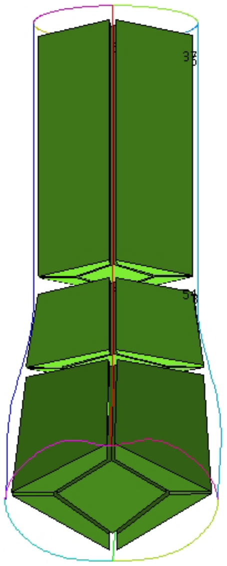

Fig. 3.19 Final optimized Compressor Inlet Duct Grid: Multi Blocking.

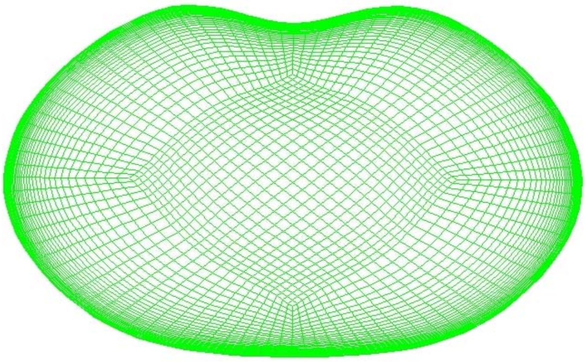

Fig. 3.20 Multi Block Structured Grid: Duct Inlet.

3.6 Comparison

The shape optimization makes a great reduction in flow separation possible and therefore the spot of diffused velocity hitting the fan as it the case for the circular inlet cross-section is greatly reduced. Fig. 3.21 shows the exit plane of the scoop for two different wind speeds, 2 m/s and 7 m/s. Two extreme cases, since the average wind speed at 21'000 km is 5 m/s. The stronger the wind, the more the flow separates. Nevertheless, even at a wind speed of 7 m/s the scoop performs well.

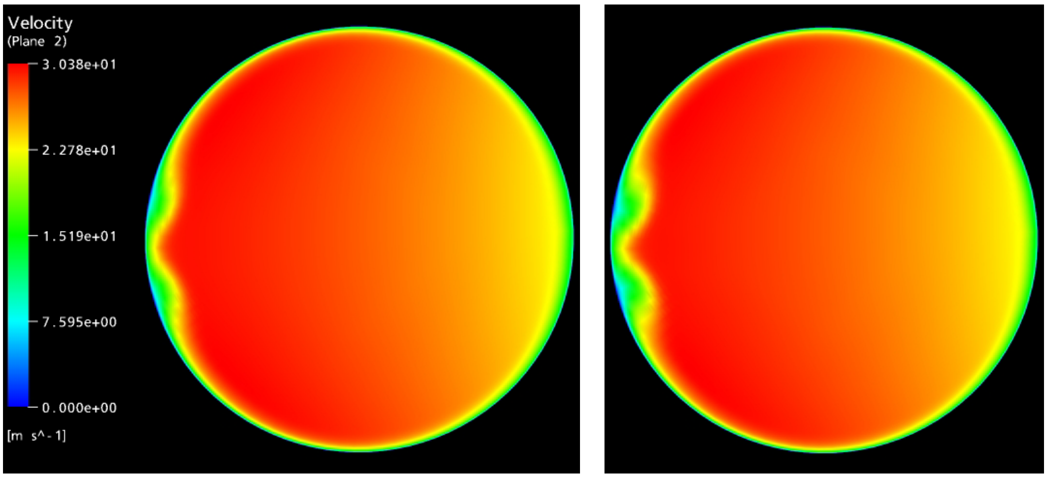

Fig. 3.21 Kidney shaped Inlet Duct Exit Plane for a Wind of 2 m/s (left) and 7 m/s.

The next figures show a comparison of the compressor inlet duct flow for the preliminary design (circular) and the optimized duct geometry (kidney). The cylindrical inlet duct is later trimmed, i.e. the inlet section is shortened, and simulated, in order to make a comparison with the advanced design possible.

The flow in the ducts shown in Fig. 3.22 is visualized by streamlines. In the cylindrical duct on the left, the flow is such, that two big recirculation zones are generated due to the turning, right in front of the fan inlet. This results in a big spot of diffused velocity hitting the fan as shown on the left in Fig. 3.22. Such a distorted fan inlet flow can easily cause the fan to stall. Therefore, the duct inlet section is changed from cylindrical to kidney-shaped. On the right of Fig. 3.22, the flow inside the kidney-shaped duct is as well visualized by streamlines. This beneficial design allows no recirculation zones to arise as for the cylindrical duct. Nevertheless, due to the kidney shape, two swirling streams are created. But, the impact on the fan inlet flow is very small as can be seen in on the right in Fig. 3.22.

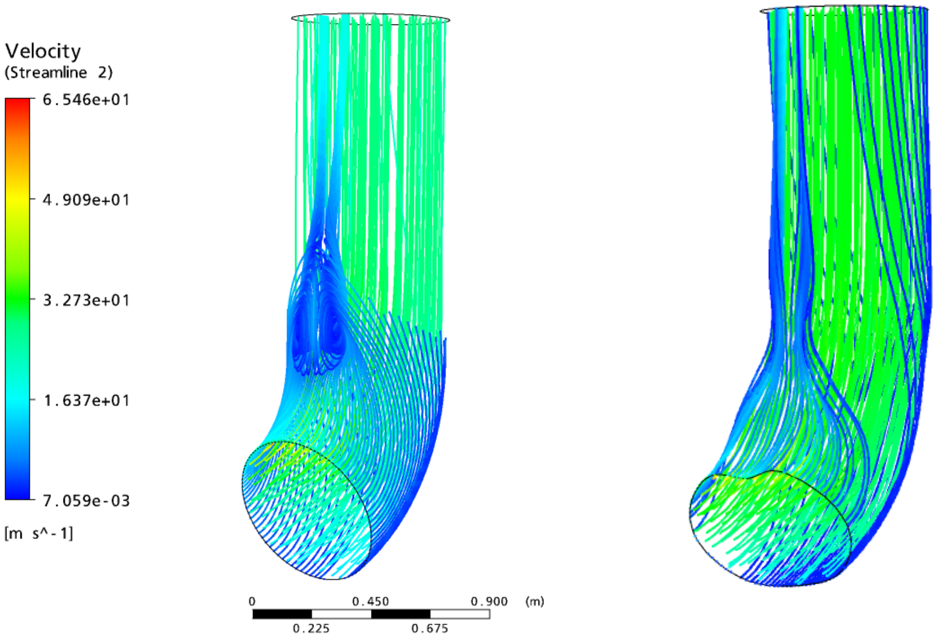

Fig. 3.22 Flow through the different Duct Designs, visualized by Streamlines.

It can be clearly seen that the “trimmed” kidney shaped scoop design leads to best performance. By having the scoop “trimmed”, the turning of the flow is reduced, so that the separation is greatly lowered and therefore also the total pressure losses. From this follows a much better and less distorted fan inlet velocity field, without having any recirculating flow entering the fan as can be seen in Fig. 3.23.

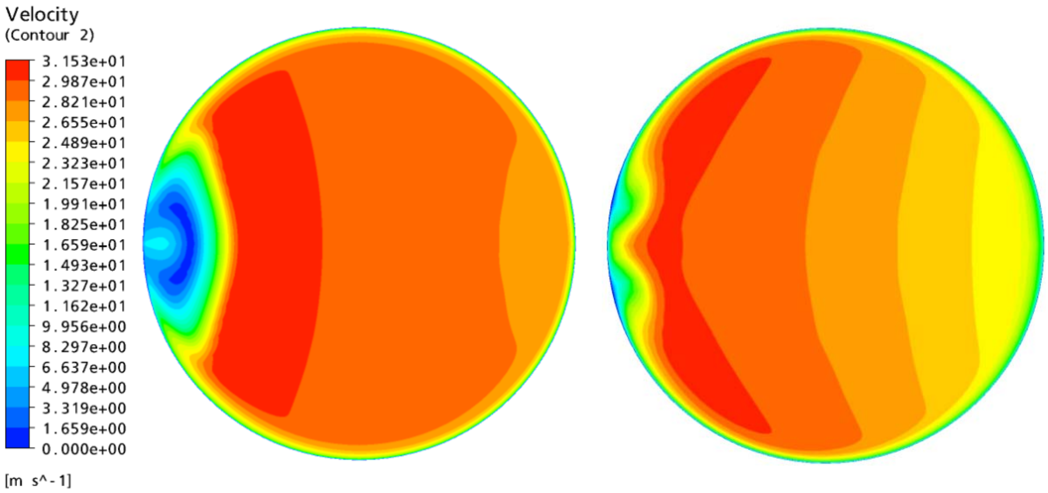

Fig. 3.23 Fan Inlet Flow generated by a Cylindrical Inlet Duct (left) and a Kidney-Shaped Duct (right).

The flow through the two different inlet ducts is shown in Fig. 3.24, visualized by a contour plot of a cross-section through the ducts. On the one hand, the difference in geometry is noticeable and on the other hand the difference in the flow behaviour. Where the flow in the case of the circular inlet cross-section separates heavily with big recirculation zones as previously shown in Fig. 3.22, the flow separation in the case of the kidney-shaped inlet is greatly reduced.

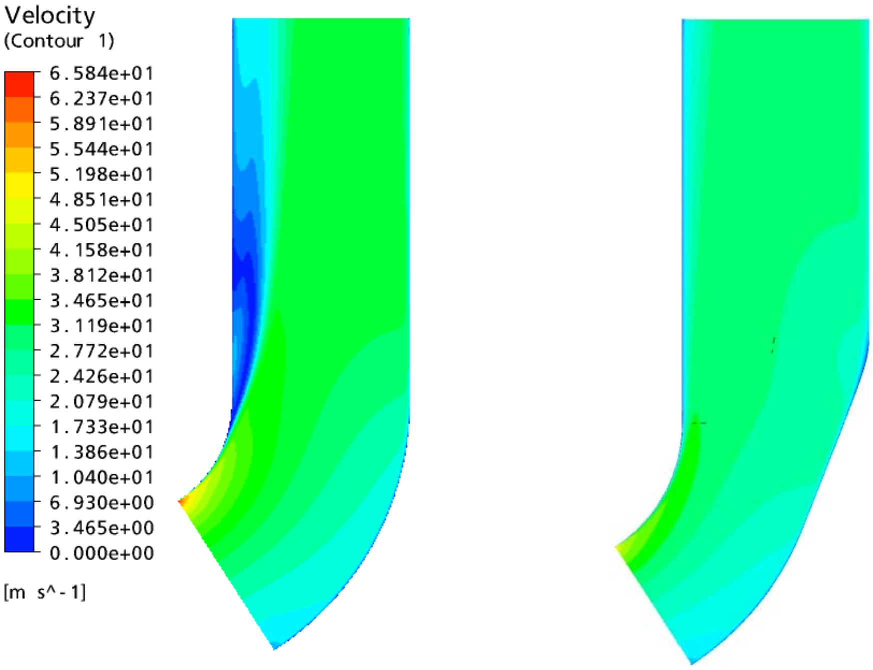

Fig. 3.24 Contour Plots of Flow through the two different Duct Designs (circular (left) and kidney-shaped).

One disadvantage, nevertheless, is the increased fan inlet flow angle. Fig. 3.25 shows the exit flow angle at the location of the fan inlet plane. It can be seen, that the flow is turned more towards the axial direction of the fan in the case of the cylindrical inlet, which is closer to the ideal axial design inlet flow. Certainly, the flow becomes straighter at cross-sections further downstream. But also the spots of diffused velocity become bigger with the growing boundary layer as well as the geometry height and weight is increased.

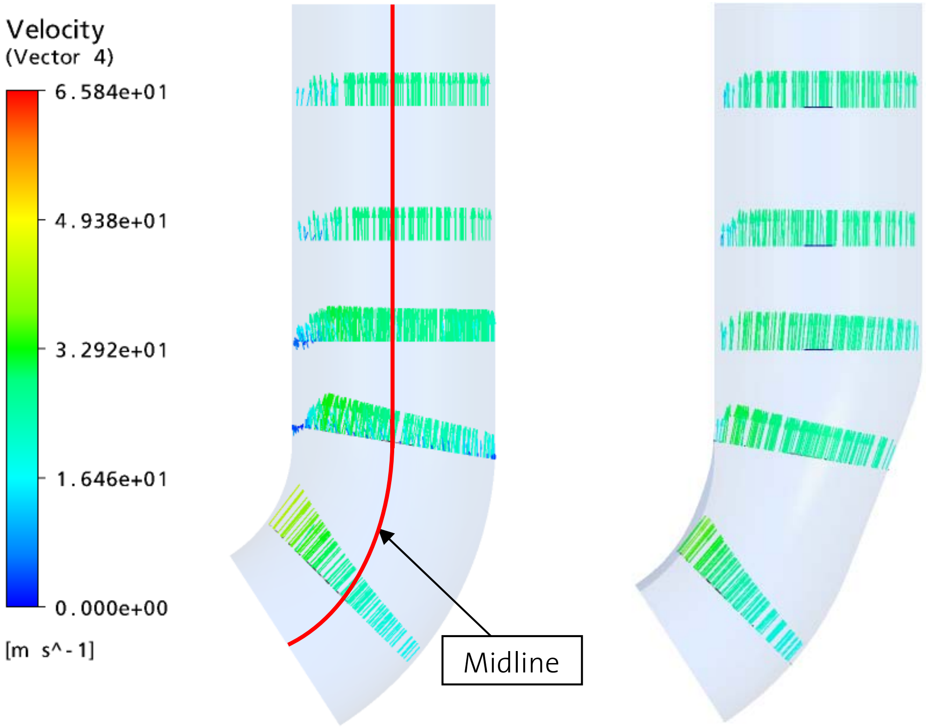

Fig. 3.25 Fan Inlet Flow Directions for the two different Inlet Ducts (circular (left) and kidney-shaped).

The pressure coefficient C_p is computed along the midline (Fig. 3.25) of the two different geometries and compared in Fig. 3.26:

$$C_p = \frac{P - P_{01}}{P_{01} - P_1}$$

Again, it can be clearly seen that the kidney shaped duct performs better than the circular shaped duct. Due to the reduced flow separation, the losses are reduced and therefore higher pressure values are achieved with the optimized design at the area of interest (fan inlet).

Another optimization criterion is the minimization of the total pressure loss between inlet and outlet of the duct. The optimized duct generates a total pressure loss of 2.3 Pa compared to the preliminary design, where 4.6 Pa are lost. Therefore, with the advanced design, the initial pressure loss is reduced by more than 50%. At first sight, 4.6 Pa of total pressure loss are almost nothing compared to common compressor applications. But since the design pressure ratio of the fan is only 1.02 and the ambient pressure at 21'000 km altitude is only 5000 Pa, only a pressure increase of 100 Pa is achieved. Here, a total pressure loss of 4.6 Pa makes 4.6 % of the pressure increase and has therefore to be considered and tried to be minimized.

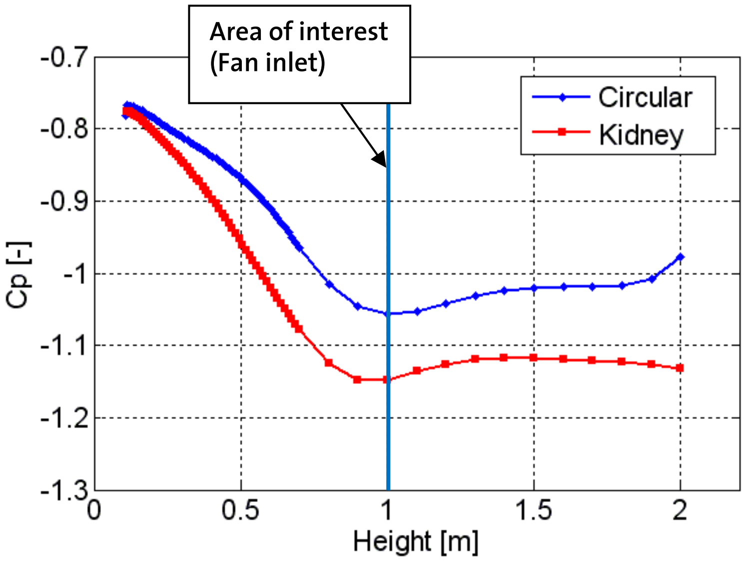

Fig. 3.26 Pressure Coefficient Cp computed along Midline for both Geometries.

Chapter 4

Compressor Design

4.1 Introduction

In order to control the temperature rise due to sun radiation and solar cells as well as to keep the outer blimp inflated, a continuous stream of air is required, passing through the small gap between inner and outer blimps. The fan design project is focused on aerodynamic design, manufacturing and testing of a high volume flow rate axial fan. This fan is supposed to be working continuously at 21 km providing a pressure ratio of 1.01 to 1.05 at a volume flow rate of 6 to 7.5 m^3/s equivalent to mass flow rate of about 0.6 kg/s. Due to the low density of air at high altitude, the fan would be operating at relatively low Reynolds number. The compressor specifications (per fan) are summarized in the following table:

Compressor Specifications	
Mass Flow	0.6 kg/s
Pressure Ratio	1.01-1.05
Power Consumption	1 kW

Table 4.1 Compressor Specifications for a single Fan.

The severe ambient conditions make the compressor operating condition differ from any existing fan and therefore make the fan design very special. The given operating conditions at 21’000 km altitude are found in Table 4.2. These conditions differ totally from the ones at mean sea level. The change in temperature affects directly the Reynolds number and the scaling analysis. For details about similarity and scaling, the reader is referred to chapter 5.3.

Operating Conditions at 21'000 km Altitude	
Ambient Temperature	-60 °C
Ambient Pressure	5000 Pa
Air Density	0.08 kg/m^3

Table 4.2 Air Properties at 21'000 km.

4.1.1 Approaches and Design Steps

A general turbomachinery design always starts with a zero-dimensional analysis where the fan characteristics are specified. In addition to pressure ratio and mass flow rate, the fan needs to operate at a low input power (about 1 kW) and is supposed to be as light as possible with an external diameter of 60 cm, due to structure limitations. The fan has only one single stage (rotor and stator blades) due to its relatively low pressure ratio and in order to minimize the costs, complexity and weight. The designed fan is then scaled down and a 1 : 2.68 model of the fan is tested in the turbomachinery lab (discussed in chapter 5). The compressor design presented in this chapter is based on the 1-D and 2-D design done by Jitendra Singh, which is briefly discussed.

The next design step is the 1-D meanline design. The forced vortex approach has been applied for rotor blade preliminary design while free vortex design has been used for stator blade. The fan characteristics including the degree of reaction, diffusion factor, etc. have been all designed to be within the accepted range. After computing the flow angles, a NACA profile is chosen and the meanline design is continued by calculating the angles at the blade hub and tip.

In the next design step, 2-D design, a commercial tool (AXCAD) is applied to create the full rotor/stator blade geometry. The blades are defined by several cross-sections, mainly at hub, 25 %, 50, %, 75 % of span and at tip. In between, the cross-sections are interpolated.

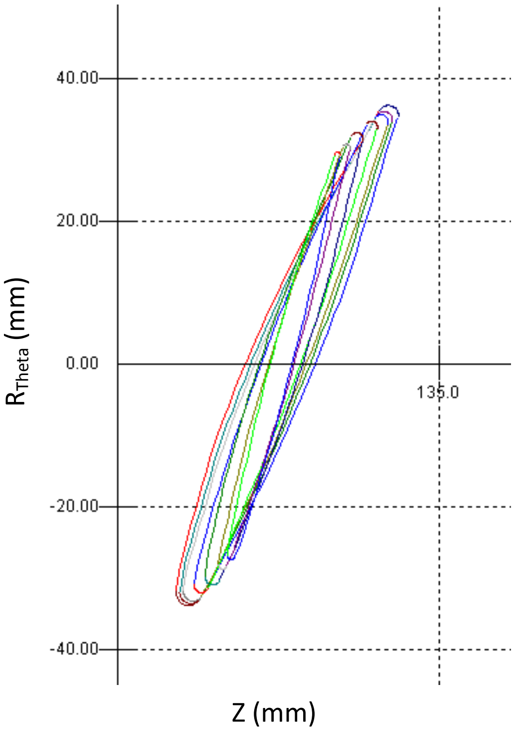

Fig. 4.1 Rotor Profile Stacking.

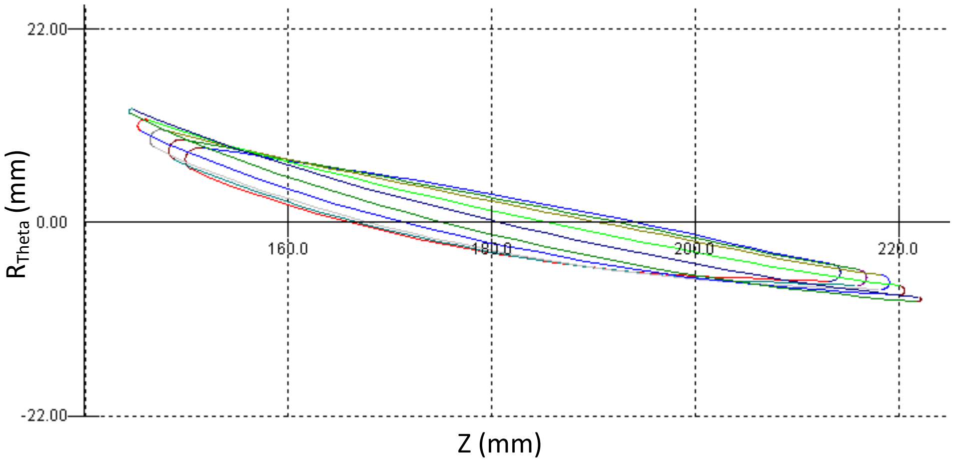

Fig. 4.2 Stator Profile Stacking.

Fig. 4.1 and 4.2 show the rotor and stator profile stacking. These figures illustrate the little twist of the rotor and stator blades. They also show the change in chord length and blade thickness as well as the blade angles. Fig. 4.3 shows the 2-D contour plot in the meridional view. In this view, the position of the two blade rows can be observed. The gap between the rotor and stator row is typically

$$Gap = 0.3 \cdot c$$

where c is the rotor chord at hub.

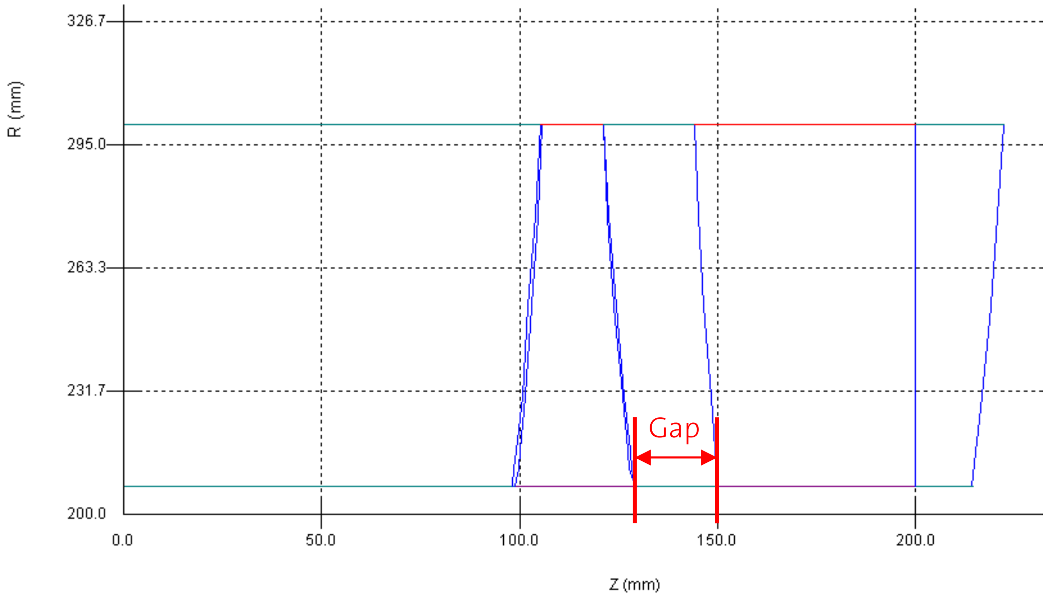

Fig. 4.3 2-D Contour Plot.

4.2 Preliminary Compressor Design

The geometry is then transferred to a CAD program (Unigraphics NX4) to model the entire blisk geometry needed for manufacturing and also for the next steps in the 3-D design:

- Manufacturing: first estimation of cost, lead time and manufacturability
- CFD: flow field and performance prediction
- Structure and vibration analysis

The initial 3-D blade design for the rotor and stator airfoil based on Singh's previous work is presented in the following figures:

Fig. 4.4 Preliminary Rotor Blade Design.

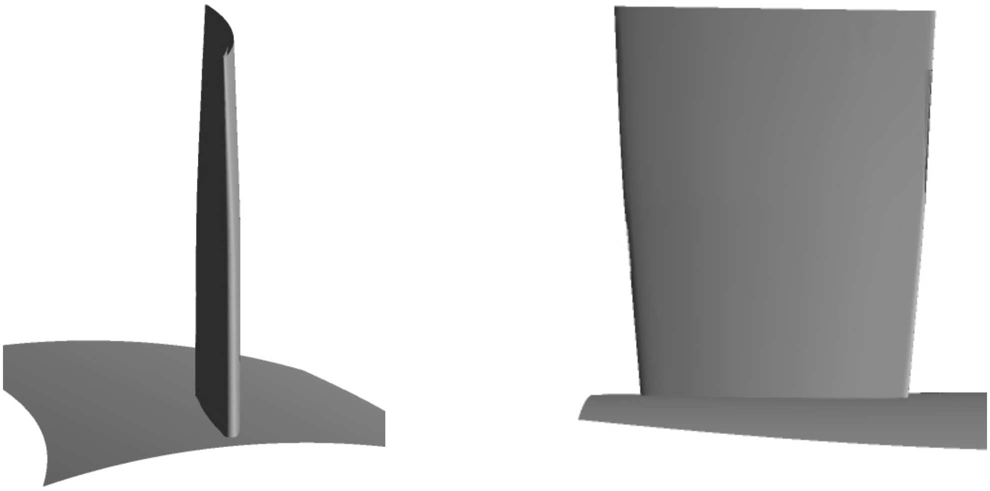

Fig. 4.5 Preliminary Stator Blade Design.

The rotor row consists of 19 blades and the stator row consists of 14 blades. The hub to tip ratio is 0.69. Both, the number of blades as well as the hub to tip ratio is a result of the mean line design. For a tip diameter of 60 cm, this leads to a hub diameter of 41.4 cm and therefore to a blade span of 9.3 cm. The blade length is smaller than typical fan or aero engines with the same size. This is due to high altitude air properties. The following tables summarize the basic design factors of Singh's work for a design mass flow of 0.6 kg/s and a design pressure ratio of 1.05:

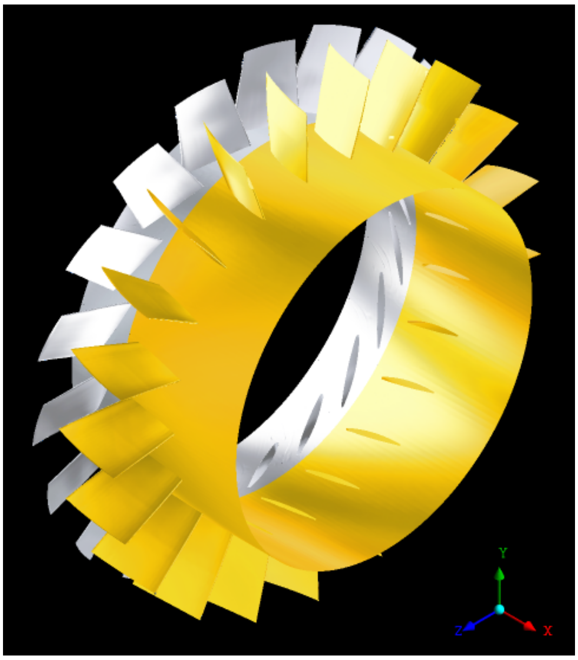

Fig. 4.6 Preliminary Stage Design.

Overview of Preliminary Design Parameters	
Blade Count	19 Rotor / 14 Stator
Fan Outer Diameter	0.6 m
Hub to Tip Ratio	0.69
Blade Span	0.093 m
Tip Clearance (1 % of Blade Span)	0.0093 mm
Gap Rotor Stator	20 mm
Design Rotational Speed	7'000 RPM
Blade Tip Speed	220 m/s
Tip Blade Mach Number	0.77
Axial Velocity	50.63 m/s
Reynolds Number	$3.88 \cdot 10^5$

Table 4.3 Overview of Preliminary Design Parameters.

Overview of Preliminary Design Parameters - Rotor

	Hub	Mid	Tip
Chord	75.4 mm	66.6 mm	58.9 mm
Solidity	1.34	0.95	0.72
β_1	69.85 °	73.32 °	75.79 °
B_2	65.60 °	70.78 °	74.87 °
Turning	4.25 °	2.54 °	0.93 °
Reaction	0.86	0.93	0.97
Flow Coefficient	0.39	0.3	0.23
Loading Coefficient	0.2	0.13	0.1
Diffusion Factor	0.155	0.188	0.220
De Haller Number	0.89	0.88	0.87

Table 4.4 Overview of Preliminary Design Parameters - Rotor.

Overview of Preliminary Design Parameters - Stator

	Hub	Mid	Tip
Chord	7.70 mm	7.80 mm	9.60 mm
Solidity	0.83	0.69	0.71
α_2	18.89 °	23.87 °	29.69 °
α_3	9.09 °	7.44 °	6.30 °
Turning	9.80 °	16.42 °	23.39 °
Diffusion Factor	0.300	0.380	0.403
De Haller Number	0.90	0.92	0.94

Table 4.5 Overview of Preliminary Design Parameters - Stator.

CFD is applied using the Turbo Mode of the commercial Software Package of ANSYS CFX to predict the flow and performance of the fan. ICEM-CFD is used for grid generation and the initial and boundary conditions are then specified in CFX pre-processor. Through an iterative process the flow is simulated and results are analyzed in a post-processor.

4.3 CFD Analysis

4.3.1 Grid Generation

ANSYS ICEM CFD is used for the stage mesh generation. The rotor and the stator are meshed independently and merged together for simulations using an interface. For both a block structured mesh is generated. The next section gives information about the way the grid is generated and where the challenges are, producing Turbomachinery grids with ICEM CFD.

Used Technique

After preparing the 3-D blade configuration in Unigraphics NX4, the geometry is imported into ICEM for mesh generation. This is done through the ICEM Direct CAD interface for Unigraphics. This interface allows a definition of solid bodies, surfaces to be extracted, relevant curves and points, directly in the CAD environment. The different geometry families can be easily selected and a geometry definition file for ICEM can be written. Since this interface is not available, the export must be done via third-party formats like Parasolid, which require redefinition of the different geometry families under ICEM, which is a time consuming process. Another disadvantage of using third-party format is the required geometry cleanup, which is very small when exporting through the interface. Once this geometry file is available, ICEM can be run to start generating the grid. The first step here, as already mentioned, is the geometry cleanup. At first, the automatic repair tool is applied, where multiple curves, missing curves and holes in the surface are looked at. At this point, new surfaces can be introduced, others can be deleted, using different tools in ICEM.

At this point an optional step can be taken and is recommended. Sometimes ICEM generates one volume mesh for two different bodies. The mesh is valid, but separate access to the two bodies is needed. A remedy to this problem is to define different bodies clearly in the ICEM environment by defining material points within the bodies. In the present case, the solid blade is defined as a body by a material point and the blade surrounding volume, the flow region, is defined by a another material point as another body. The importance of material points definition becomes crucial when dividing the bodies into blocks. This allows an easy selection and handling of the different blocks.

Blocking

The first step after geometry treatment is the definition of the mesh sizes on the different surfaces. The second step is to apply the multi blocking technique, necessary to get a high quality surface mesh. The control volume is divided into several blocks in order to obtain a smooth O-grid around the blade as shown in Fig. 4.7.

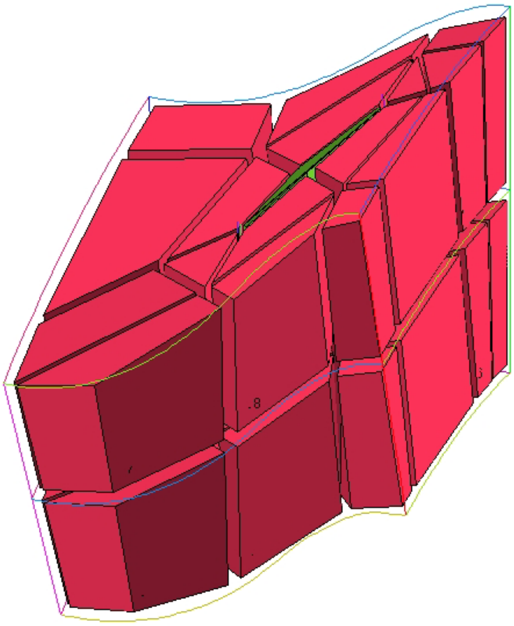

Fig. 4.7 Rotor Domain Multi Blocking.

For the present grid, the points of the surface mesh are chosen to be mapped leading to a structured mesh, where the volume is filled with hexahedras. Finally the so-called pre-mesh is converted into a primary mesh. This mesh then has to be optimized in terms of quality, aspect ratio and skewness using a smoothing tool in ICEM. The rotor domain grid consists of 163’560 elements and 175’525 nodes and the stator domain grid consists of 331’992 elements and 349’752 nodes. The grids for the two domains are imported into the pre-processing environment of CFX Pre Turbo to set the boundary conditions. The y^+ values are in the required range for the turbulence model and solver used in the present work as, discussed in section 4.3.4. Fig. 4.8 and Fig. 4.9 show the resulting mesh of the rotor and stator domain.

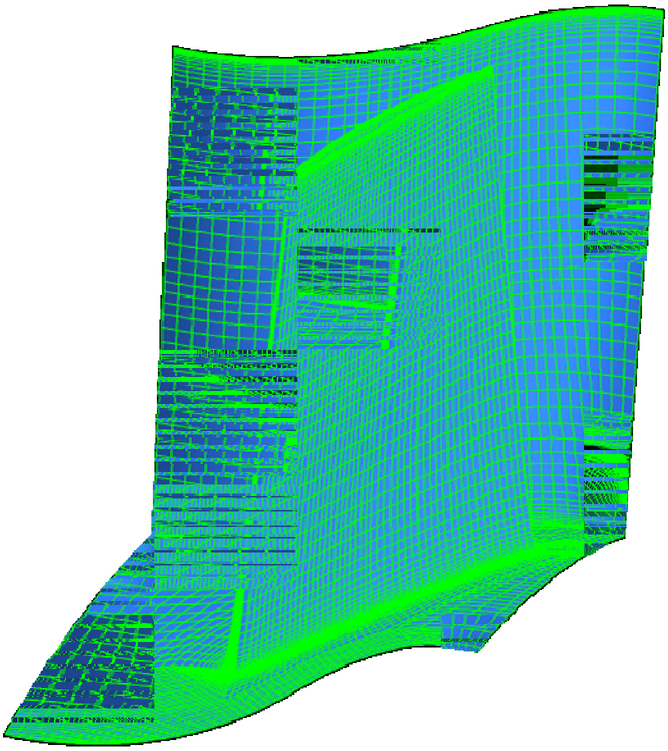

Fig. 4.8 Rotor Domain Grid.

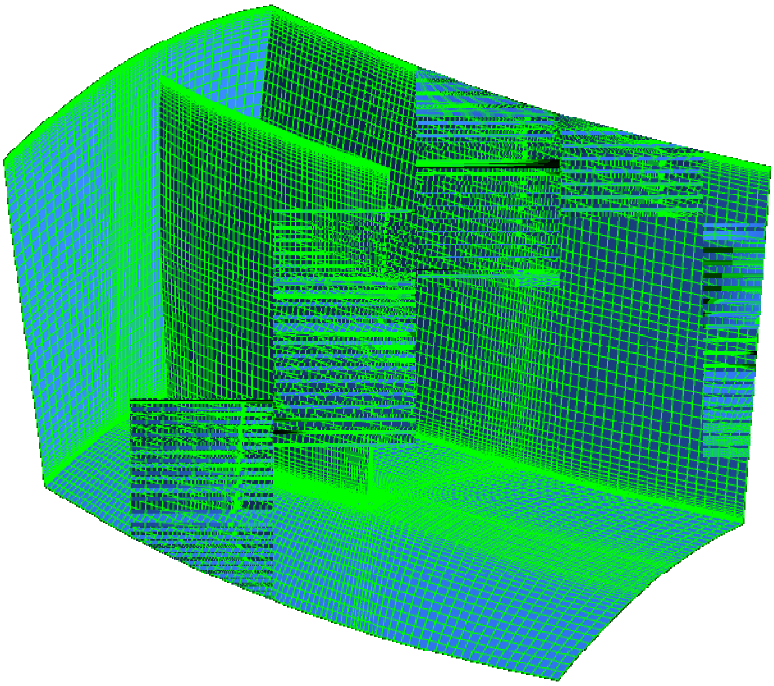

Fig. 4.9 Stator Domain Grid.

4.3.2 Boundary Conditions

When pre-processing in CFX Turbo Mode, the different fluid and solid domains are defined, before setting the boundary conditions and the solver parameters. At the end, the solver definition file is created.

The type of simulation is set to steady-state and the mesh files are loaded. CFX Turbo recognises the names of the mesh regions automatically as potential boundaries and interfaces. The following boundary conditions are set:

Boundary	Parameter	Value
Inlet	Boundary type	Subsonic Inflow
	Stat. Frame Total Pressure (relative Pressure)	97.54 Pa
	Static Temperature	216 K

Outlet	Boundary type	Subsonic Outflow
	Average Static Pressure	Variable

Table 4.6 Stage Boundary Conditions.

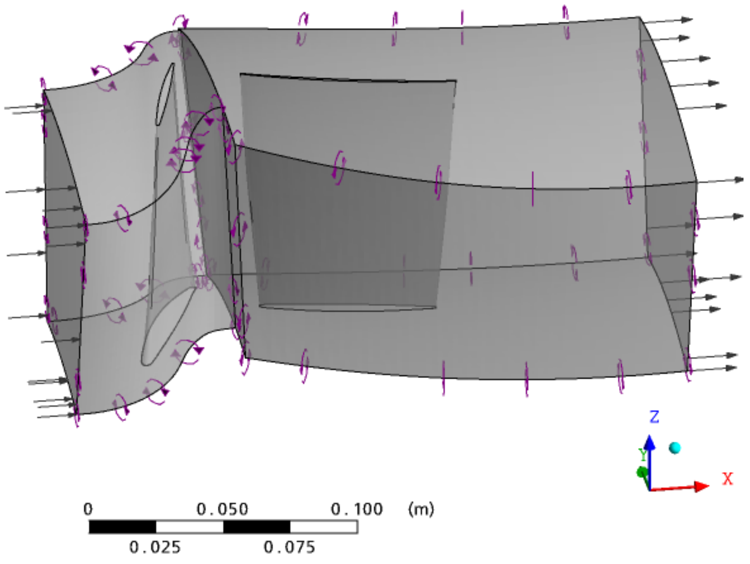

Fig. 4.10 Compressor Stage Topology and Boundary Conditions.

Fig. 4.10 shows the stage topology and the opposed boundary conditions. The particular combination of total pressure definition at the inlet and an average static pressure at the outlet yields stable results.

Then the flow field (fluid domain) is defined and the following parameters are set:

Parameter	Value
Fluid	Air ideal gas
Reference Pressure	5000 Pa
Heat transfer model	Thermal Energy
Turbulence model	k-epsilon
Turbulence Intensity	5 %

Table 4.7 Definition of Fluid and Turbulence Model.

4.3.3 Domain Interface Setup

When specifying domain interfaces in the CFX Turbo pre-processor, the type of analysis has to be selected that will be carried out in the solver. The choices are Frozen Rotor, Stage, and Transient Rotor Stator as described in the following. The present simulations are all performed with a Stage interface as this is the most suitable interface for the present application.

Frozen Rotor

The Frozen Rotor model treats the flow from one component to the next by changing the frame of reference while maintaining the relative position of the components. Usually, periodicity is used to reduce the number of components to a subset that has approximately the same pitch ratio as the full geometry. To account for differences in pitch ratio between the subset and the full geometry, the flow passing through the interface is scaled according to the net pitch ratio of the subsets.

The Frozen Rotor model must be used for non-axisymmetric flow domains, such as impeller/volute, turbine/draft tube, propeller/ship and scroll/volute cases. It can also be used for axial compressors and turbines. The Frozen Rotor model has the advantages of being robust, using less computer resources than the other frame change models, and being well suited for high blade counts. The drawbacks of the model include inadequate prediction of physics for local flow values and sensitivity of the results to the relative position of the rotor and stator for tightly coupled components.

Stage

The Stage model circumferentially averages the fluxes in bands and transmits the average fluxes to the downstream component. Possible applications include axial turbines, compressors and pumps, as well as fans and torque converters. The model is useful for large pitch ratios and still takes a relatively short time to solve. The model is not suitable for applications with tight coupling of components and/or significant wake interaction effects and may not accurately predict loading.

Transient Rotor-Stator

The Transient Rotor-Stator model takes all of the transient flow characteristics into account. A sliding interface is used to allow a smooth rotation between components. As with the Frozen Rotor model, the Transient Rotor-Stator model scales the flow from one component to the next in order to account for a non-unity net pitch ratio. This model is robust and yields high accuracy predictions of loading. The drawbacks include high computational cost and large amounts of storage required to hold the transient data.

4.3.4 Turbulence Model and Solver Setup

The software used for the CFD investigation is the commercial ANSYS CFX software. The ANSYS Solver is a coupled solver which solves the hydrodynamic equations as a single system. This solution approach uses a fully implicit discretization of the equations at any time step. For stationary problems the time step behaves like an acceleration parameter to guide the approximate solutions in a physically based manner to a steady state solution.

The widely used industry-standard $k - \varepsilon$ turbulence model is used as also advised by the ANSYS CFX Turbo guide for compressor applications. This turbulence model leads to a stable solution of the set of equations. Heat transfer and viscous work are modeled using the Total Energy heat transfer model and enabling the Viscous Work Term option in CFX-Pre.

Timestep

A good estimate of the timestep is within the region $\frac{0.1}{\omega}\ to\ \frac{1}{\omega}$, where ω is the angular velocity of the rotating domain in radians per second. The option automatic timestep is selected, resulting in a timestep of $\frac{0.2}{\omega}$.

Convergence

For high speed compressors where a specified mass flow outlet boundary condition is applied, the flow can "choke" when the velocity approaches Mach 1 at throat, resulting in possible solver failure. A suggested workaround to this problem is to run the simulation using a static pressure outlet, which is more stable.

The optimal performance characteristics can be determined by creating a curve of pressure ratio versus flow rate. In Fig. 4.11, Region 1 shows an area where a large change in mass flow rate represents a small change in pressure rise. When modeling flow in this region, a mass flow rate specified outlet is better than a pressure specified outlet. Region 2 shows an area where a small change in flow rate represents a large pressure variation. This region is close to "choking", and a pressure-specified outlet is the best choice.

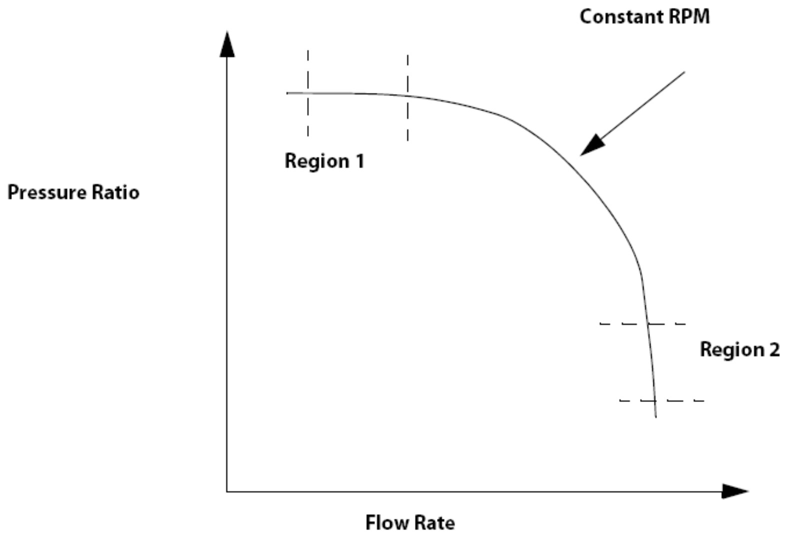

Fig. 4.11 Flow Rate vs. Pressure Rise for a Gas Compressor. (ANSYS 2007)

4.3.6 Convergence Quantification

Solver Residual

The residual is a measure of the local imbalance of each conservative control volume equation. It is the most important measure of convergence as it relates directly to whether the equations have been solved. The residual is calculated using only the spatial flux terms and essentially represents a discrete conservation balance. The following residual plot representatively shows the convergence history of the stationary simulations:

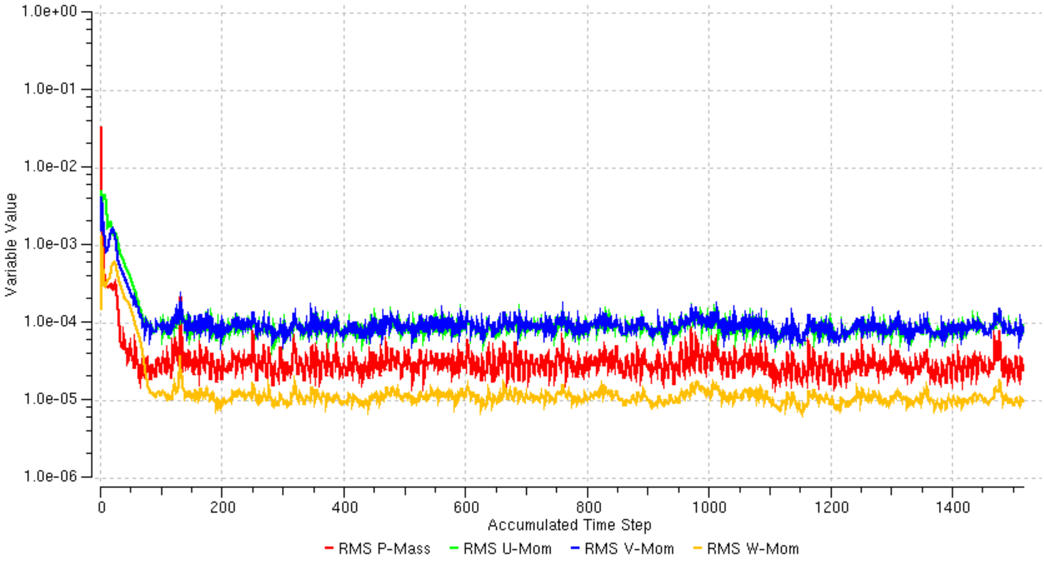

Fig. 4.12 RMS Solver Residuals.

According to the CFX Solver Guidelines a decrease of the RMS residuals of the main kinematic properties of at least three orders of magnitudes is required.

4.4 Preliminary Results

In this study, no tip gap leakage flow is considered. This section presents the CFD results for simulations based on Singh’s preliminary blade design. The idea is to validate the design in terms of airflow and performance before modifications and manufacturing. The structure and vibration analysis is discussed in chapter 4.5. The next figures show the flow field through the stage at hub, midspan and tip for the stationary and absolute frame of reference. The rotor performs really well, receiving the flow at right angles, where the stator shows big flow separation at hub and tip (suction side). Based on these results, the stator blade needs to be optimized.

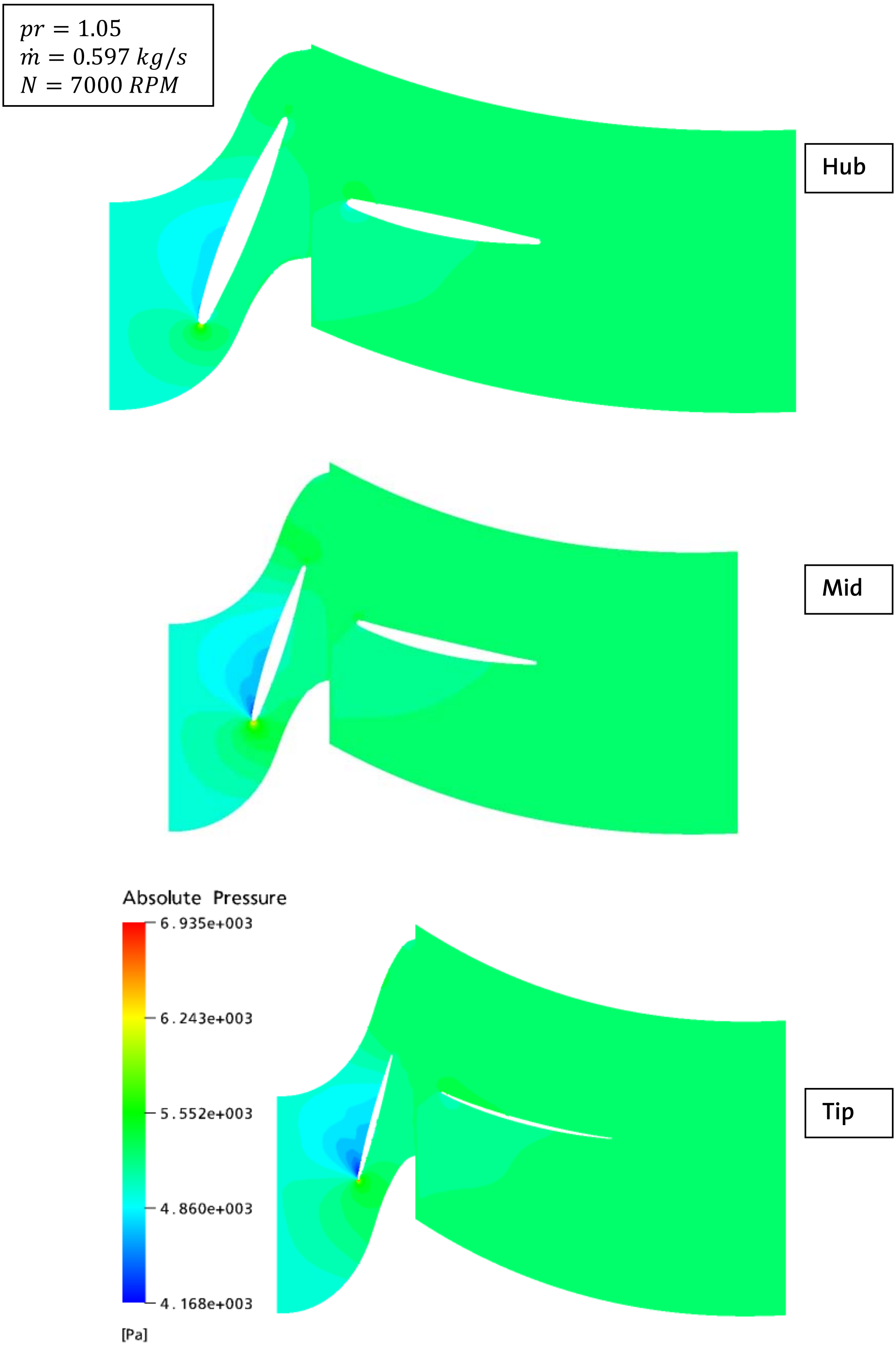

Fig. 4.13 Blade to Blade View: Absolute Pressure.

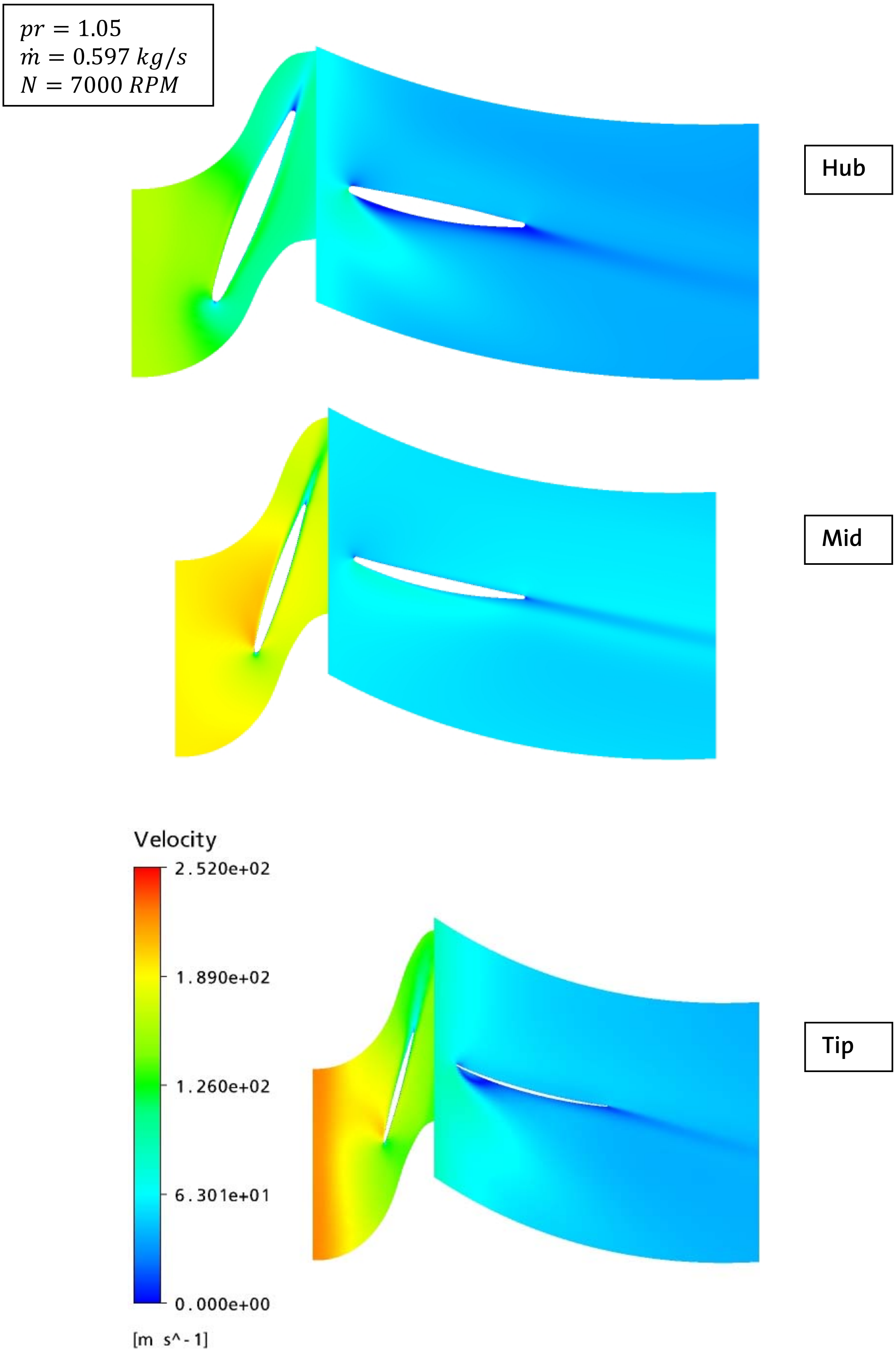

Fig. 4.14 Blade to Blade View: Velocity in Relative Frame at.

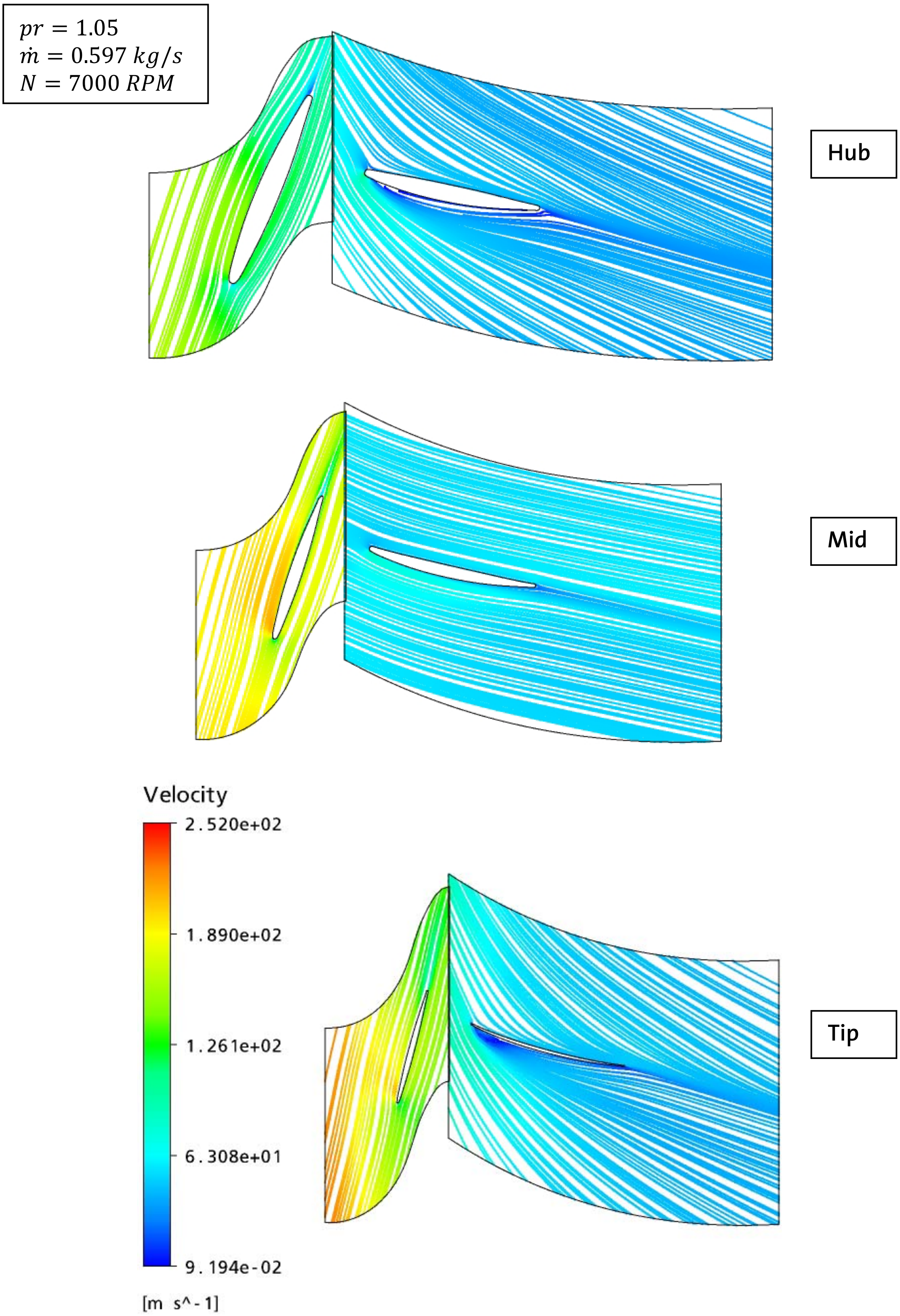

Fig. 4.15 Blade to Blade View: Velocity in Relative Frame (Streamlines).

The separation at tip and hub is shown again in Fig. 4.16, where the flow is visualized by streamlines. It is found by analysing the stator flow and blade angles, that the stator receives the flow at hub and tip at wrong angles, leading to a flow separation. A possible way to avoid or reduce the separation is to turn the blade more into the flow by changing the blade incidence and stagger angle.

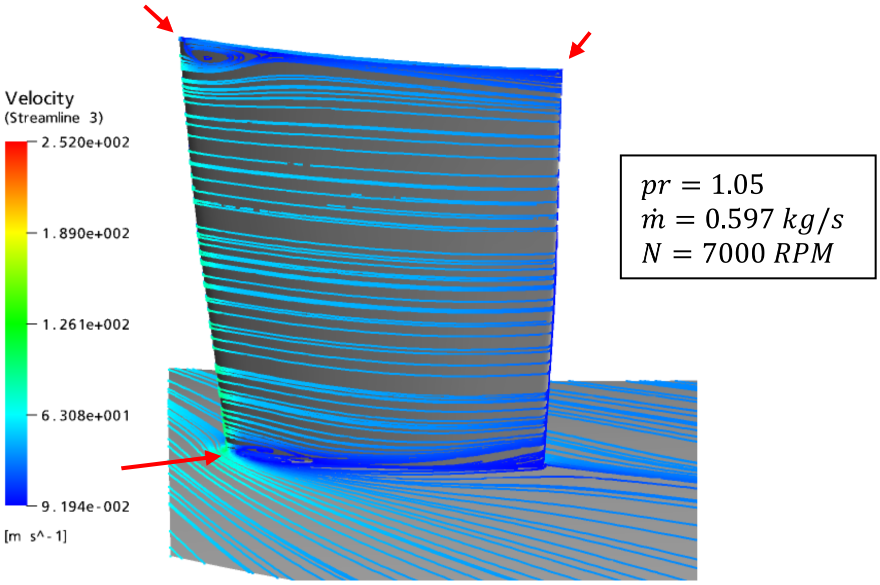

Fig. 4.16 Flow around a Stator Vane (Preliminary Design).

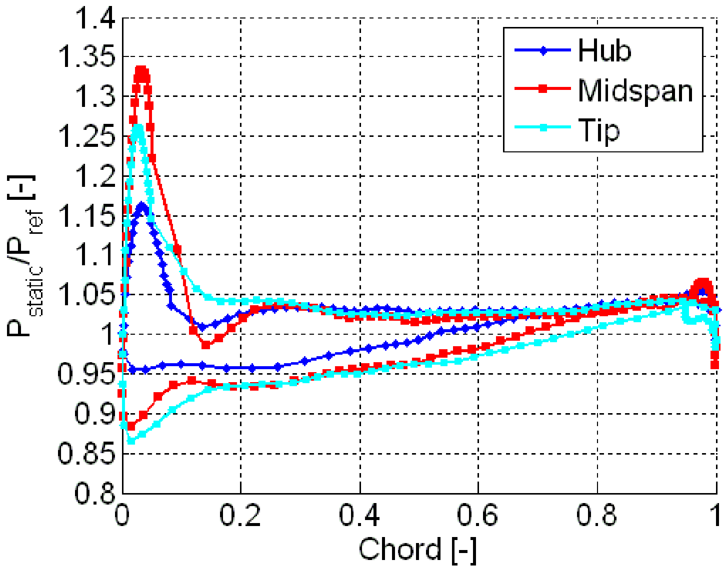

Fig. 4.17 Rotor Blade Loading at Hub, Midspan and Tip.

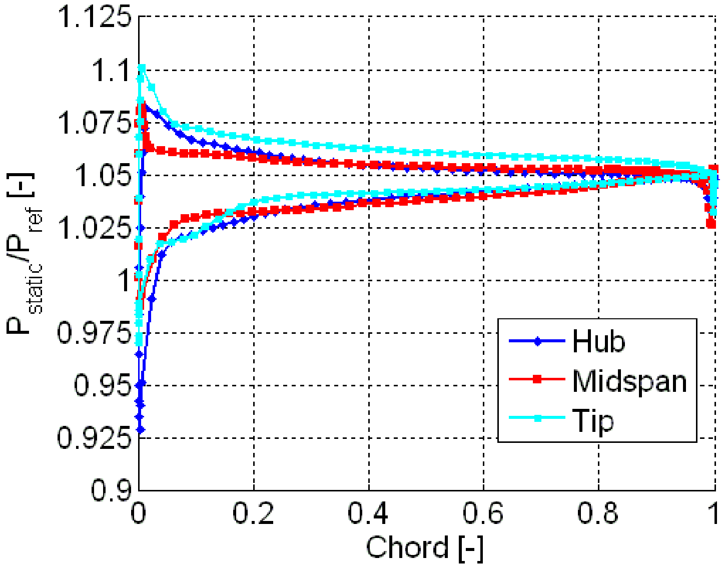

Fig. 4.18 Stator Blade Loading at Hub, Midspan and Tip.

The blade loading (force exerted on the blade) is another parameter to check the quality of a blade design. The profile loading shown in Fig. 4.17 and 4.18 is non-dimensionalized with the reference pressure and plotted versus chord for the rotor and stator blade. A high blade loading becomes critical at tip, since the tip leakage vortex is related to the loading. The highest loading at tip is found at approximately 3 % of chord. The present stage computation does not include any tip clearance and therefore no conclusions can be made about a possible tip vortex flow.

The change of fan pressure ratio versus passage mass flow rate at various rotational speeds, known as compressor map, is plotted in Fig. 4.19. The pressure ratio increases when the mass flow rate is reduced. Pressure rise can be also achieved by means of increase in rotational speed. In order to choose the operating conditions of the fan, Fig. 4.19 plays an important rule. Due to the material constraints of the high altitude application, the interior pressure ratio should be kept under 1.02-1.03. Higher pressure ratios may damage the interior blimp. Nevertheless, the flow will have a significant pressure loss while passing through the passage and therefore the fan is designed so that it can provide higher pressure ratios if required. To meet the given compressor specifications, the compressor has to be run on speed lines between the two speed lines shown in Fig. 4.19.

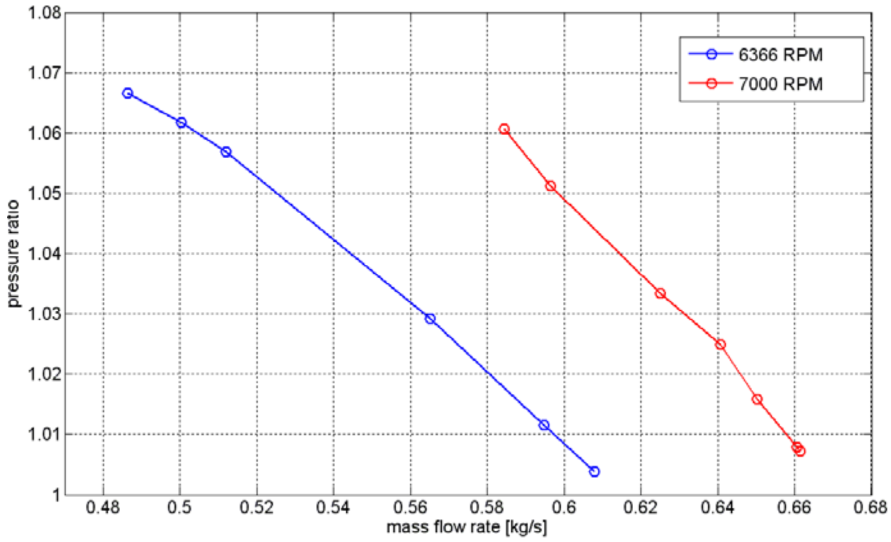

Fig. 4.19 Pressure Ratio vs. Mass Flow Rate plotted for two Speed Lines.

The pressurized air is expected to flow through a narrow passage between the exterior and interior blimps. Due to the high losses the 1.02 pressure rise is not enough to provide the required mass flow rate. In this case a higher pressure ratio will be required to make sure that adequate amount of air will pass through the layers. Increasing the pressure ratio can be easily achieved since the designed fan is able to provide pressure ratios up to 1.07 before the instabilities degrade the fan performance. Nevertheless, there is a problem with the power requirements. There is a linear correlation between the fan power and the pressure ratios (Fig. 4.21). The fan power is a function of mass flow rate, efficiency, pressure ratio, and air properties, based on the first law of thermodynamics. The power needed to compress a certain air mass flow rate from a pressure P_{01} to P_{02} can be visualized as shown in Fig. 4.20 and expressed as:

$$P_{Shaft} = \dot{m} \cdot \frac{c_p T_{01}}{\eta_c} \cdot \left[\left(\frac{P_{02}}{P_{01}} \right)^{(\gamma-1)/\gamma} - 1 \right]$$

Fig. 4.20 Black Box: Compression of Air.

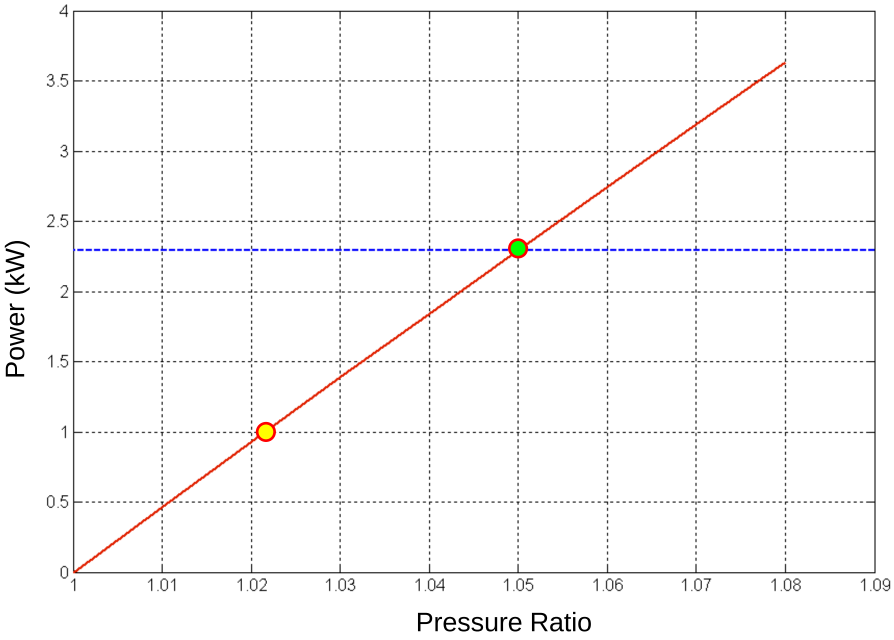

Fig. 4.21 Correlation between Power Consumption and Pressure Ratio for a single Fan.

Increasing the pressure ratio will significantly increase the power consumption. Fig. 4.21 shows the correlation between the pressure ratio and power. For a pressure ratio of 1.05, the power consumption will be about 2.3 kW per fan, which is relatively higher than requested 1 kW limit.

Fig. 4.22 shows the isentropic efficiency plot for the above computed speed lines. The highest efficiency of approximately 69% is reached for the highest pressure ratio of 1.07 which is nevertheless very close to stall condition. Higher efficiencies or a continuation of the efficiency and speed lines towards higher pressure ratios are expected when optimizing the in terms of flow separation and stability. The reader is referred to chapter 4.6 for results obtained by an optimized stator design.

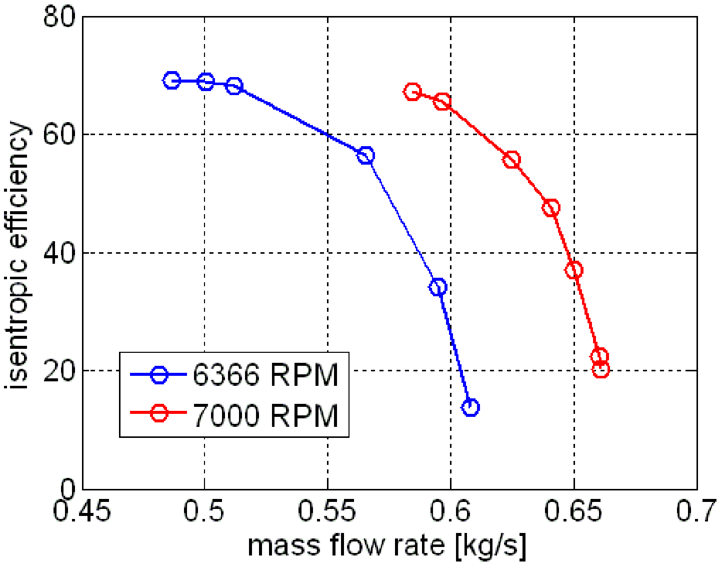

Fig. 4.22 Isentropic Efficiency vs. Mass Flow Rate plotted for two Speed Lines.

4.5 Mechanical Design

A stress analysis is presented for a one stage compressor rotor design and it's scaled down model for the experimental setup presented in chapter 5. The analysis consists of the one-dimensional pre-analysis to support the design layout and the follow-on three-dimensional finite element analysis to confirm the blade design at operating loading conditions.

The one-dimensional stress analysis treats the blade as a cantilever beam. A prismatic bar, rotating about an axis through its end with an angular velocity ω. The analysis allows a quick calculation of the average centrifugal stress at the blade sections and provides the basis for blade section sizing.

At any radius, the stress in the bar due to centrifugal force will be

$$\sigma = \int_{r}^{r_T} \rho\omega^2 r\, dr = \frac{\rho\omega^2}{2}(r_T^2 - r^2)$$

Near the axis of rotation occur the highest stresses

$$\sigma = \frac{\rho(\omega r_T)^2}{2}$$

For a blade tip speed ωr_T of 216 m/sec (Scaled down model, chapter 5.3) and a density ρ of 2780 kg/m^3 for the aluminium used, this implies a stress of $\sigma = 0.65 \cdot 10^8 N/m^2$. Close to the strength limit of the material, $\sigma = 4.2 \cdot 10^8 N/m^2$, so that care in design is required.

ANSYS Simulation Environment

The ANSYS Workbench 10 platform is an environment that offers an efficient and intuitive user interface, CAD integration, automatic meshing, and access to model parameters as well as to the functionalities available within the ANSYS Mechanical products.
Mechanical simulation with ANSYS Workbench builds upon the core ANSYS solver technology and offers the following benefits for advanced analysis:

- High-end desktop environment for all ANSYS technologies from static linear analysis to nonlinear rigid/flexible dynamics, from steady state thermal analyses to coupled thermo-mechanical transient studies

- Tight integration with other ANSYS solutions (Geometry disfeaturing & modelling, Design Exploration, Fatigue Analysis, Computational Fluid Dynamics, ANSYS Meshing Technologies)

- Fully automated connection detection and creation (contact, joints)

ANSYS Mechanical solutions offers, a range of linear and nonlinear materials technology to handle composites, plasticity, hyper elasticity and specialized materials such as cast iron, shape memory alloys and cohesive zone models.
Mechanical solutions offer advanced dynamics technology by enabling calculations of a product's dynamic response to time or frequency varying inputs. The capability is used over a broad range of application areas for modal, harmonic, transient and random vibration analysis.

ANSYS provides a complete set of solver technology for both serial and parallel computing. Large scale computing is achieved via parallel processing, iterative and domain-based solvers. With Distributed ANSYS, the entire solution phase runs in parallel, including the stiffness matrix generation, linear equation solving.

4.5.1 Rotor Blisk Stress Analysis

The three-dimensional finite element analysis to confirm the blade design at operating loading conditions is performed using the introduced commercial Software Package ANSYS Workbench 10.

The 3-D model is easily imported into the CAD environment where no further editing is necessary. This step is followed by a meshing procedure, where a refined mesh is obtained as depicted in Fig. 4.23. The next step is to set the correct material properties for aluminium Haba 50 and to set environment and boundary conditions as depicted in Fig. 4.24 on the basis of the scaled model.

Cylindrical Support	
Radial	Free
Axial	Free
Tangential	Fixed

Rotational Velocity	
X-Component	25’000 RPM
Y-Component	0
Z-Component	0

Table 4.8 Structure and Vibration Analysis Boundary Conditions.

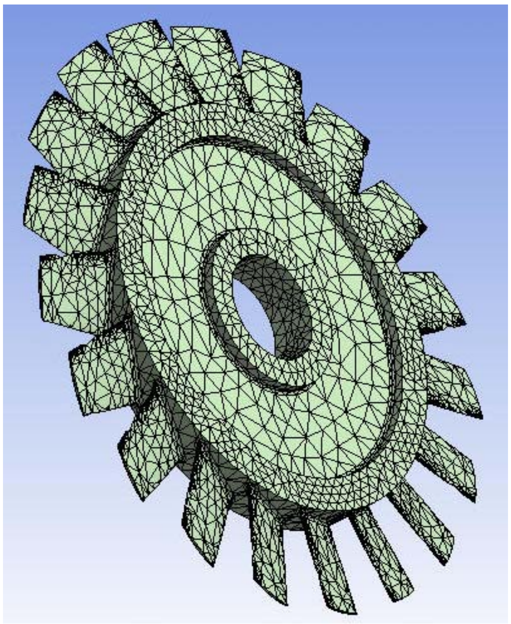

Fig. 4.23 Refined Mesh for all Computations.

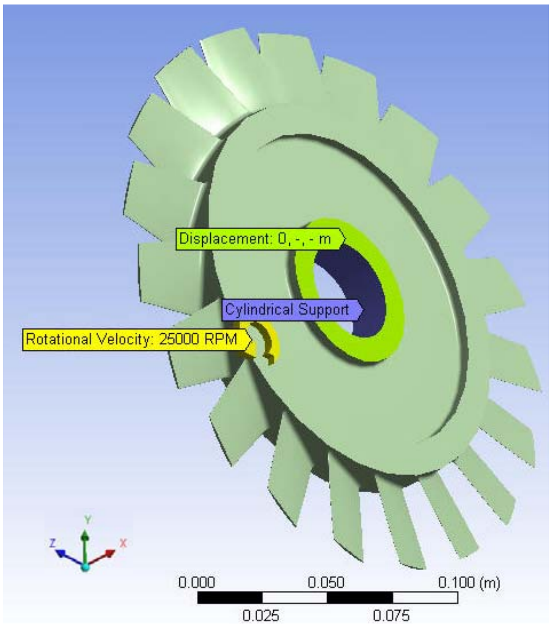

Fig. 4.24 Boundary Conditions for the Computational Domain.

The reference temperature of the environment as well as the thermal condition of the rotor blisk for the scaled down model is set to 25 °C and to -60 °C for the high altitude version.

The values of interest are first the equivalent von Mises stress and the directional deformations. Rotor vibrations are calculated in a later step, and are introduced in the next section.

The equivalent von Mises stress σ_v, or simply Mises stress, is a scalar function of the deviatoric components of the stress tensor that gives an appreciation of the overall magnitude of the shear components of the tensor. This allows the onset and amount of plastic deformation under tri-axial loading to be predicted from the results of a simple uni-axial tensile test. It is most applicable to ductile materials.

$$\tau_0 = \frac{\sqrt{2}\sigma_0}{3}$$

where τ_0 is the allowable shear.

Plastic yield initiates when the Mises stress reaches the initial yield stress in uni-axial tension and, for hardening materials, will continue provided the Mises stress is equal to the current yield stress and tending to increase. Mises stress can then be used to predict failure by ductile tearing. It is not appropriate for failure by crack propagation or fatigue, which depend on the maximum principal stress.

In 3-D, the Mises stress can be expressed as:

$$\sigma_v = \sqrt{\frac{(\sigma_1 - \sigma_2)^2 + (\sigma_2 - \sigma_3)^2 + (\sigma_3 - \sigma_1)^2}{2}}$$

where $\sigma_1, \sigma_2, \sigma_3$ are the principal stresses.

The von Mises stress for the high altitude fan and its scaled down model is calculated by ANSYS Workbench and presented in Fig. 4.25 and Fig. 4.26. As expected and as a result of the introduced one-dimensional analysis on a prismatic bar, the stress at the blade tip is minimal and finds its maximum at the smallest radius of the disk, since the stress is a function of r^2. The maximal occurring von Mises stress is in the case of the scaled model $\sigma_{vmax} = 1.216 \cdot 10^8$ Pa. Hence, even at a rotational speed of 25’000 RPM, which is 14% higher than the design speed of 22’000 RPM, a safety factor of 3.45 is guaranteed. In the case of the high altitude fan, the maximal occurring von Mises stresses are $\sigma_{vmax} = 7.123 \cdot 10^7$, at the design rotational speed of 7’000 RPM, leading to a safety factor of 4.733.

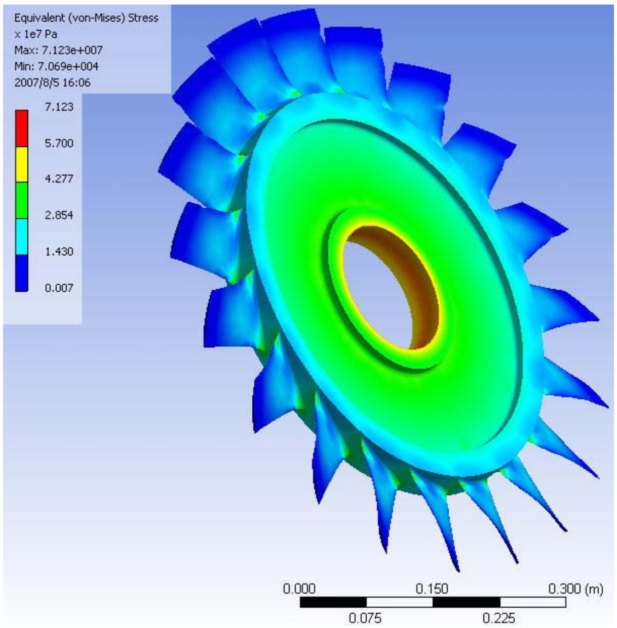

Fig. 4.25 Von Mises Stresses for the High Altitude Blisk at a Rotational Speed of 7’000 RPM.

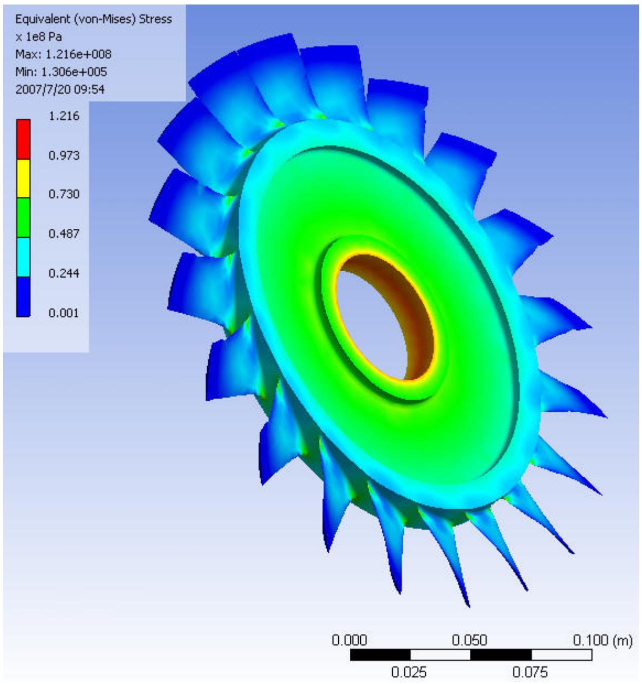

Fig. 4.26 Von Mises Stresses for the Scaled Blisk at a Rotational Speed of 25’000 RPM.

Fig. 4.27 and 4.28 show the calculated directional deformation in z-direction. Since this is a rotationally symmetric blisk, the deformations are symmetrical and also the deformations in y-direction are exactly the same. This is a verification for a correct boundary condition selection. The maximal deformation occurring in the blisk is 0.0759 mm respectively 0.0498 mm for the scaled down model. This makes 8.3 % respectively 14.7 % out of the designed tip clearance, which itself is 1% of blade span. It can be seen, that the deformations of the high altitude blisk are smaller than the ones of the scaled model. The reason for this is on the one hand the different environmental temperature and on the other hand the different rotational speed.

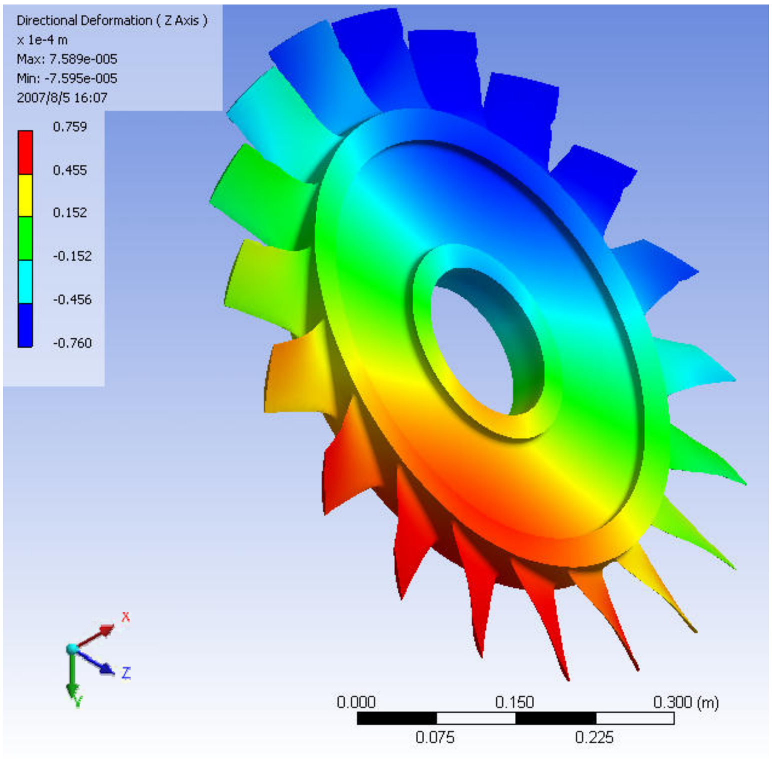

Fig. 4.27 Directional Deformation (Z Axis) for the High Altitude Blisk at a Rotational Speed of 7'000 RPM.

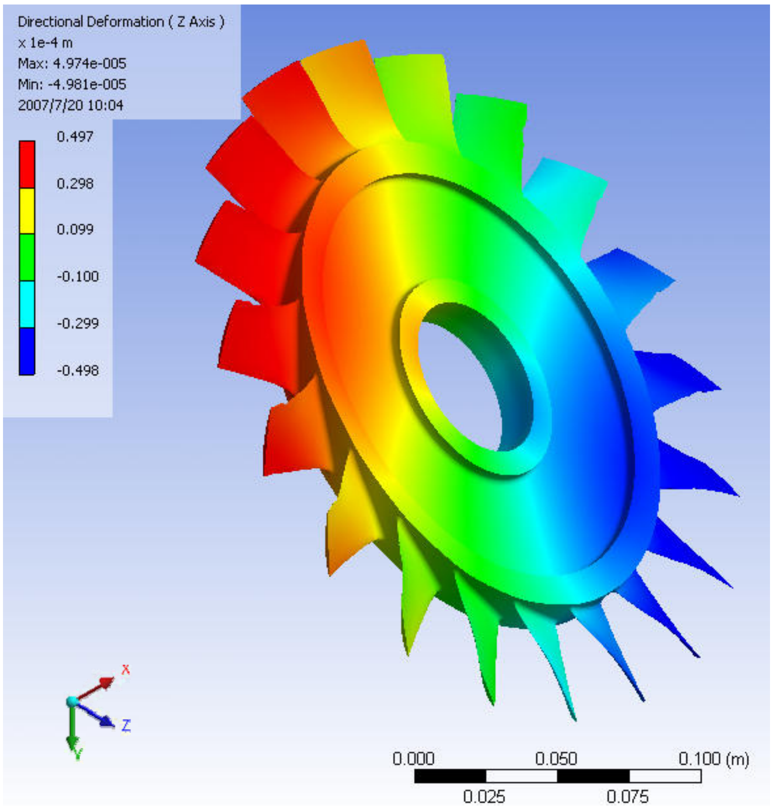

Fig. 4.28 Directional Deformation (Z Axis) for the Scaled Blisk at a rotational speed of 25'000 RPM.

Therefore, the results from the performed von Mises stress and the deformation calculations justify the rotor blisk design and the use in a real application without to have failure or a risk of casing rubbing.

4.5.2 Rotor Vibration Analysis

The rotor stress analysis showed a good mechanical performance. The next step is to perform a vibration analysis in order to make a statement about the system behaviour. In the following, an overview is given for the first six eigenfrequencies of the high altitude blisk and it's scaled down model.

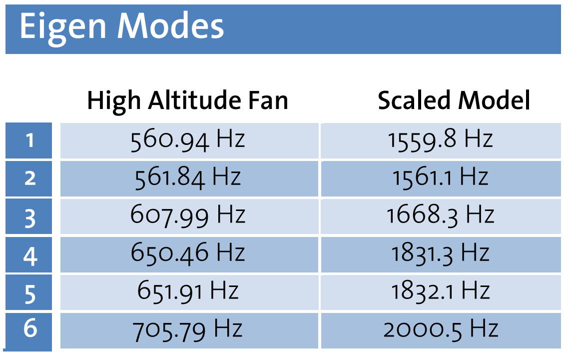

Eigen Modes

	High Altitude Fan	Scaled Model
1	560.94 Hz	1559.8 Hz
2	561.84 Hz	1561.1 Hz
3	607.99 Hz	1668.3 Hz
4	650.46 Hz	1831.3 Hz
5	651.91 Hz	1832.1 Hz
6	705.79 Hz	2000.5 Hz

Table 4.9 Eigen Modes of the Rotor Blades.

The maximal operating speed range is 116.7 Hz for the high altitude fan and 366.7 Hz for the scaled down model. Therefore, for both cases, the first six, and hence all further eigenfrequencies are located considerably above the maximal operating speed range and cannot be excited during operation.

The mode shapes belonging to these six eigenfrequencies for both geometries are depicted in Fig. 4.29 and 4.30.

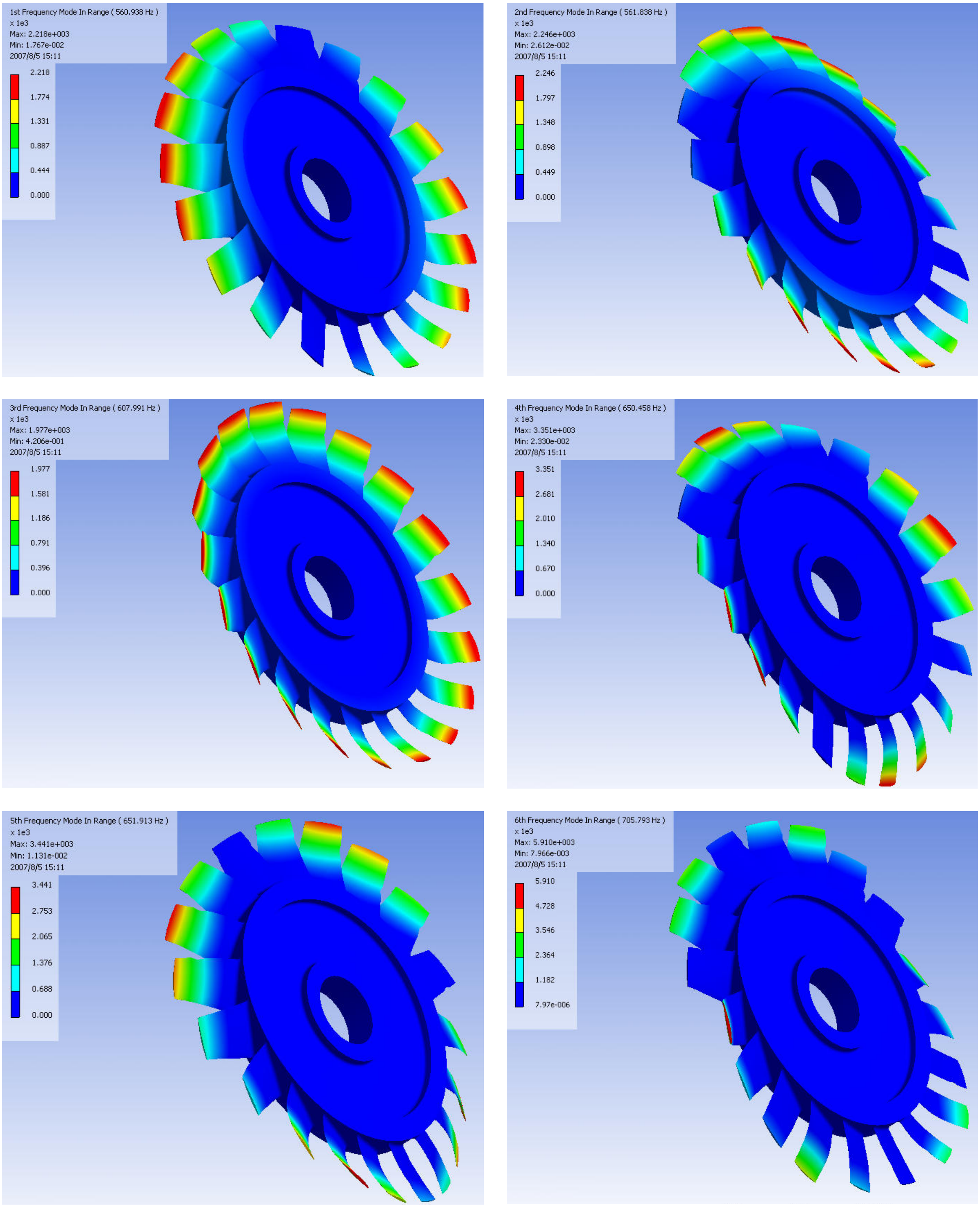

Fig. 4.29 Mode Shapes of the first six Eigenfrequencies of the High Altitude Blisk (7'000 RPM).

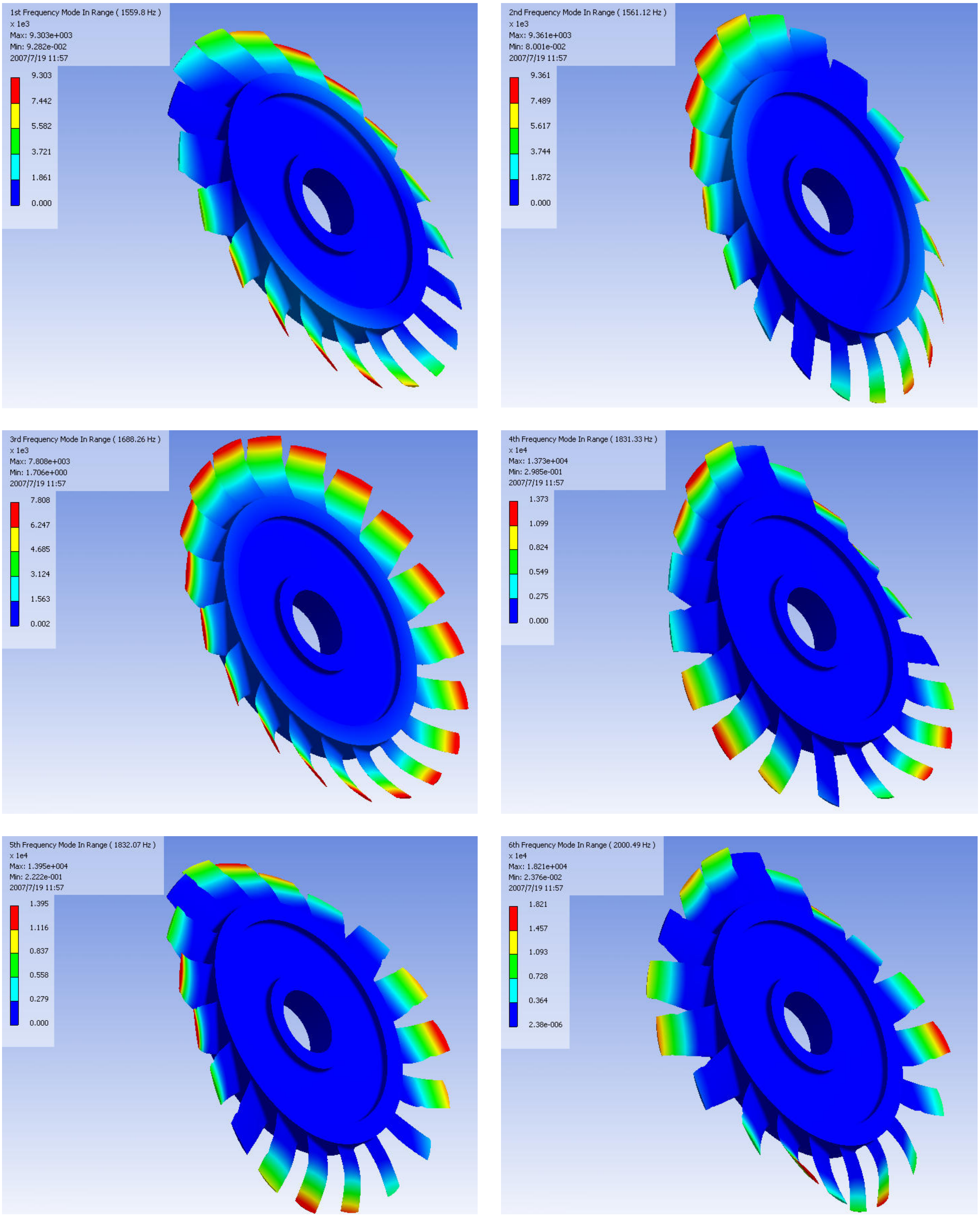

Fig. 4.30 Mode Shapes of the first six Eigenfrequencies of the Scaled Down Blisk (25'000 RPM).

4.6 Stator Design Optimization

While the rotor shows a satisfying performance, the preliminary stator design has to be optimized in order to avoid or at least to minimize the occurring hub and tip separation. As mentioned above, only the stator blade hub and tip profiles have to be turned more into the flow in order to decrease the incidence angle. Also the stagger angle is adapted in order to avoid a high turning of the flow. Inspired by the work of Thomas Behr, additionally a leaning and a sweeping is applied to the stator blade. This leads to a much more stable flow around the stator blade and helps to suppress the separation. The change in incidence and stagger angle, as well as the leaning and sweeping is done using in Axcad, the tool used in the 2-D design of the compressor. The incidence and stagger angle are only changed for the hub and tip airfoil section, while maintaining the rest of the defined sections along blade span.

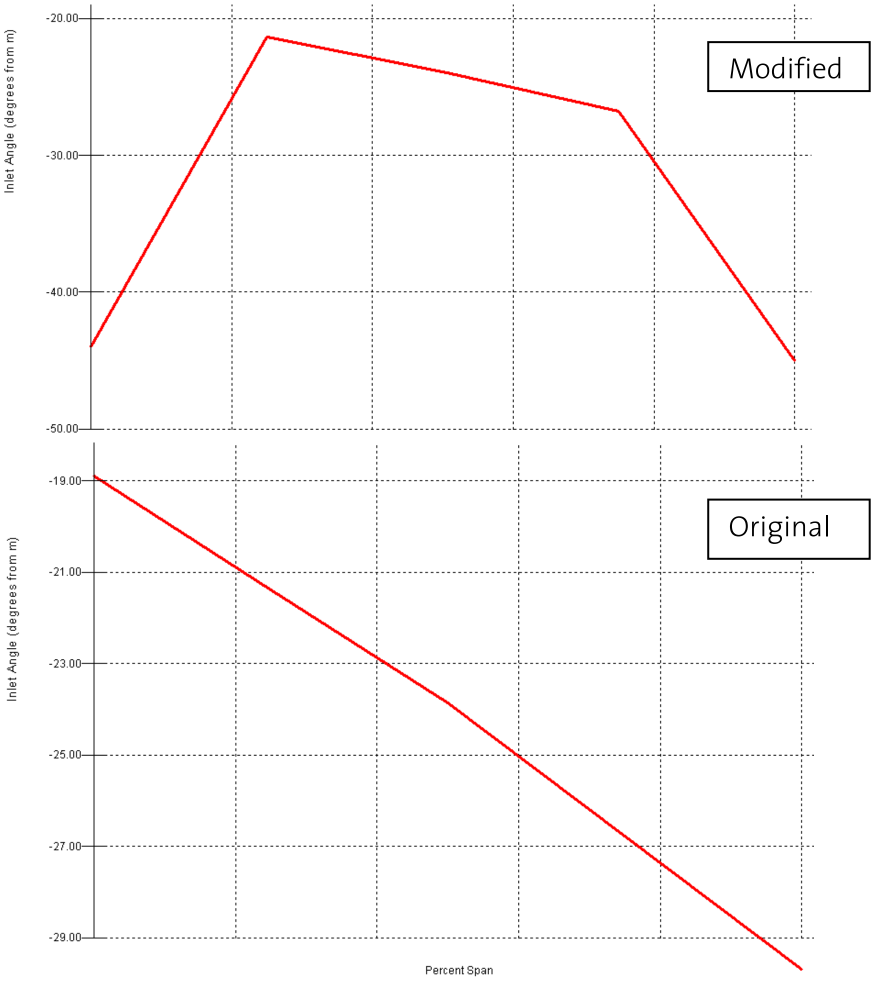

Fig. 4.31 Inlet Angles defined for five Cross-Sections across Span (0 %, 25 %, 50 %, 75 %, and 100 % of span). a) Optimized Stator vs. b) Preliminary Design.

Fig. 4.31 shows the defined stator blade inlet angle for defined five cross-sections (0 %, 25 %, 50 %, 75 %, and 100 % of span) for both design cases. In order to avoid a kink in the leading and trailing edge near hub and tip due to the change in incidence angles, the blade geometry is generated by interpolating between the defined cross-sections. The leaning and sweeping are applied by changing the meridional and tangential stacking curve. The values are changed from zero radial offset for both curves (original design) to values shown in Fig. 4.32 and 4.33.

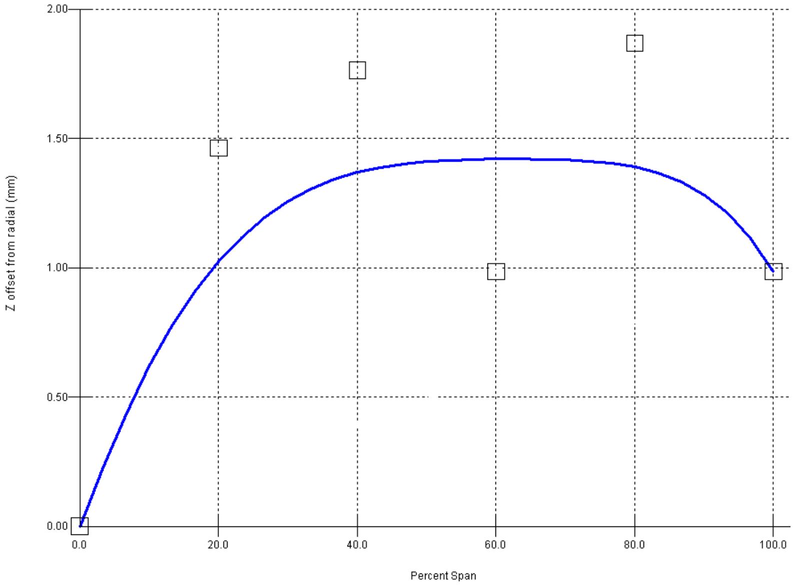

Fig. 4.32 Meridional Stacking Curve.

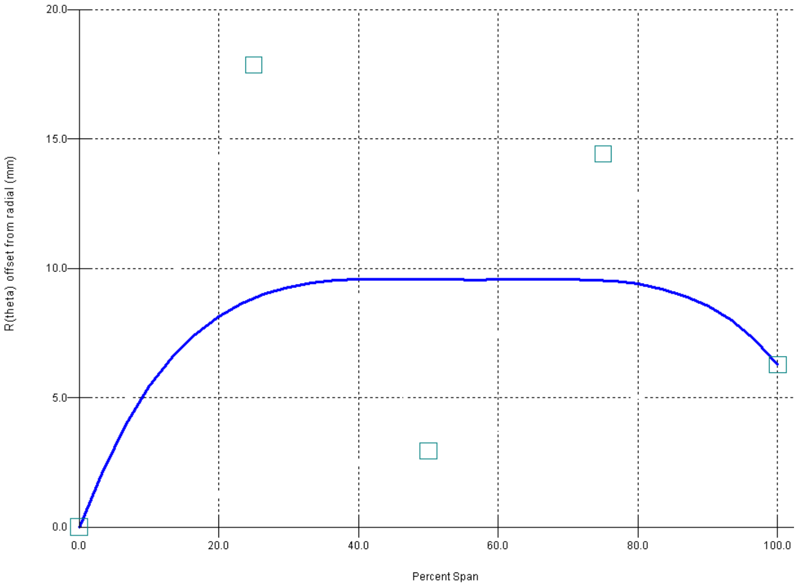

Fig. 4.33 Tangential Stacking Curve.

The change of the meridional and tangential stacking curve has a direct influence on the profile stacking. Fig 4.34 compares the profile stacking for the new and old design. Where the profiles for the original design are all stacked linearly above each other, they are relatively shifted for the new design, following the change in the stacking curves.

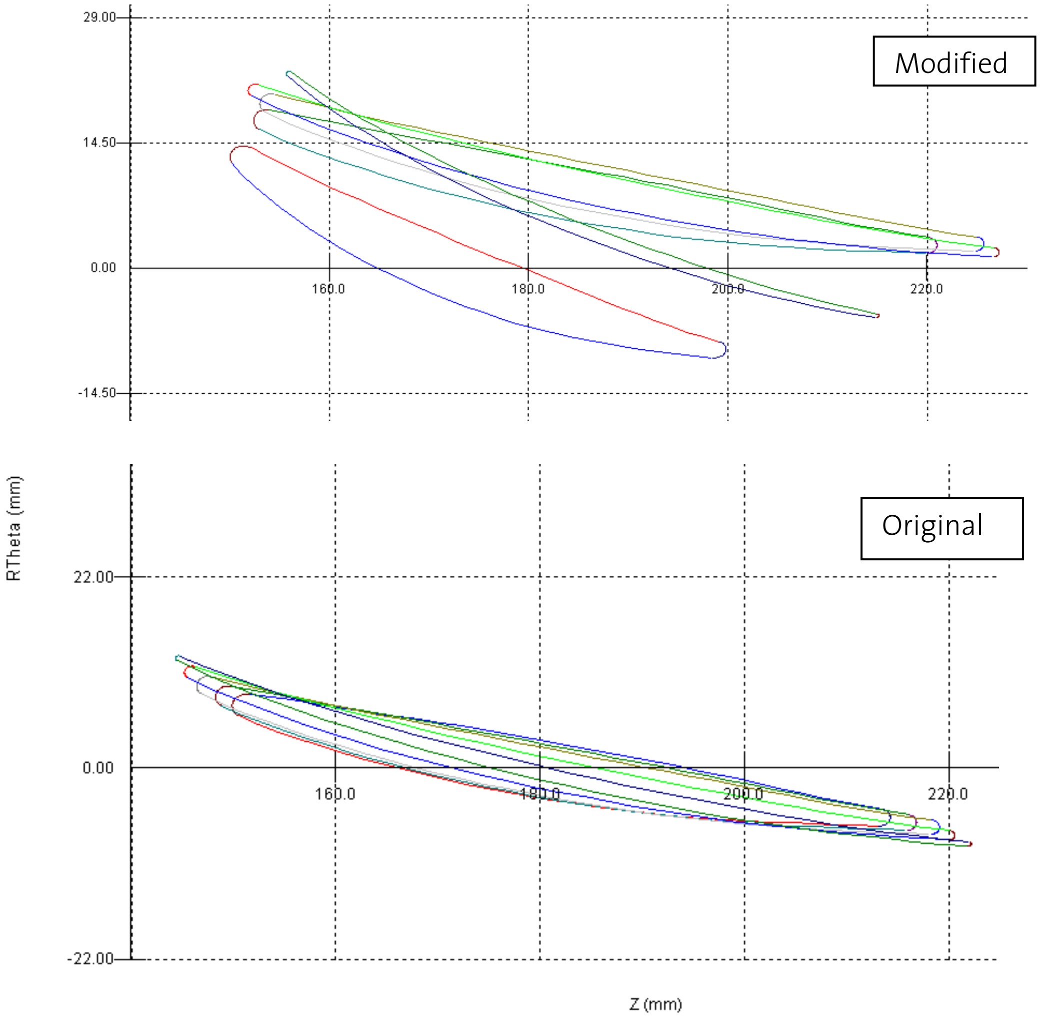

Fig. 4.34 Stator Blade Profile Stacking (Optimized vs. Original Design).

The optimized blade is presented in the following figures and compared to the preliminary design. Fig. 4.35 and 4.36 show the effect of leaning and sweeping as well as the inlet and stagger angle change on the stator blade.

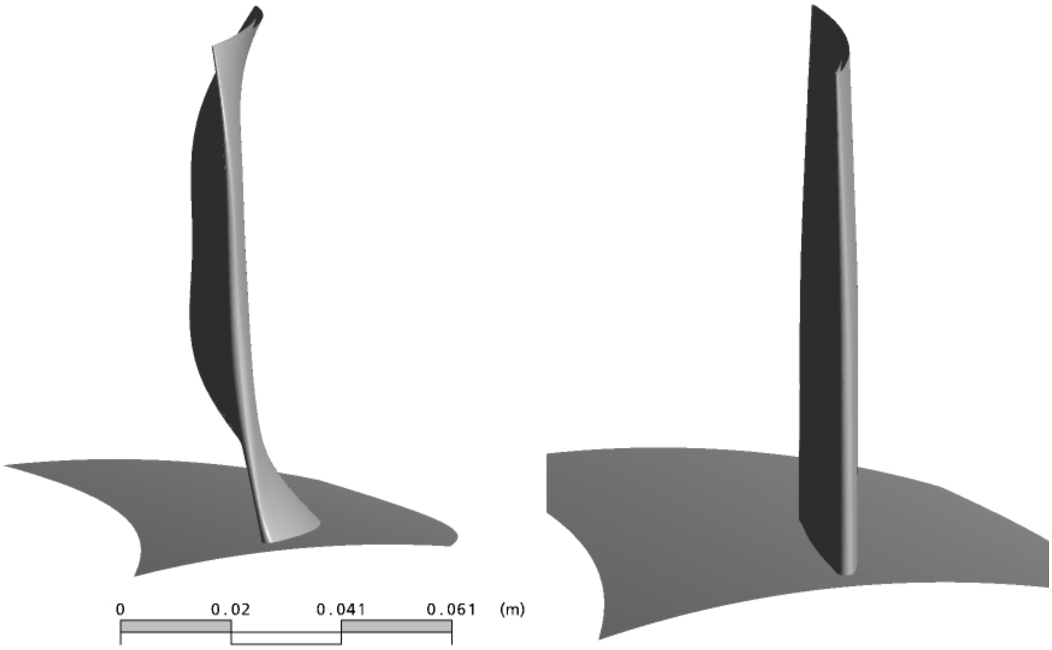

Fig. 4.35 Leaned Stator Blade vs. Preliminary Stator Blade.

Fig. 4.36 Swept Stator Blade vs. Preliminary Stator Blade.

Additionally to the modification on the stator blade, the vane count is changed. The number of stator vanes is increased from 14 to 21 blades. Finally, the optimized stage is presented in Fig. 4.37.

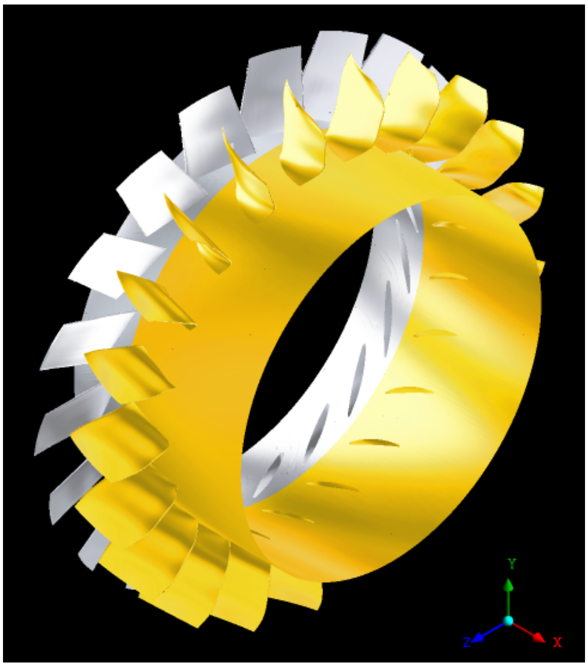

Fig. 4.37 Optimized Stage Design.

CFD is applied again to validate the optimized stator design against the preliminary design. All boundary conditions and solver settings remain the same. Only a new grid is generated for the new stator geometry as shown in Fig. 4.38. The CFD results are presented in the following section.

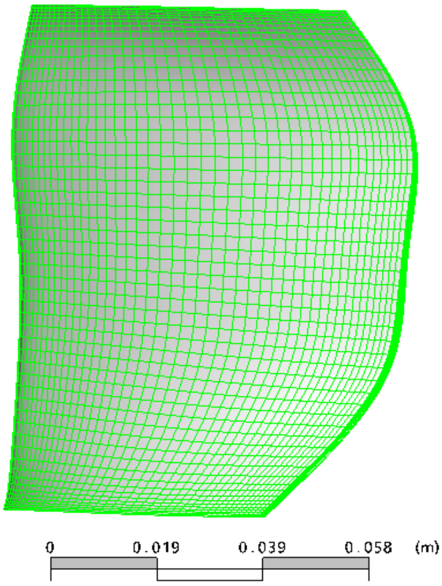

Fig. 4.38 Grid optimized stator.

4.7 Comparison

The stator blade is accurately designed with both leaning and sweeping in order to modify the separated flow at hub and tip. Flow streamlines are compared for the original and the modified design in the next two figures. The beneficial effect of change in incidence angle as well as stator blade leaning and sweeping on the hub corner separation is shown.

$pr = 1.05$
$\dot{m} = 0.597\ kg/s$
$N = 7000\ RPM$

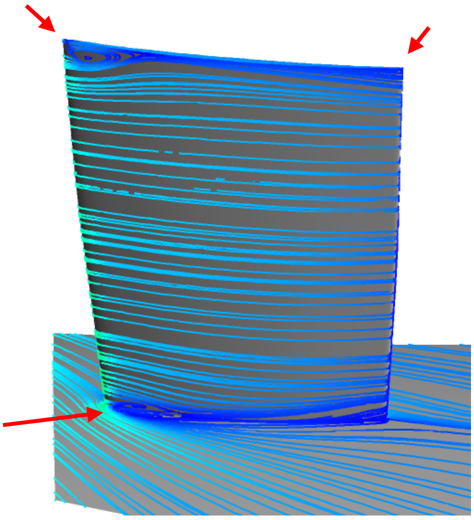

Fig. 4.39 Preliminary Stator Blade Design.

$pr = 1.05$
$\dot{m} = 0.599\ kg/s$
$N = 7000\ RPM$

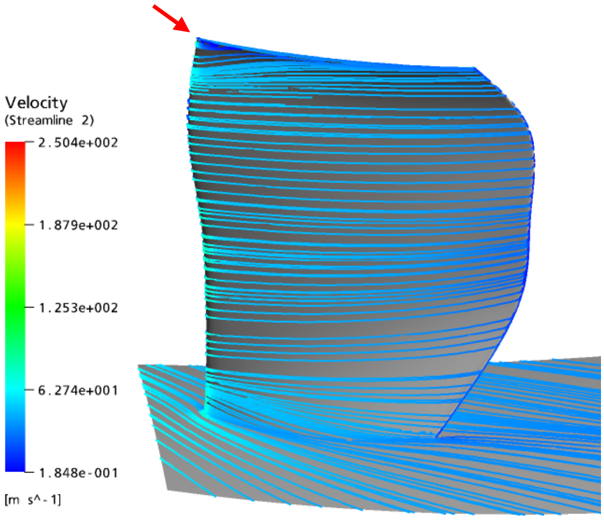

Fig. 4.40 Optimized Stator Blade Design.

In the following, the stator blade loading is compared at hub, midspan and tip. The rotor loading (Fig. 4.17) is found no to be affected by the stator design modification and is therefore not presented here again. It can be clearly seen, that the loading is reduced throughout the entire chord with the modified design, especially at hub, where the largest loading occurs. At lower blade loading the diffusion factor is reduced and therefore the losses.

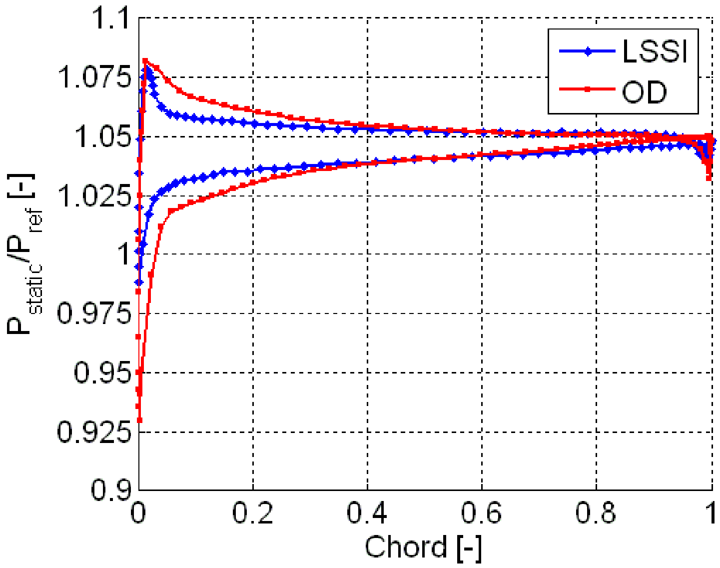

Fig. 4.41 Stator Blade Loading at Hub (Modified Design (LSSI) vs. Original Design (OD)).

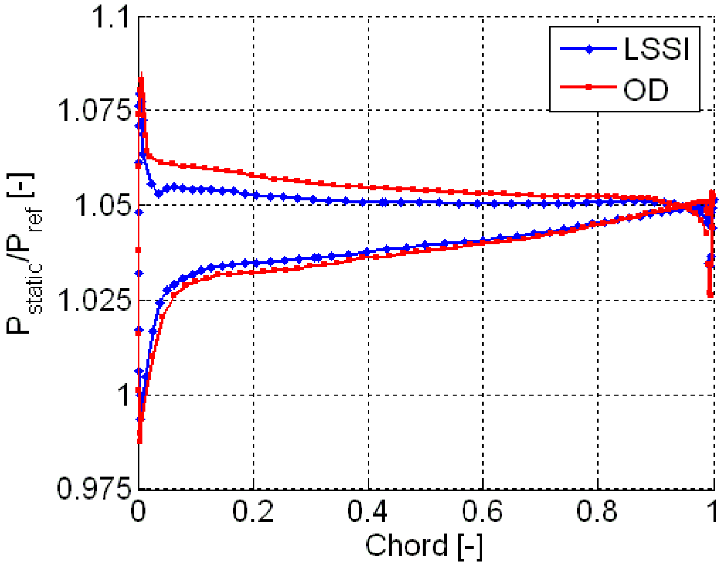

Fig. 4.42 Stator Blade Loading at Midspan (Modified Design (LSSI) vs. Original Design (OD)).

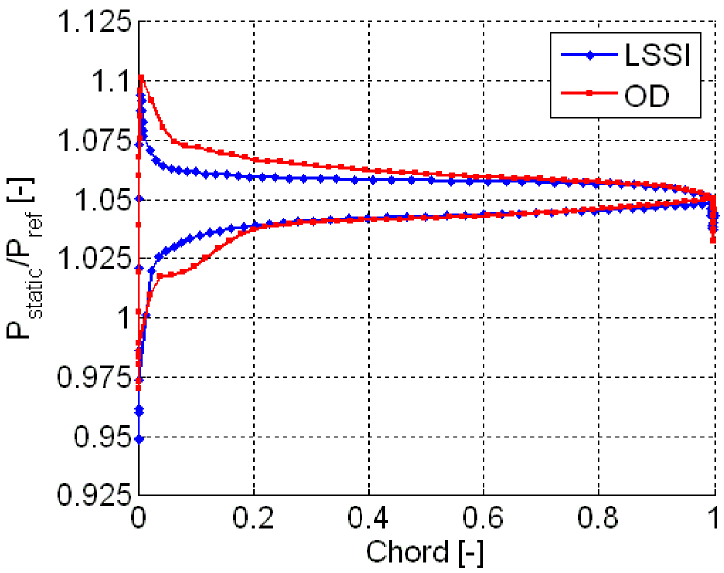

Fig. 4.43 Stator Blade Loading at Tip (Modified Design (LSSI) vs. Original Design (OD)).

The improvements can also be seen in the pressure and velocity distribution in the blade to blade view. The following figures show a comparison for hub, midspan and tip (Original design vs. Modified design). The comparison is done for an almost same operation point as indicated.

The pressure distribution and the flow field through the rotor are almost identical for the compared cases. The main differences are found as expected in the pressure distribution and flow field for the stator row. The modified incidence and stagger angle totally suppress the initial hub corner separation and greatly reduce the tip corner separation. The flow at midspan shows for both cases a good behaviour. The leaning and sweeping of the vane positively contribute to the reduction of separation as well as to the overall stabilization of the flow. It may be noticed that there is a difference in the blade passage between both designs. This is due to the increased stator vane count change, from 14 to 21 vanes.

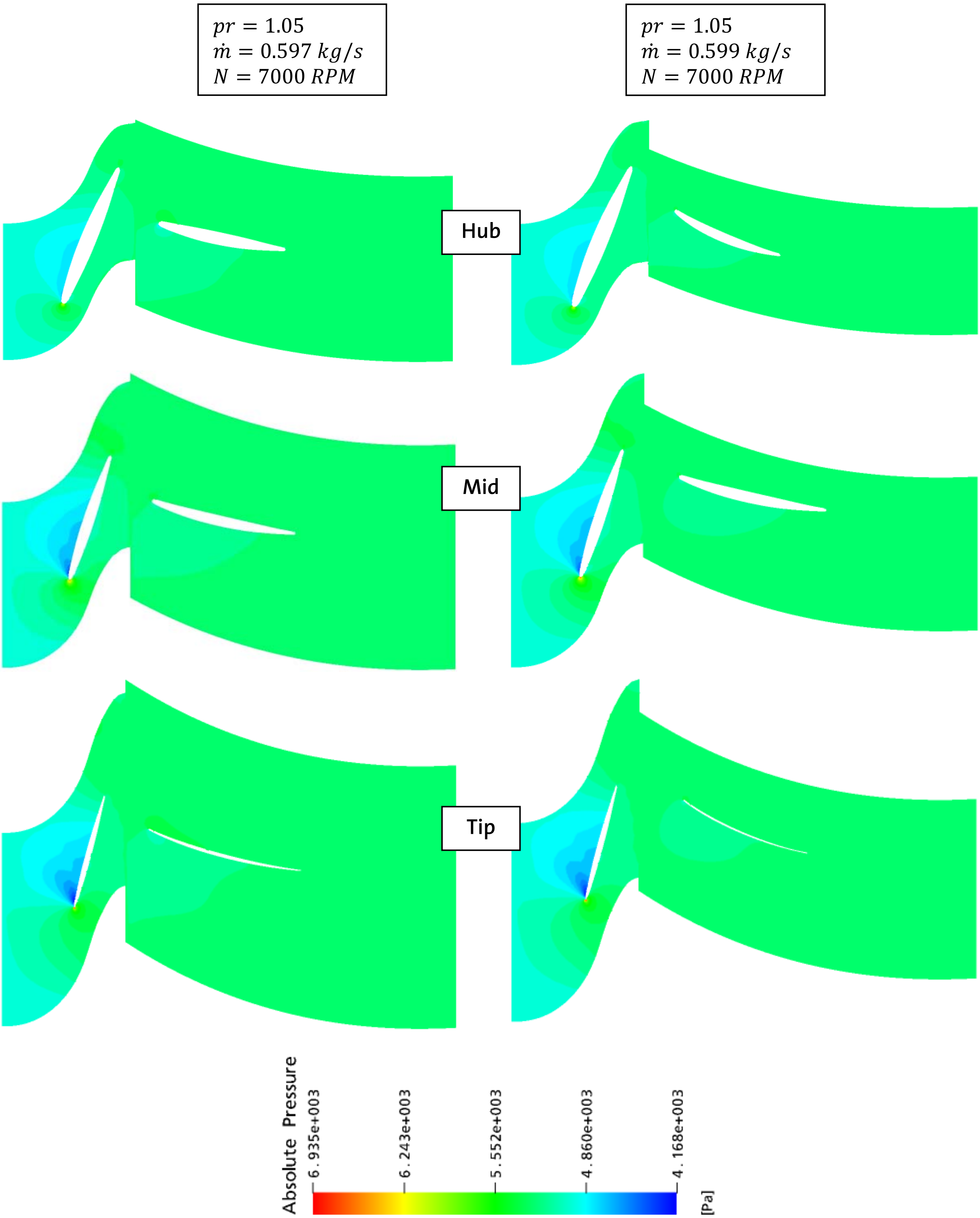

Fig. 4.44 Blade to Blade View: Absolute Pressure.

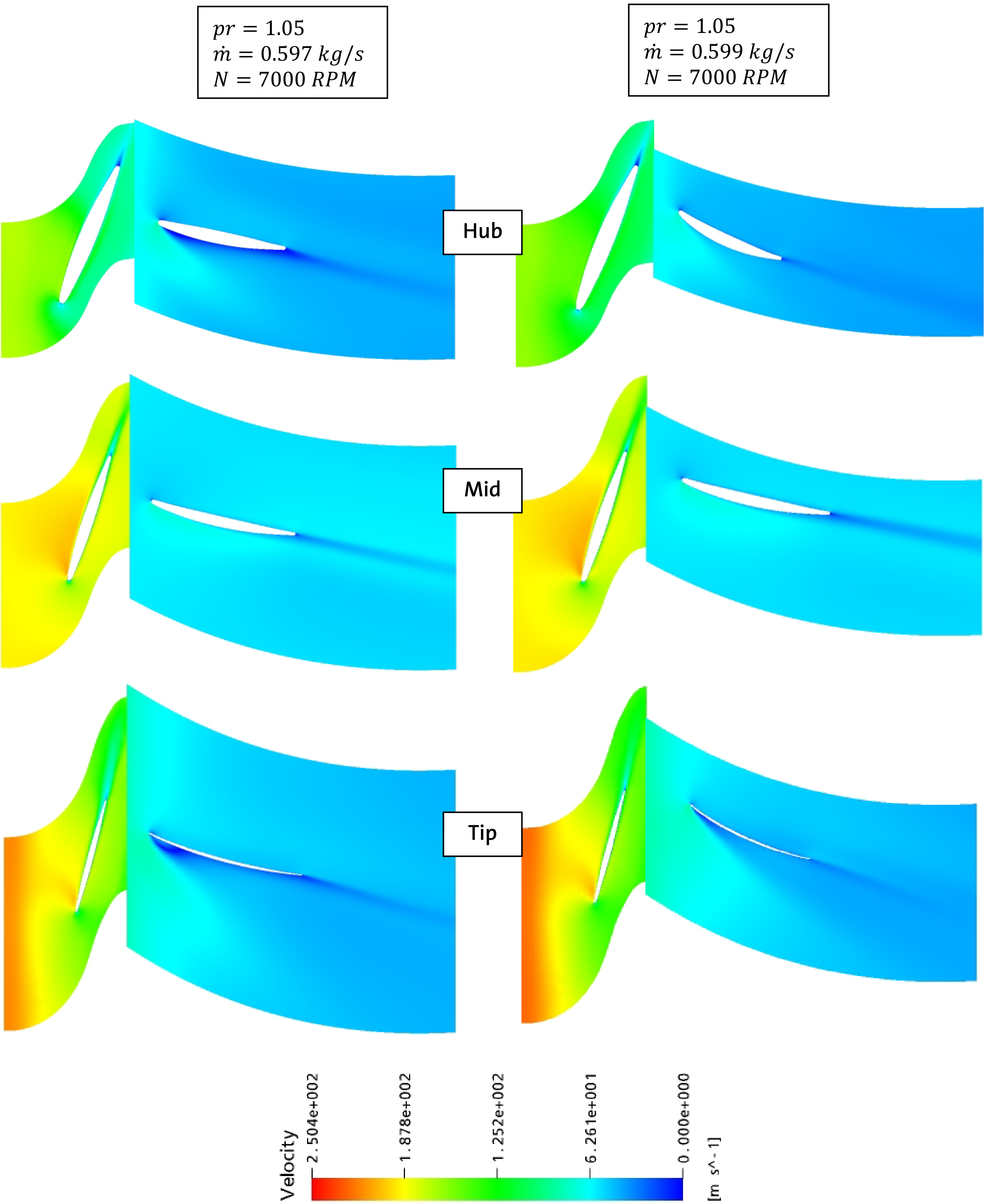

Fig. 4.45 Blade to Blade View: Velocity in Relative Frame.

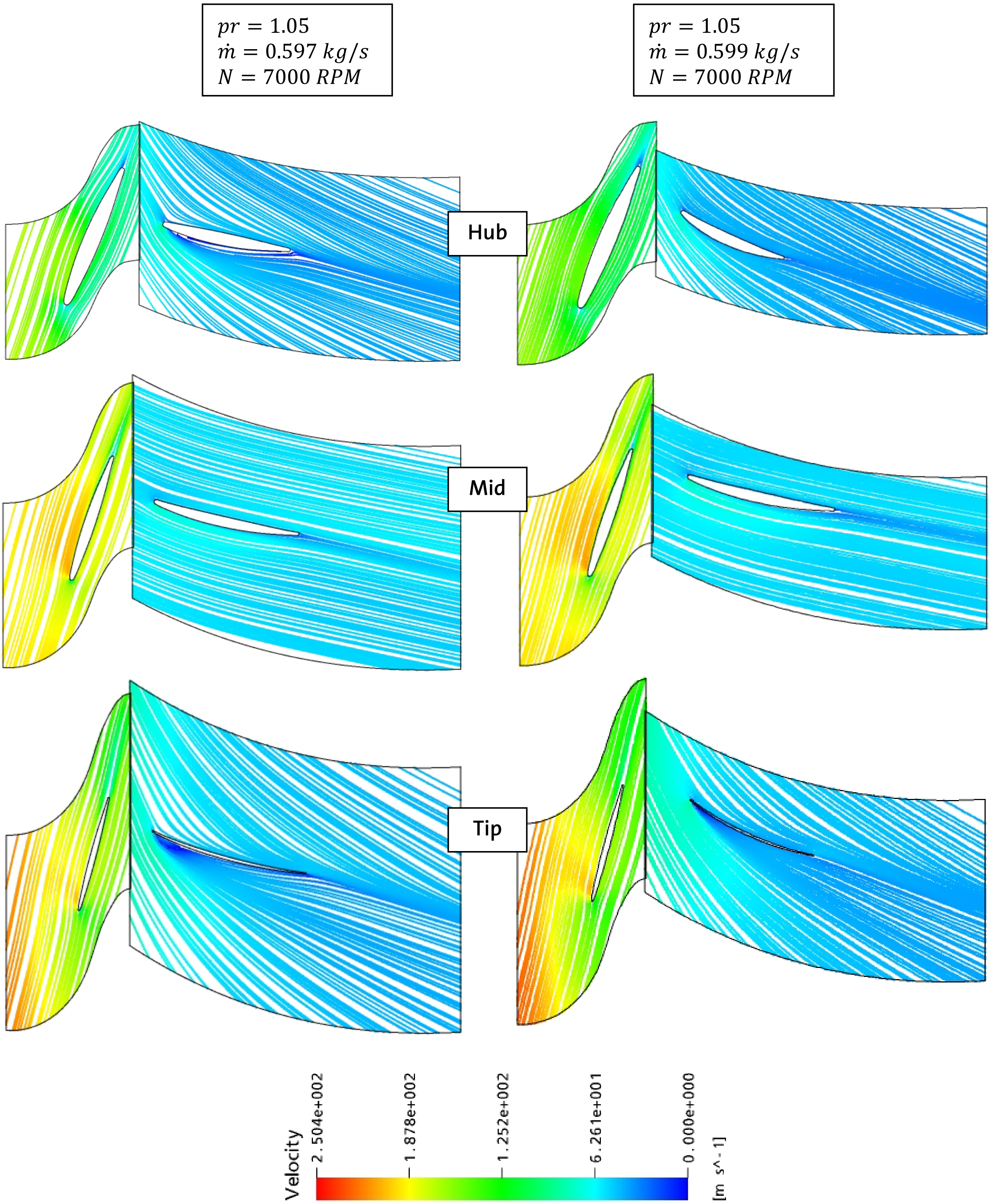

Fig. 4.46 Blade to Blade View: Velocity in Relative Frame (Streamlines).

Fig. 4.47 shows two speed lines as a comparison of the new design (LSSI) with the preliminary analysis results (OD). With the optimized stator row, the stall condition is shifted towards higher pressure ratio and lower mass flow rate. For the design speed of 7000 RPM, a pressure ratio up to 1.08 can be reached before the compressor stalls. Compared to the stall condition of the original design at around a pressure ratio of 1.06, this is an increase of 33 % or an additional increase of 100 Pa.

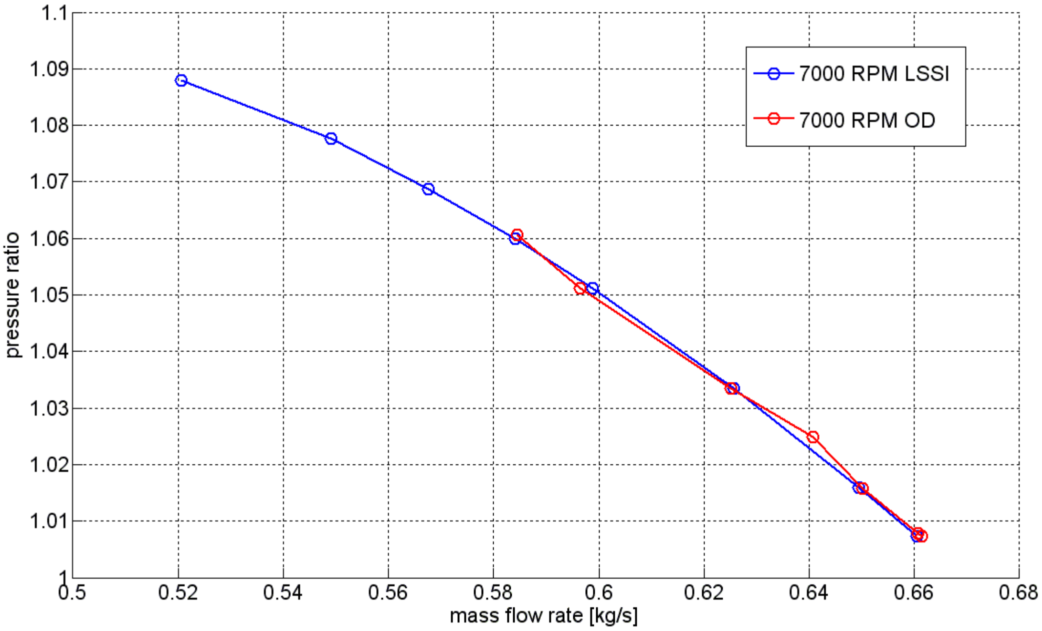

Fig. 4.47 Comparison of Design Speed Line for New Design (LSSI) vs. Original Design (OD).

The beneficial stator blade optimization in terms of flow separation and stability does also have an influence on the efficiency as shown in Fig. 4.48. The isentropic efficiency curve follows the same trend as shown above for the speed lines. It is extended towards smaller mass flow rates, i.e. towards higher pressure ratios. Therefore, highest efficiencies are reached for pressure ratios between 1.08 – 1.09, which are nevertheless very close to stall condition.

To study the compressor stability, the stall margin (SM) is defined as follows [B. H. Beheshti]:

$$SM = \left(\frac{\pi_{stall} \cdot \dot{m}_{design}}{\pi_{design} \cdot \dot{m}_{stall}} - 1\right) \cdot 100.$$

The stall pressure ratio (π_{stall}) and stall mass flow rate ($\dot{m}_{stall}$) are 1.06 and 0.583 kg/s³ for the original design and 1.0877 and 0.52 kg/s³ for the optimized design. The stall margin for a design pressure ratio of 1.05 and design mass flow rate of 0.6 kg/s³ is 3.9 % for the original design and 19.53 % for the optimized design. Hence, the stall margin is considerably improved by 15.63 %.

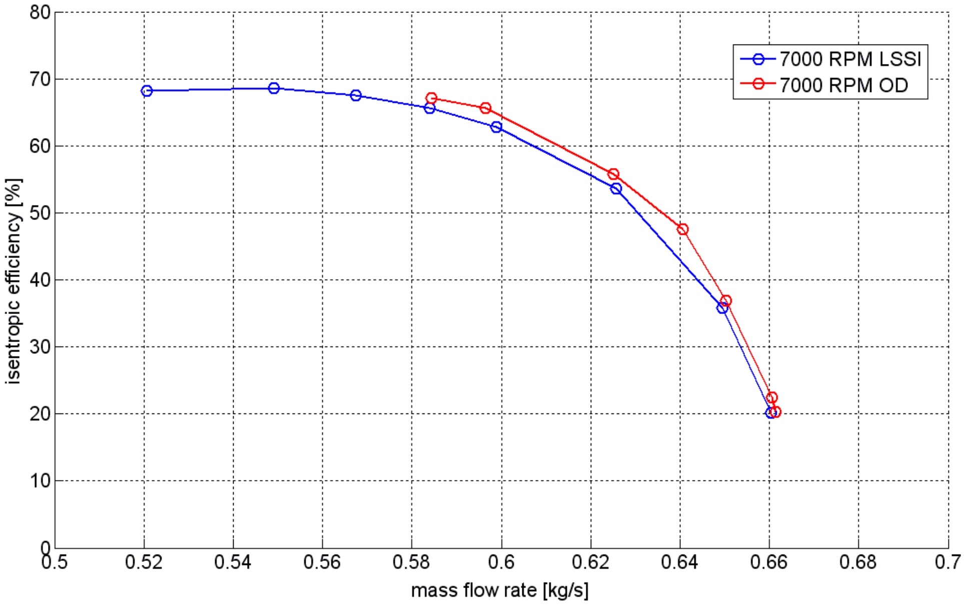

Fig. 4.48 Efficiency Plot: Comparison of New and Old Design.

Chapter 5

Experimental Setup

5.1 Introduction

The designed one stage axial compressor presented in the previous chapters showed a satisfying aerodynamic and mechanical behaviour according to numerical simulations. But this is not enough to guarantee appropriate working conditions in real situations. Therefore the compressor performance predicted by simulations must be validated by testing. Typically a scaled down model of the real compressor is built and tested. From scaling analysis (chapter 5.3) follows a reasonable scale factor of 3, considering manufacturability and rotational speed. While coming up with a test rig design, it has been noticed that an existing centrifugal compressor test rig at the Turbomachinery Laboratory of ETH Zurich offers a possibility to integrate an axial compressor in terms of model dimensions and rotational speed. This way, almost all measurement facilities needed are already available and can be directly used. A way to successfully integrate the fan into this test rig is found and discussed in the following chapters, after introducing the centrifugal compressor test rig *RIGI*.

5.2 The *RIGI* Test Rig at Turbomachinery Laboratory

5.2.1 Overview

The Turbomachinery Laboratory of ETH Zurich is equipped with a centrifugal compressor test rig named after a famous mountain near Luzern. In the past and today the test facility provides a solid basis to undertake research in the field of impeller aerodynamics, system instabilities, aerodynamic probe development FRAP and application of LDA measurement techniques. Currently the test facility is being redesigned aiming to extend its research capabilities into the field of forced response of radial compressors.

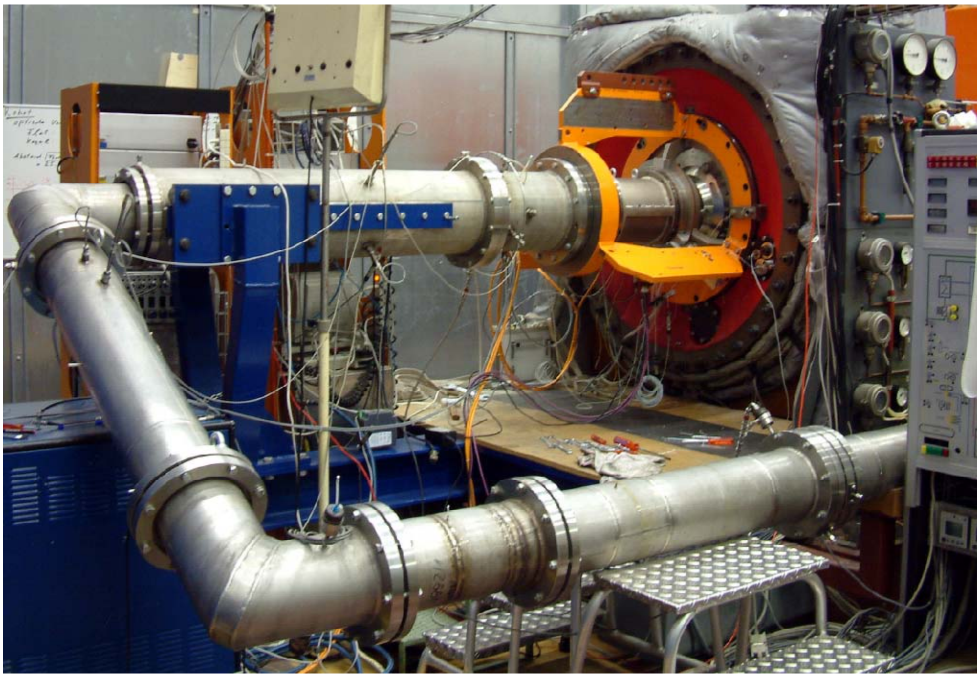

Fig. 5.1 RIGI Test Rig at Turbomachinery Laboratory ETH Zurich.

5.2.2 Test Rig Features

RIGI is a closed loop facility. Within the test section the pressure can be adjusted independent of the ambient conditions. During operation pressure and temperature at the inlet of the impeller are controlled and fixed. Herein the facility can be evacuated up to 0.25 bar absolute or pressurized to a maximum value of 4 bars. The maximum deliverable power to the rotating components is limited by a gearbox mechanism to 370kW and is supplied by an electrical DC motor. RIGI allows maximum rotational speeds up to 22'000 RPM. The mass flow is controlled through an orifice. Downstream of the impeller a water cooled heat exchanger reduces the fluid temperature to the required impeller inlet temperature.

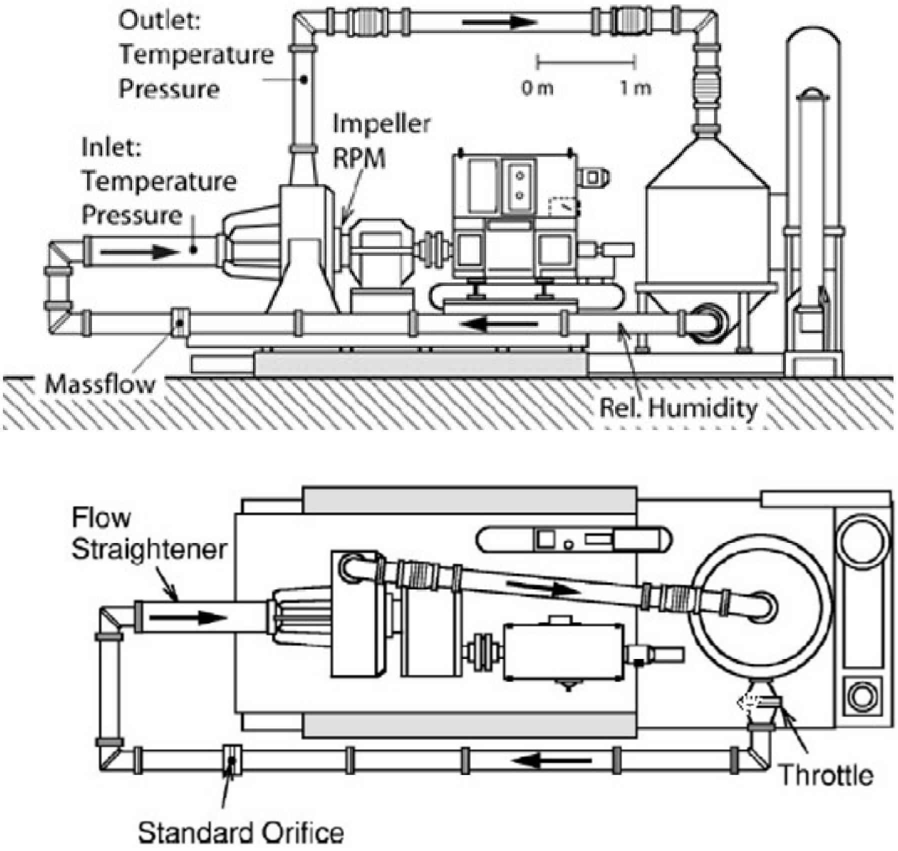

Fig. 5.2 Schematic of *RIGI* Test Rig Closed Loop.

A number of impeller configurations have been already tested in *RIGI* with typical outer diameters of 280 mm and pressure ratios around 2. In the latest research project prior to the current work an impeller was installed measuring 400 mm on the outer diameter generating a maximum pressure ratio in the excess of 3. The diffuser section allows modification of the diffuser configuration.

5.2.3 Measurement section

Fig. 5.3 shows the frame (orange) which carries a series of rings, beginning with the impeller shroud. This is the place where the impeller is located and therefore where most of the measurements are performed. Any technical or mechanical changes are done in this test section. In the following, this section is referred to as the measurement section.

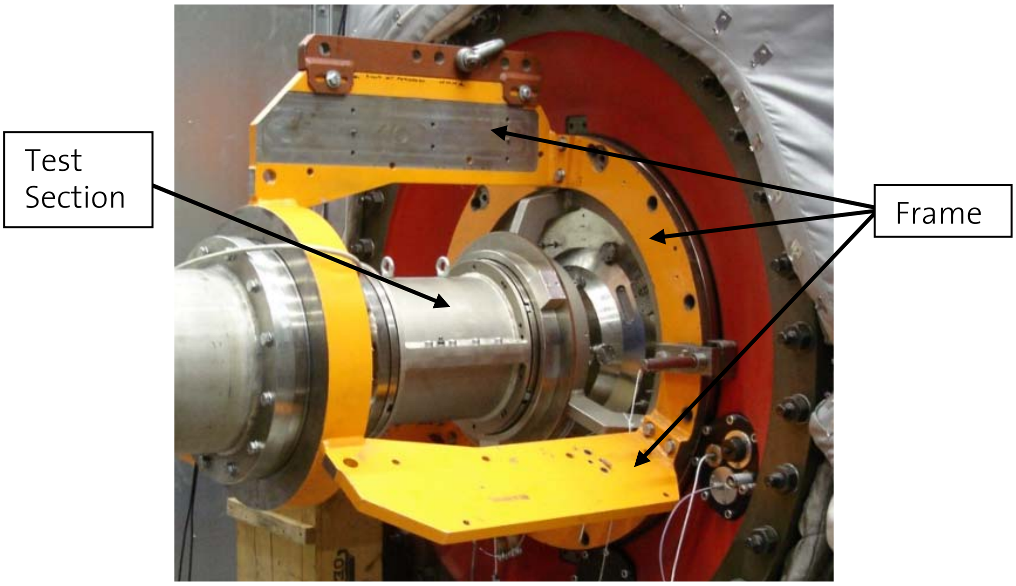

Fig. 5.3 Test Rig Measurement Section.

5.2.4 Measurement Techniques

During operation two separate acquisition systems record data from sensors installed in the facility. On the one hand performance data is acquired in order to monitor and to control the operating conditions of the facility and on the other hand data is acquired from a set of fast response measurement techniques i.e. pressure transducers, the fast aerodynamic probe FRAP or the LDA system.

In order to perform the impeller measurements, RIGI is currently being extended by a rotating transmission system. This will allow to perform strain gauge and pressure sensor measurements on the impeller surface.

5.3 Scaling of the Compressor

To keep the aerodynamic behaviour of the fan constant, we must ensure that the Mach Number in axial and circumferential direction remain constant.

$$Ma_x = const$$
$$Ma_U = const$$

As a result, the velocity triangles will also remain the same.

Three different aspects have to be considered while scaling the fan:

- The Reynolds number will change, since the dimensions of the blade and the environment is changed.
- The stresses will change, since the ring speed can not be kept constant. This is again a result of the environment change.
- The pressure ratio remains constant as a result from the mean line design.

First the Mach Number for the axial flow C_x is taken into account. (1 refers to the compressor inlet)

$$Ma_x = \frac{c_{x1}}{\sqrt{\gamma R T_1}} \qquad \text{(Eq. 5.1)}$$

$$C_x = \frac{\dot{m}}{\rho_1 A_1} \qquad \text{(Eq. 5.2)}$$

$$\rho_1 = \frac{p_1}{R T_1} \qquad \text{(Eq. 5.3)}$$

$$T_1 = T_{01}\left(1 + \frac{\gamma - 1}{2} Ma_x^2\right)^{-1} \qquad \text{(Eq. 5.4)}$$

A_1 is the through flow area of the compressor inlet. The equations above can be combined which lead to an expression for the axial Mach number.

$$Ma_x = \frac{\dot{m}\sqrt{RT_{01}}}{p_1 A_1 \sqrt{\gamma}}\left(1 + \frac{\gamma - 1}{2} Ma_x^2\right)^{-\frac{1}{2}} \qquad \text{(Eq. 5.5)}$$

To determine Ma_x, Eq. 5.5 has to be solved iteratively.

$$Ma_x = f(Ma_x)$$

$$Ma_x = \underbrace{\frac{\dot{m}\sqrt{RT_{01}}}{p_1 A_1 \sqrt{\gamma}}}_{\alpha}\left(1 + \underbrace{\frac{\gamma - 1}{2}}_{\beta} Ma_x^2\right)^{-\frac{1}{2}}$$

$$x = \alpha(1 + \beta x^2)^{-\frac{1}{2}} \qquad | \ \text{sub } Ma_x = x$$

Iteration loop:

1. initialize x_o
2. $x_{n+1} := f(x_n)$
3. check if $x_n - f(x_n)$ fulfils terminating condition
4. if not, redo all steps but initialize

Values used for iteration (design point data from original fan):

$$\dot{m} = 0.6\ \frac{kg}{s}$$
$$R = 287\ \frac{J}{kgK}$$
$$p_1 = 5000\ Pa$$
$$A_1 = 0.14813\ m^2$$
$$\gamma = 1.4$$
$$T_{01} = 216.69\ K$$

$$Ma_x = \frac{\dot{m}\sqrt{RT_{01}}}{p_1 A_1 \sqrt{\gamma}} \left(1 + \frac{\gamma - 1}{2} Ma_x^2\right)^{-\frac{1}{2}} \quad \rightarrow \quad Ma_x = 0.17025$$

The geometry of the scaled fan is already given by the fixed the test rig dimensions of *RIGI*. The compressor inlet conditions are as follows:

$$T_{01} = 300\ K$$
$$A_1 = 0.020686\ m^2$$
$$p_1 = 1\ atm$$

By reforming Eq. 5.5 and including these conditions, the necessary mass flow is calculated:

$$\dot{m} = \frac{Ma_x \sqrt{\gamma} p_1 A_1}{\sqrt{RT_{01}}} \left(1 + \frac{\gamma - 1}{2} Ma_x^2\right)^{\frac{1}{2}} \qquad \text{(Eq. 5.6)}$$

Now the Mach Number based on the rotational velocity *Ma_U* has to be calculated. Knowing the mean radius r_m of the compressor, Ma_U is gives the angular velocity of the scaled-down fan.

$$Ma_U = \frac{U}{\sqrt{\gamma R T_1}} \qquad \text{(Eq. 5.7)}$$

$$U = \omega r_m = 2\pi f r_m = 2\pi \frac{N}{60} r_m \qquad \text{(Eq. 5.8)}$$

$$Ma_U = \frac{2\pi \frac{N}{60} r_m}{\sqrt{\gamma R T_1}} = \frac{2\pi N r_m \left(1 + \frac{\gamma - 1}{2} Ma_U^2\right)^{\frac{1}{2}}}{60\sqrt{\gamma R T_{01}}} \qquad \text{(Eq. 5.9)}$$

To determine Ma_U, Eq. 5.9 is iteratively solved following the same followed procedure as above for Ma_x:

$$Ma_U = 0.67068$$

The rotational speed N is computed by reforming Eq. 5.9 and inserting the inlet conditions for the scaled-down fan:

$$N = \frac{60\sqrt{\gamma R T_{01}}}{2\pi r_m \left(1 + \frac{\gamma - 1}{2} Ma_U^2\right)^{\frac{1}{2}}} \qquad \text{(Eq. 5.10)}$$

As previously mentioned, the test rig dimensions determine the scaled-down model size.

For a high altitude fan:

$$r_{Tip} = 299.9\, mm$$

$$r_{Hub} = 207.5\, mm$$

$$r_{ht} = \frac{r_{Hub}}{r_{Tip}} = 0.691$$

For a scaled model:

$$r_{Tip_m} = r_{Pipe} = 112\, mm$$

Initial scale factor:

$$z_i = \frac{r_{Tip}}{r_{Tip_m}} = 2.6776$$

$$r_{Hub_m} = \frac{r_{Hub}}{z_i} = 77.4924\, mm$$

The tip clearance is typically 1% of blade span:

$$1\%\ of\ blade\ span = t_c = r_{Tip_m} - r_{Hub_m} = 0.345076\, mm$$

The new tip radius for the model is computed:

$$r_{Tip_m} = r_{Pipe} - t_c = 111.654924\, mm$$

And finally the scale factor is obtained:

$$z = \frac{r_{Tip}}{r_{Tip_m}} = 2.68595$$

The following table summarizes the design parameters for the high altitude fan and its scaled-down model. These values are the result of the followed mean line design.

D_o [m]	D_i [m]	RPM	Re	Mass Flow [kg/s]	C_x [m/s]	U [m/s]	V [m/s]	Pshaft [W]
0.6	0.414	7000	77642	0.6	50.09	185.83	192.46	2628.2

Table 5.1 Design Parameters for High Altitude Fan .

Different scaled-down models are compared in the next table to illustrate the effect of the scaling factor *z* on the different design parameters. While with increasing scaling factor, the model size, mass flow, Reynolds Number and power decrease, the rotational speed is increasing. Although a small model size seems to be beneficial, but problems will be faced during manufacturing and the compressor has to be run at high rotational speed.

Scale	D_o [m]	D_i [m]	RPM	Re	Mass Flow [kg/s]	C_x [m/s]	U [m/s]	V [m/s]	P_{shaft} [W]
1	0.6	0.4	8141.9	1E+06	10.3	58.3	216.1	223.9	61138
2	0.3	0.21	16284	5.2E+05	2.6	58.3	216.1	223.9	15284
2.68	0.2	0.15	21788	3.9E+05	1.4	58.3	216.1	223.9	8537.6
3	0.2	0.14	24426	3.5E+05	1.1	58.3	216.1	223.9	6793.1
4	0.15	0.1	32567	2.6E+05	0.6	58.3	216.1	223.9	3821.1
5	0.12	0.08	40709	2.1E+05	0.4	58.3	216.1	223.9	2445.5

Table 5.2 Design Parameters for Scaled Models as a Function of z.

Reynolds Number

All efforts to keep the Reynolds Number constant failed. This is due to the strong change in density. The velocity triangle for the high altitude fan is defined by the flow angles and the velocities. In order to use the same geometry for the scaled model, the velocities are matched, while the flow angles are kept constant. The resulting velocity triangle is then similar to the original one.

It emanates from the following calculation that it is not possible to scale the velocity triangle while keeping both flow angles and Reynolds Number constant at the same time.

The Reynolds Number relative to the blade is defined in Eq. 5.11, where V represents the velocity relative to the blade and c represents the chord of the blade.

$$Re = \frac{V \cdot c}{\upsilon} \tag{Eq. 5.11}$$

Setting the Reynolds Number of the high altitude fan (Indices 1) and the scaled-down model (reference 2) give:

$$Re = \frac{V_1 \cdot c_1}{\upsilon_1} = \frac{V_2 \cdot c_2}{\upsilon_2}$$

From scaling:

$$c_1 = z \cdot c_2 \tag{Eq. 5.12}$$

$$V_2 = z \cdot V_1 \frac{\upsilon_2}{\upsilon_1}$$

Using the iterative solution for the axial Mach Number:

$$\dot{m}_2 = \frac{Ma_x \sqrt{\gamma} p_2 A_2}{\sqrt{RT_{02}}} \left(1 + \frac{\gamma - 1}{2} Ma_x^2\right)^{\frac{1}{2}}$$

$$C_{x_2} = \frac{\dot{m}_2}{\rho_2 A_2} \tag{Eq. 5.13}$$

$$U_2 = \sqrt{V_2^2 - C_{x_2}^2} \rightsquigarrow U_2 \in \mathbb{C} \tag{Eq. 5.14}$$

This will provide a non-real value for the circumferential velocity.

5.4 Axial Compressor Configuration

5.4.1 Axial Compressor Design and Integration

As discussed in the introduction, this chapter presents the axial compressor design and the integration into the test rig *RIGI*. Fig. 5.4 depicts the measurement section for an impeller configuration. As can be seen, it consists of a series of rings and an impeller shroud. The impeller is sitting on a short shaft. The idea is to integrate the one stage axial compressor into the straight constant diameter ring series of this measurement section. This automatically involves a shaft elongation.

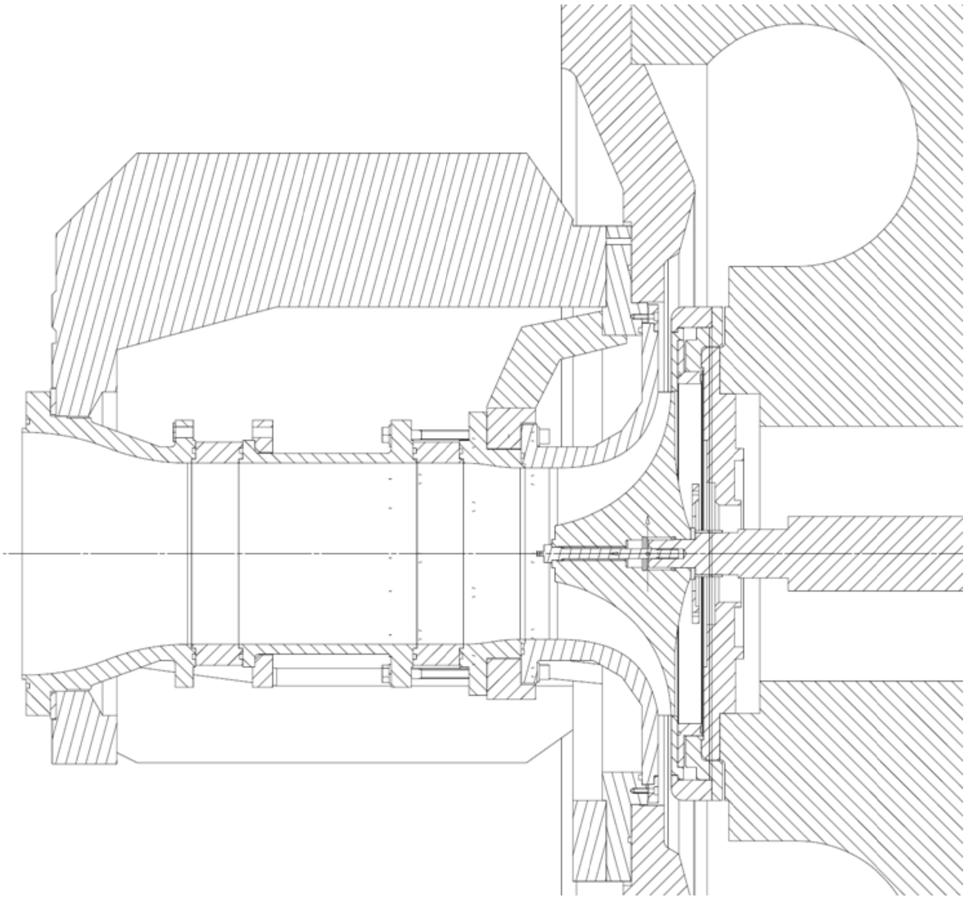

Fig. 5.4 Measurement Section for an Impeller Configuration.

The integrated axial compressor is presented in an enlarged assembly drawing on the next page (Fig. 5.5). The impeller and one of the rings have been removed, in order to allow an integration of a stator blisk assembly to support the extended shaft. The axial compressor configuration consists of more than 20 designed parts. Only the coupling and the bearings were ordered as off-the-shelf parts, all other parts were machined either in the workshop of the Turbomachinery Laboratory or externally (Table 5.3). Having the parts manufactured in-house turned out to be a big advantage. Customized solutions were developed and manufacturability problems are detected early and fixed immediately.

List of Parts

Table 5.3 introduces the most important parts of the axial compressor assembly and indicates where the parts have been manufactured or ordered. All these parts are numbered and shown in the enlarged assembly drawing in Fig. 5.5.

	Part	Comments
1	Cone	MSW
2	Cone Inserts	Rapid Prototyping *(Institute of Robotics)*
3	O-Ring Cone	Johansson
4	Rotor Blisk	Von Allmen
5	Stator Blisk	Rapid Prototyping *(Institute of Robotics)*
6	Stator Blisk Inner Ring	LSM Workshop
7	Stator Blisk Outer Ring	LSM Workshop
8	Struts with O-Ring	LSM Workshop
9	Shaft	LSM Workshop / Grünenwald
10	Rotor Axial Fixing	LSM Workshop
11	Rotor Axial Fixing M8 Nut (left-hand)	LSM Workshop
12	Bearings	SKF
13	Bearing Fixation Flange	LSM Workshop
14	Bearing Fixation Bush	LSM Workshop
15	Bearing Fixation Nut (left-hand)	Bossard
16	Flexible Coupling	Trelco AG
17	*RIGI* Shaft Attachment	LSM Workshop / Hönggerberg
18	*RIGI* Shaft	Already existing
19	Feather Keys	Bossard
20	Hub	LSM Workshop
21	Pressure Measurement Inserts	LSM Workshop

Table 5.3 Axial Compressor Configuration Part List.

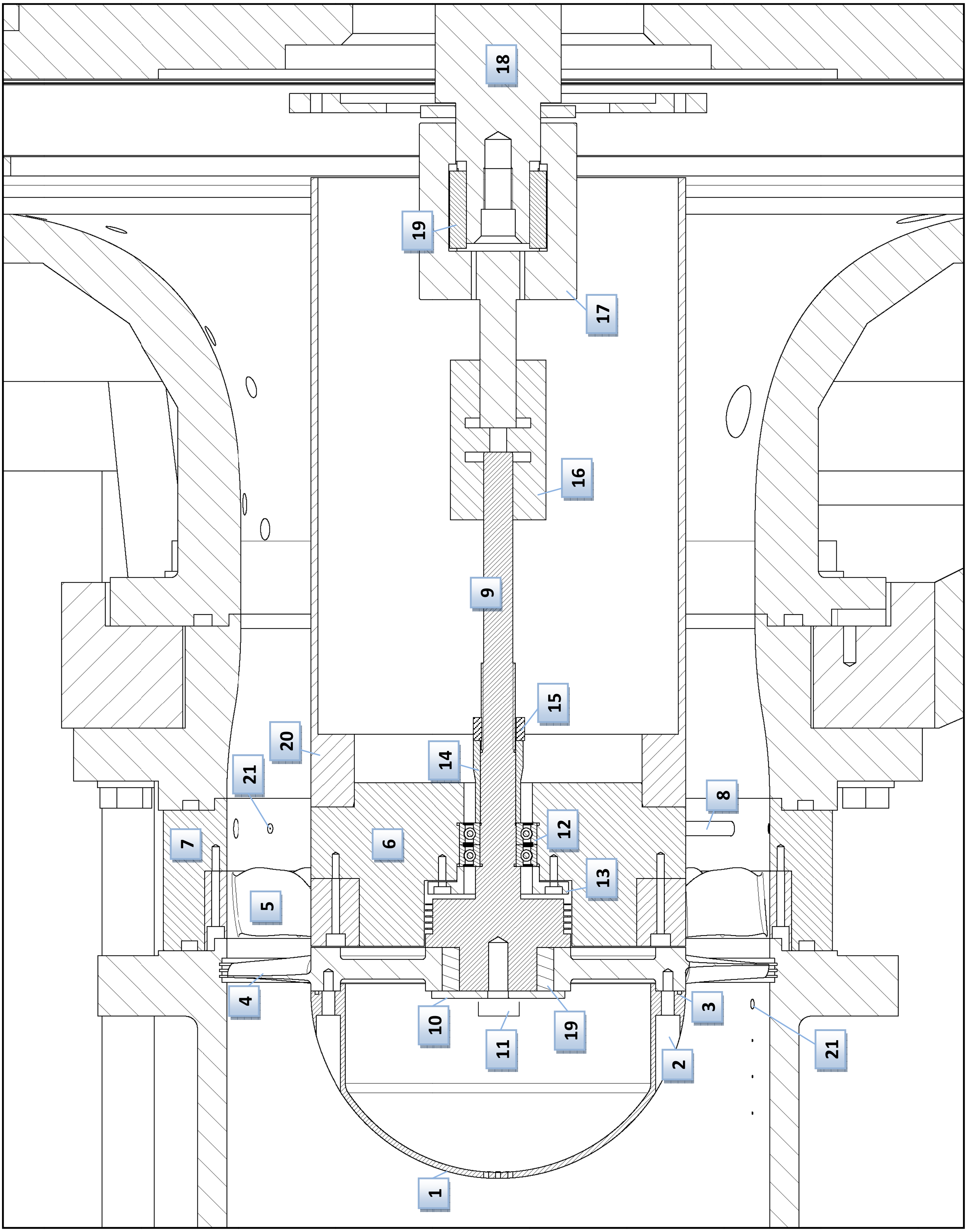

Fig. 5.5 Assembly Drawing.

5.4.2 Rotor Blade Manufacturing

The blade manufacturing is a key point in the compressor design. The accuracy of the blade profile and the throat area must be kept within tight tolerances. The combination of very thin compressor blades and the necessity of an accurate geometry for later comparison of the obtained measurement results with extensive CFD computations make the blade manufacturing a real challenge.

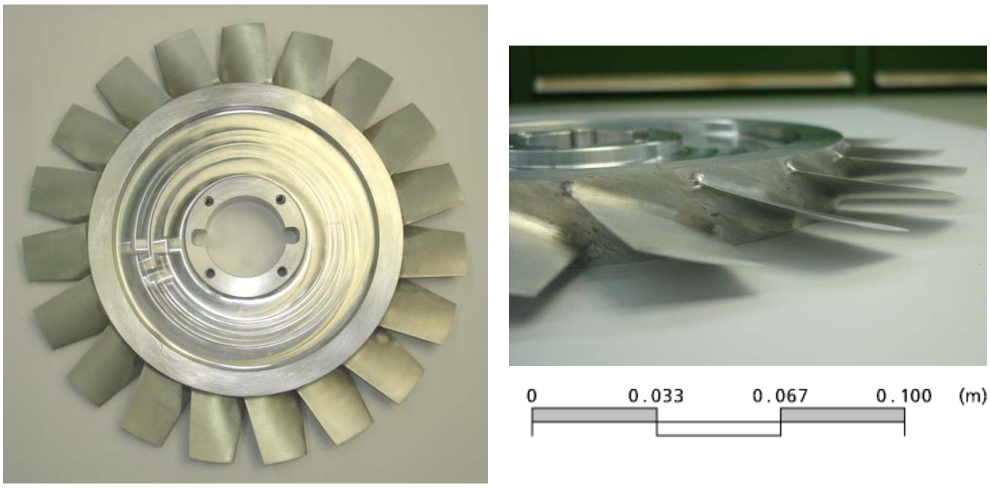

Fig. 5.6 Rotor Blisk with machined Force-Off Threads.

The compressor blades are manufactured out of high strength aluminium using milling. The so called blisk, which is a synonym for a bladed disk, turned out to be very accurate, especially in terms of balance, although some slight differences in thickness and length is observed at blade tip. The manufacturing time for such a blisk is seven weeks including delivery. The handling of such a blisk is obviously very practical with respect to the assembly process, as it simply has to be just shrunk on the shaft. Fig. 5.6 shows the manufactured rotor blisk. It can be seen how thin the aerofoils are, especially at the trailing edge. The aerofoils are almost as sharp as a knife. The maximal thickness at tip is 1.2 mm.

The fir tree shaped blade foot, normally used for a single blade design, is not considered in this design. This avoids the mounting of single aerofoils within a rotor ring as the related non-linear contact forces between the blade foot and the blade carrying ring. The blade manufacturing becomes much simpler, since the complex geometric interface between the blade foot and the rotor ring is avoided.

The high strength aluminium with a yield strength of $\sigma=4.2\cdot10^8$ N/m^2 is as stiff as standard steel, but at a lower density. The reduction of weight of the rotor disk positively affects the overhang of the disk relatively to the two bearings and therefore minimizes the gyroscopic effects. The blisk weight is a key issue in the design, driven by the high altitude application of the scaled up version of the blisk. This explains the choice of aluminium as the blades material instead of a Chrome-Nickel alloy. Additionally, the milling process is three times faster than the equivalent process for steel, which reduces the manufacturing cost by a factor 2 to 3.

The shrink fit design and calculation are presented in chapter 5.4.5. Two grooves for the feather keys are machined through the blisk to build a shaft hub joint. Once shrunk, the blisk cannot be easily pulled off. Also heating up the blisk does not help, since the shaft also will also get warm and expands. Therefore, four M4 force off threads are drilled into the blisk for carefully controlled strip off of the blisk, without harming the two contact surfaces.

5.4.3 Stator Blade Manufacturing

The design of the stator (casing and blades) considers removable stator blisk and probe accessibility to the area behind the stator blade row.

Initially, the stator blisk was designed so that it can also replace one of the already existing rings of the test rig, consisting of blades, inner and outer casing. This blisk would support the shaft by bearings and perfectly align it relatively to the rings, since the rings are assembled together by fitting into each other.
With this design, the blisk would perfectly align and carry the load of the rotating shaft, avoiding any weight carrying struts and any exhausting alignment effort. The ideal ring to replace is the one marked in Fig. 5.7, which shows the configuration for an impeller.

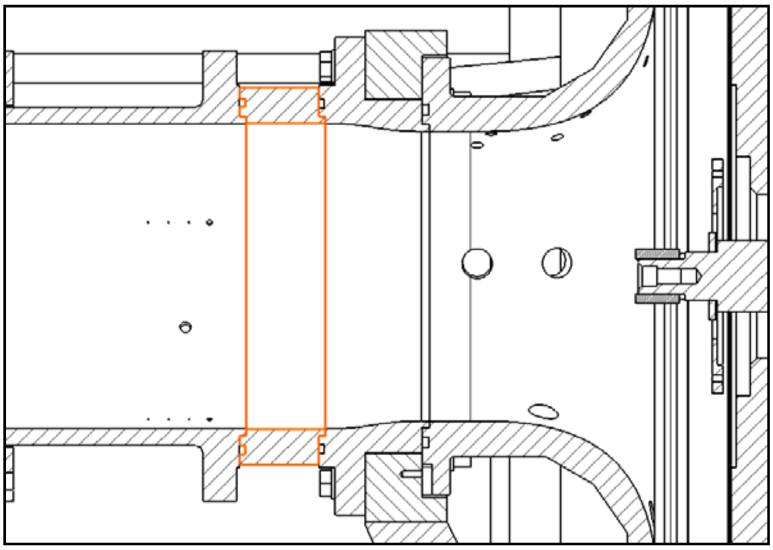

Fig. 5.7 Ring to be replaced by a Stator Blisk Configuration.

This is the only possible way and perhaps the best solution, since the ring geometry is very simple and not big. The other benefit is that the duct after the stator gets narrower and leads to a better flow field behind the stator, instead of having a continuous increase in hub diameter.

Usually, the stator blade row adds much more complexity to the stage design than the rotor and hence needs a long development and validation time. This leads to the idea of having an exchangeable stator blisk design.

On the one hand, considering the high cost and especially the manufacturing time of two months involved for an aluminium blisk, this is not an acceptable solution.

These two issues lead on the other hand to further ideas to realize an exchangeable stator design:

- The material and the manufacturing technique must be changed
- Avoiding the weight to be carried by the blisk by adding struts
- Alignment is achieved through adjusting the struts

These ideas result in a design presented in Fig. 5.8, which allows a very easy stator blisk replacement. The stator ring consists no longer out of one ring as intended in the beginning, but it is split into three pieces:

- Outer ring (outer casing)
- Stator blisk
- Inner ring (inner casing)

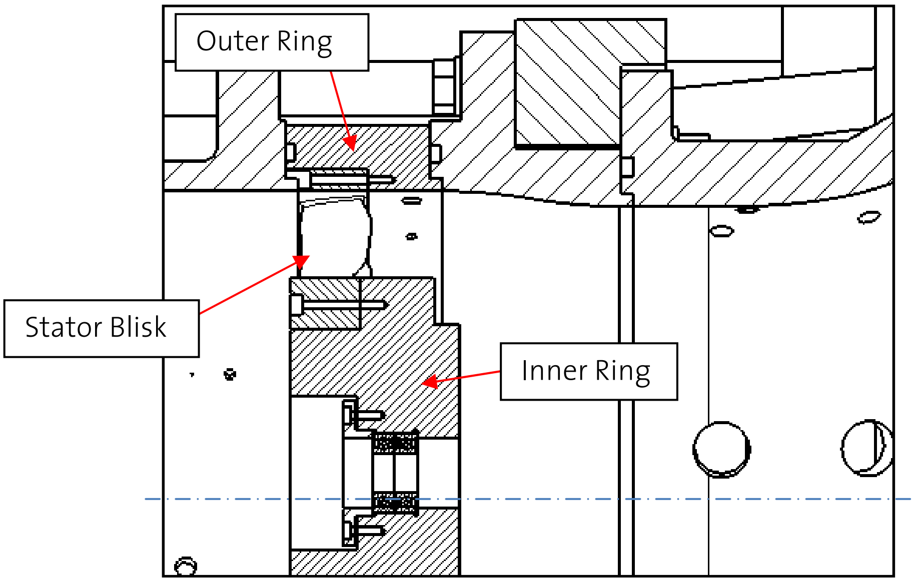

Fig. 5.8 Stator Blisk Configuration.

The idea is to have the replaceable stator blisk screwed to an aluminium inner and outer ring, which are already concentrically aligned to each other by four struts as depicted in Fig. 5.9. Like this, only the struts are carrying all the weight and the stator blisk is automatically aligned by fitting. As shown in Fig. 5.8 and 5.9, the bearings supporting the shaft are located inside the stator inner ring. Therefore, it becomes clear how important it is, to have the two rings perfectly concentrically aligned to each other, in order to have the shaft perfectly centred.

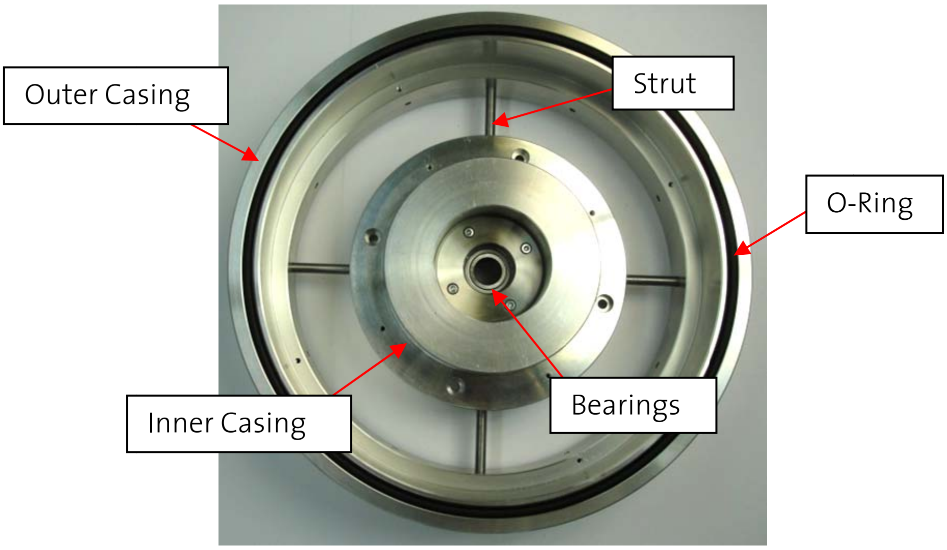

Fig. 5.9 Manufactured Stator Blisk Configuration.

An economic way to manufacture the stator blisk is rapid prototyping. The manufacturing time is reduced to only maximum one day instead of two months, as it can be ordered next door in the Institute of Robotics and Intelligent Systems. The other advantage is the reduced cost. The cost of such a blisk is about a tenth of the one made of aluminium. This way, flexibility and a compressed design-to-manufacturing cycle is achieved. The material is FullCure 720 with a tensile strength of 60 N/mm^2. This is a weak and brittle material compared to aluminium, but with good technical properties and strong enough to stand the aerodynamic forces, since no other forces are acting on the blisk itself. The blisk is manufactured by an ultra-thin-layer 3-dimenionsional printing system EDEN 350V, utilizing the Polyjet™ Polymer Jetting technology as shown in Fig. 5.10.

Fig. 5.10 3D Printing System EDEN 350V.

The FullCure 720 material is available in cartridges of 3.6 kg liquid content. The jetting heads print the desired product layer by layer on a tray as can be seen in Fig. 5.11. The tray size and hence model size is maximal 350 x 350 x 200 mm.

Fig. 5.11 A Stator Blisk Polymer Layer printed on a Tray.

The build resolution is given as follows:

X-Axis	600 dpi	0.042 mm
Y-Axis	600 dpi	0.042 mm
Z-Axis	1600 dpi	0.0016 mm

Table 5.4 Rapid Prototyping Build Resolution.

To support the structure and to ensure hard grid edges, a gel-like support material is printed by separate heads around the geometry. Fig. 5.12 depicts the printed stator blisk, surrounded by the support material.

Fig. 5.12 Printed Stator Blisk, surrounded by Support Material.

The printing job itself is finished after eleven hours. Nevertheless, the model cannot be used right after and the support material cannot be easily removed by a water jet. Also, special care is required while removing the support material, since the aerofoils are very thin and can brake. Surprisingly, the aerofoils can easily stand the forces of the strong thin water jet used to clean the models as well as the forces of an air blast (6 bars). After removing most of the support material by a water jet, the blisk is laid in a caustic soda solution for a couple of hours to remove the rest of the persistent supportive material. All together, it takes about 5 hours to remove all the supportive material. Fig. 5.13 shows the cleaned stator blisk and the through holes for the fixation at the inner and outer ring.

Fig. 5.13 Cleaned and ready-to-use Stator Blisk.

As mentioned above, the purpose of the four struts is to carry the weight of the structure and to align the stator inner ring, which supports the shaft by bearings, with the outer ring. The latter is aligned by fitting to the other rings in the measuring section. This leads to a perfectly centred shaft, relative to the rings. It is therefore obvious how important the adjustment of the struts is. Any misalignment causes the system to fail. Hence, the struts must be designed in a way that they can be very fine tightened, in order to adjust the two rings with a very high accuracy. This is realized by a fine pitch thread instead of a normal thread. The stator outer ring is sealed by an O-ring underneath the bolt head. The strut diameter is 6 mm and is made of an M8 bolt. First, the shaft it is turned down to the desired diameter and then the fine pitch thread is taped. Fig. 5.14 shows a strut with an O-ring applied for sealing purposes.

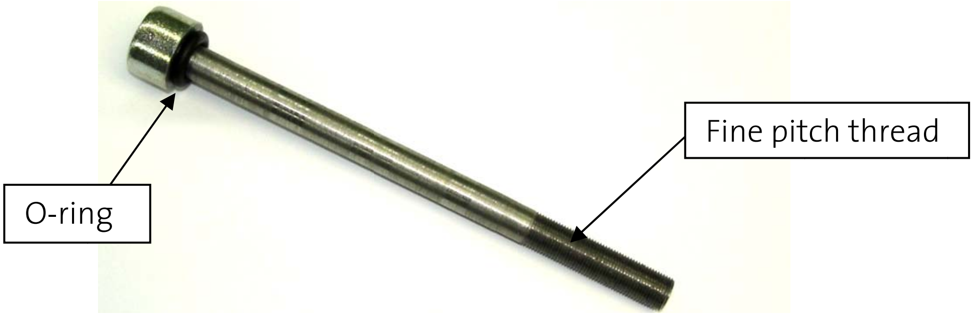

Fig. 5.14 One of the Four Struts with applied O-ring.

The stator outer ring is mounted and fixed on a drilling machine and concentrically aligned by an alignment tool which is clamped in the drill chuck as shown in Fig. 5.15. Then the two rings are screwed together by the four struts, without fastening them. The inner ring is centred by fastening the struts and keeping an eye on the alignment tool, whereas always two neighbouring struts are fastened simultaneously and then the other two directly opposed. This procedure is followed until all four struts are well tightened as depicted above in Fig. 5.14.

Fig. 5.15 Stator Blisk Alignment Procedure.

5.4.4 Shaft Design

The existing shaft of *RIGI* has been designed for centrifugal impellers and is therefore too short to be used for an axial compressor configuration.
The idea is to extend this shaft by using an attachment and a coupling as simplified illustrated in Fig. 5.16.

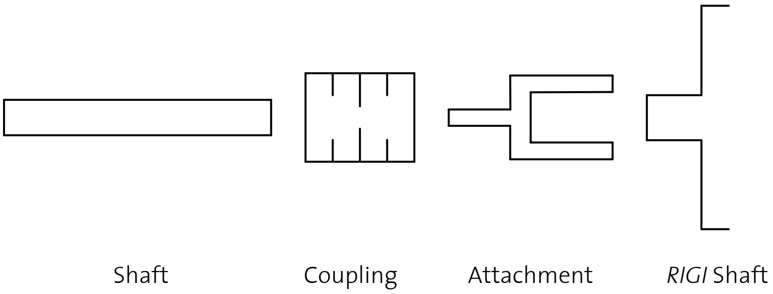

Fig. 5.16 Simplified Shaft Configuration.

Fig. 5.17 shows these four single elements. This chapter is mainly focused on the shaft design (Fig. 5.17a). Chapter 5.4.9 goes into detail of the coupling *KHS 15*, shown in Fig. 5.17b. The short *RIGI* shaft (Fig. 5.17d) has already two grooves eroded for transferring the torque to impellers via a shaft hub joint. Therefore, the attachment (Fig. 5.17c) is simply designed as a counterpart, with grooves eroded inside to keep the same joint. Therefore, the torque stemming from the *RIGI* shaft is transferred via the attachment to the coupling and from the coupling finally to the shaft and therefore to the rotor.

Fig. 5.17 a) Shaft b) Coupling KHS 15 c) *RIGI* Attachment d) *RIGI* Shaft

The shaft design is presented in the following figure. It is machined out of stainless steel and contains several features as shown in Fig. 5.18 and undergoes a long manufacturing process.

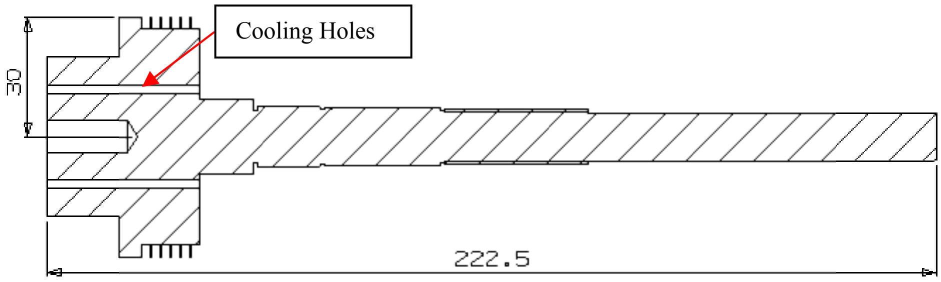

Fig. 5.18 Shaft with Cooling Holes for Bearing Cooling.

Several great demands are made on the shaft:

- Rotor fixation and powering
- Pivot-mounting
- Sealing
- Bearing cooling
- Coupling interface
- Concentricity (Circular grinding)
- High Balance

The rotor is shrunk on the shaft and fixed axially. The shrink fit doesn't allow any relative motion between the shaft and the rotor blisk up to a rotational speed of 26'500 RPM, which affects the balance positively. The following section describes how the shrink fit is designed. The rotor blisk is made of high-strength aluminium, while the shaft is made of stainless steel.

5.4.5 Shrink Fit

Fig. 5.19 shows a model of the shrink fit and the relevant dimensions. "D" represents the simplified rotor disk with an outer radius of 77 mm and an inner radius of 20 mm. "S" represents the solid shaft.

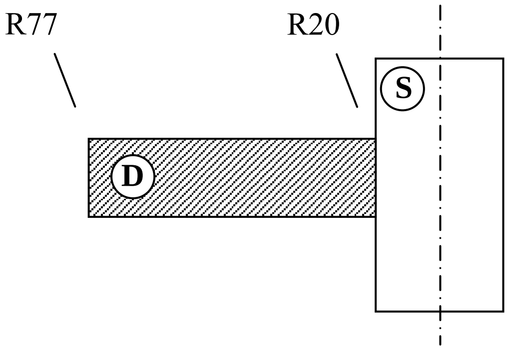

Fig. 5.19 Shrink Fit Model.

The shrink fit is calculated after manufacturing the rotor. Therefore, the rotor disk inner diameter is given by the actual size of -35 µm and only the shaft diameter has to be matched. An interference fit of n6 is necessary for this application. This results ideally in a ΔD of 60 µm, which is quite high. The shrinking must be carried out very quick and carefully.
Table 5.5 and Fig. 5.20 give an overview of the shrink fit dimensions.

	Disk	Shaft
	actual size	n6
Ø 40 mm	- 35 µm	+ 17 µm + 33 µm

Table 5.5 Shrink Fit Dimensions for a Shaft Diameter of Ø 40 mm.

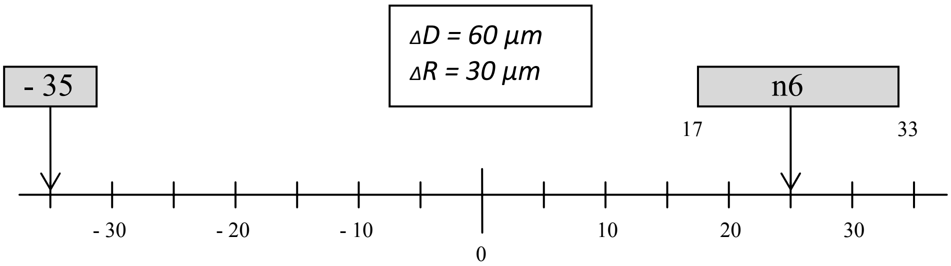

Fig. 5.20 Shrink Fit Dimensions for a Shaft Diameter of Ø 40 mm.

The equations for the radial and tangential stresses as well as the radial displacement of a rotating annular disc of uniform thickness are given by [Dubbel]:

$$\sigma_r = c_1 + \frac{c_2}{r^2} - \alpha\omega^2 r^2 \qquad \text{(Eq. 5.15)}$$

$$\sigma_\varphi = c_1 - \frac{c_2}{r^2} - \beta\omega^2 r^2 \qquad \text{(Eq. 5.16)}$$

$$u = \frac{r}{E}(\sigma_\varphi - \nu\sigma_r) \qquad \text{(Eq. 5.17)}$$

$$\alpha = \frac{3+\nu}{8}\rho \qquad \text{(Eq. 5.18)}$$

$$\beta = \frac{1+3\nu}{8}\rho \qquad \text{(Eq. 5.19)}$$

	Aluminium	**Steel**
Young's modulus	$E_{Alu} = 0.7 \cdot 10^5\ MPa$	$E_{Steel} = 2.15 \cdot 10^5\ MPa$
Density	$\rho_{Alu} = 2700\ \frac{kg}{m^3}$	$\rho_{Steel} = 7800\ \frac{kg}{m^3}$
Poisson's ratio	$\upsilon_{Alu} = 0.34$	$\upsilon_{Steel} = 0.3$
Coefficient of thermal expansion	$\lambda_{Alu} = 23.4 * 10^{-6}/\mathrm{K}$	$\lambda_{Steel} = 12 * 10^{-6}/\mathrm{K}$

Table 5.6 Material Properties for Aluminium and Steel.

The following boundary conditions are assumed to compute the unknowns c_1 and c_2.

- The radial stress at inner radius of the disk is the same along the shaft.
- The outer radius of the disk is free of stresses.
- The radial displacement difference between the disk and the shaft must equal ΔR.
- For a solid shaft, c_{2S} is zero.

Boundary conditions: $\sigma_{rD}(R20) = \sigma_{rS}(R20)$

$\sigma_{rD}(R77) = 0$

$u_D(R20) - u_S(R20) = \Delta R$

$c_{2S} = 0$ (Solid shaft)

Solving the 3x3 equation system:

	c_{1D}	c_{2D}	c_{1S}
$\Delta R = 30\ \mu m$	$5.7 \cdot 10^7$	-20907	$1.14 \cdot 10^7$

$R = 20\ mm$	$\sigma_{rD} = 1.07 \cdot 10^6$	$\sigma_{\varphi D} = 1.07 \cdot 10^8$	$u_D = 3.05 \cdot 10^{-5}$
	$\sigma_{rS} = 1.07 \cdot 10^6$	$\sigma_{\varphi S} = 5.44 \cdot 10^6$	$u_S = 4.76 \cdot 10^{-7}$

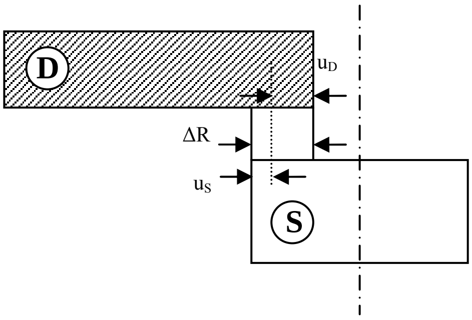

Fig. 5.21 Radial Displacement occurring in the Shrink Fit.

Fig. 5.21 illustrates the relation between the different radial displacements.

The next step is to calculate the assembly temperature for the shrink fit [INA].

$$T = T_0 + \frac{2 \cdot \Delta R + \frac{2 \cdot R20}{1000}}{\lambda_{Alu} \cdot (2 \cdot R20 - 0.35 \cdot 10^{-16})} = 129.84\ ^\circ\mathrm{C} \qquad \text{(Eq. 5.20)}$$

This is not a high temperature and can be easily achieved using a portable hotplate without damaging the material.

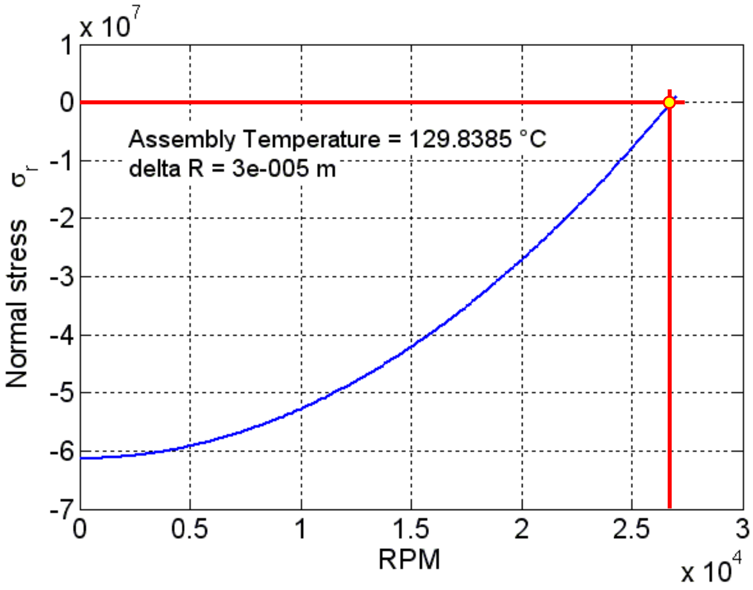

Fig. 5.22 Normal Stress in the designed Shrink Fit as a Function of the Rotational Speed.

The designed resulting radial stress at R=20 mm as a function of the rotational speed is shown in Fig. 5.22. It can be seen that a relative motion between the disk and the shaft can only occur for rotational speeds higher than 26’500 RPM, when the radial stress becomes bigger than zero.

RIGI offers a maximal rotational speed of 22’000 RPM, the shrink fit is therefore designed with a safety factor of at least 1.2.

As mentioned above, the shrinking must be carried out very quickly and carefully. Fig. 5.23 shows the individual parts of the shaft-rotor apart and assembled. The rotor blisk is fixed axially with a left-hand threaded screw.

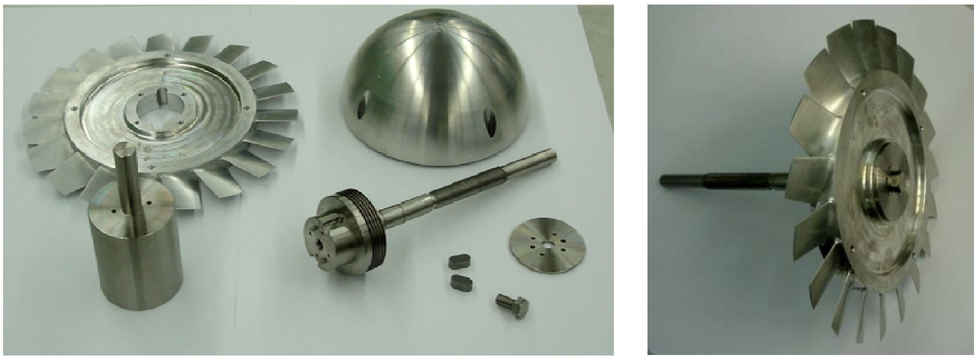

Fig. 5.23 a) Individual Parts of the Shaft-Rotor Assembly b) Shaft Rotor Assembly.

5.4.6 Labyrinth Sealing

Three relevant issues have to be considered in the present test rig design.

- Due to the design of *RIGI* and the existing limited accessibility, the length of the hub cannot be extended to the housing of *RIGI*.
- A gap exists between the rotor and the stator.
- The cooling holes in the cone and in the shaft are considered for ventilation in order to cool the bearings.

The following assembly drawing on next page (Fig. 5.25) shows what would happen if there are non existing cooling holes in the cone as shown in Fig. 5.24 and no sealing designed. The sealing prevents or at least minimizes the pressure equalisation that would take place between the high pressure field after the rotor and the lower pressure field inside the hub. This non-ideal case is indicated by a red flow path. At the end of the hub, a certain mass flow is sucked into the hub, following the path through the bearings and finally rejected into the again through the gap between the rotor and the stator. This leads to an undesired efficiency loss.

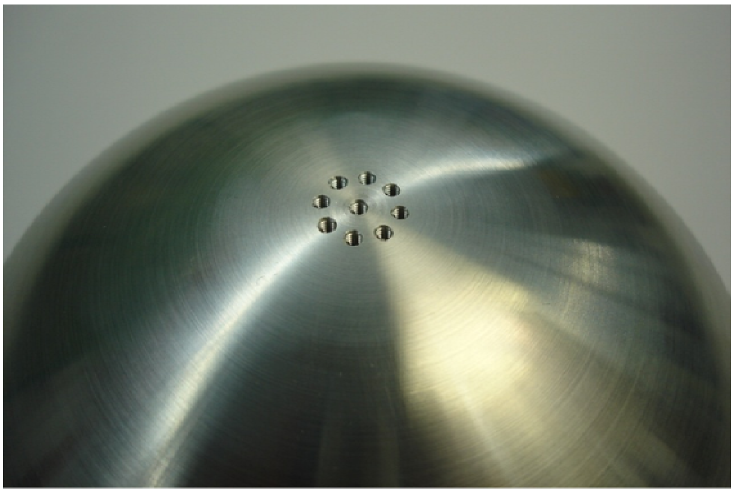

Fig. 5.24 Cooling Holes in the Cone.

The next figure shows the designed sealing in order to have the bearings cooled by a flow due to pressure equalization from the high pressure region behind the stator and the inlet of the compressor. The air following the blue flow path is pushed through the bearings, then through the holes in the shaft and finally injected into the compressor inlet flow through the holes in the cone. Like this, there is almost no leakage flow occurring between the rotor and stator that would negatively impact the system efficiency.

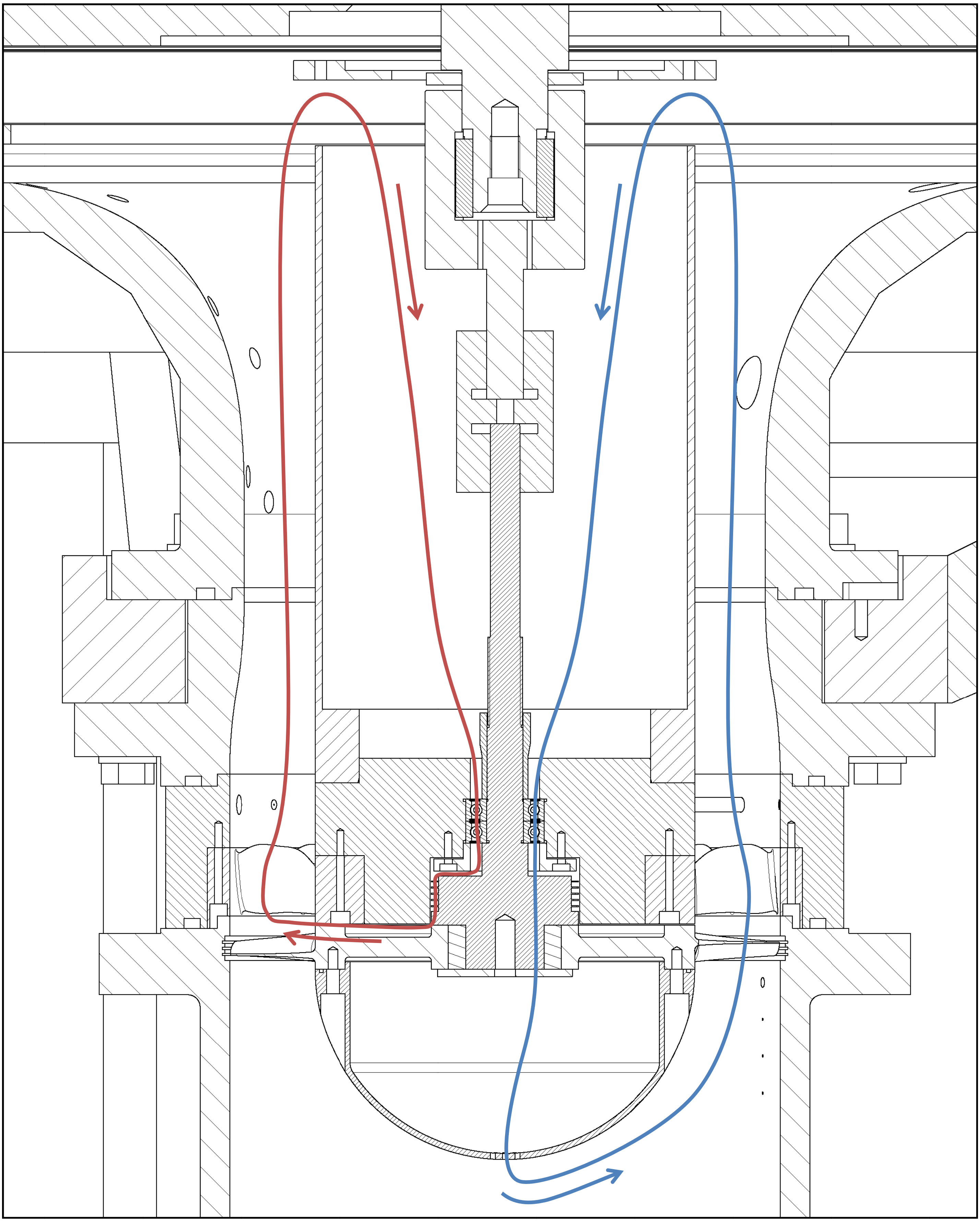

Fig. 5.25 Flow Paths due to Pressure Differences.

The following design procedure and calculation explain how the in Fig. 5.26 shown labyrinth gap sealing is designed and the resulting leakage mass flow between the rotor and the stator is quantified.

Fig. 5.26 Five Fin Labyrinth Gap Sealing.

The flow resistance of the sealing distance is increased by constructive measures. The gap between the shaft and the casing to guarantee the operational safety leads in any case to a certain leakage mass flow. This gap is designed based on an empirical equation (Eq. 5.23) given by G. Sörgel, which accounts for rotor bending, oscillations, casing deformations etc.. The Labyrinth gap sealing allows any axial relative motion between the shaft and the casing.

Fig. 5.27 shows the five fin labyrinth gap sealing design with all the relevant parameters.

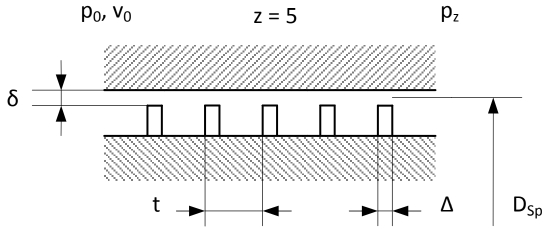

Fig. 5.27 Five Fin Labyrinth Gap Sealing [G. Sörgel].

Design parameters

$$D_{Sp} = 0.06\ m$$
$$A_{Sp} = 0.06\ m$$
$$t = 2.5 \cdot 10^{-3}\ m$$
$$C = 0.6$$
$$\Delta = 0.5 \cdot 10^{-3}\ m$$
$$p_0 = 1\ bar$$
$$p_z = p_0 \cdot pr = 1.05\ bar$$
$$v_0 = \frac{1}{\rho_0}$$

The leakage mass flow $\dot{m}_{Sp}$ is computed using the following equation [G. Sörgel]:

$$\dot{m}_{Sp} = k_{\ddot{u}} \mu_{Sp} A_{Sp} \sqrt{\frac{{p_0}^2 - {p_z}^2}{z p_0 v_0}} \qquad \text{(Eq. 5.21)}$$

Where A_{Sp} is the through flow area

$$A_{Sp} = \pi D_{Sp} \delta \qquad \text{(Eq. 5.22)}$$

The gap δ is computed based on an empirical correlation

$$\delta = C * \frac{Dsp}{1000} + 0.00025 = 2.86 \cdot 10^{-4}\ m \qquad \text{(Eq. 5.23)}$$

where C is an empirical constant.

It has been found that from the manufacturing tolerances point of view it is risky to have such a narrow gap. Instead, a value of

$$\delta = 5 \cdot 10^{-4}\ m$$

has been chosen to prevent any damages in the system.

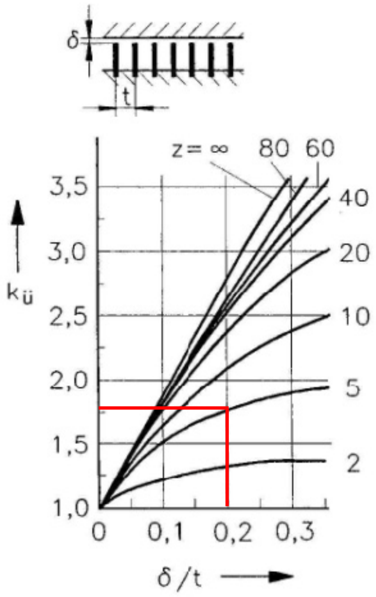

Fig. 5.28 Bridge Over Factor $k_ü$ for the Labyrinth Gap Sealing [G. Sörgel].

The bridge over factor $k_ü$ is extracted from the graph in Fig. 5.28

$$\frac{\delta}{t} = 0.2 \quad \rightsquigarrow \quad k_{\text{ü}} = 1.76$$

The flow coefficient μ_{Sp} is determined experimentally and extracted from Fig. 5.29

$$\frac{\delta}{\Delta} = 1 \quad \rightsquigarrow \quad \mu_{Sp} = 0.745$$

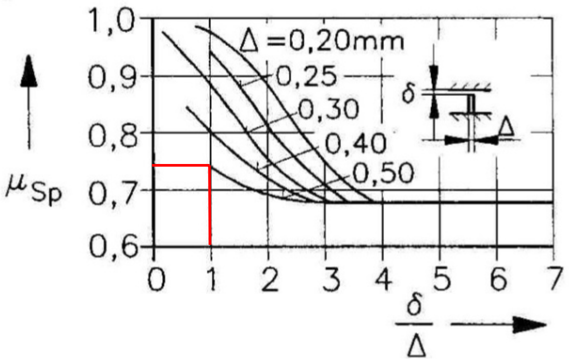

Fig. 5.29 Influence of the Throttle Ring Width on the Flow Coefficient μ_{Sp} [G. Sörgel].

This leads to a mass flow of

$$\dot{m}_{Sp} = k_{ü}\mu_{Sp}A_{Sp}\sqrt{\frac{{p_0}^2 - {p_z}^2}{zp_0v_0}} = 0.006\ \frac{kg}{s}$$

where $p_z - p_0$ is the pressure difference across the sealing.

Compared to the compressor design mass flow, the leakage mass is less than one percent. Therefore, the impact on the efficiency is negligible and it can be concluded that nearly all the mass flow due to the pressure equalization is pressed as desired through the bearings.

5.4.7 Bearings

The bearing arrangement for the compressor rotor is discussed in this section. The main goal is to have a shaft support and a safe operation up to a rotational speed of 22'000 RPM. The shaft is with 22.3 cm very long. To avoid overhang effects, the bearings are located as near as possible to the rotor blisk. A pair of ball bearings is supporting the shaft as depicted in Fig. 5.30. The bearings are fixed axially on the shaft as well as on the stator inner ring.

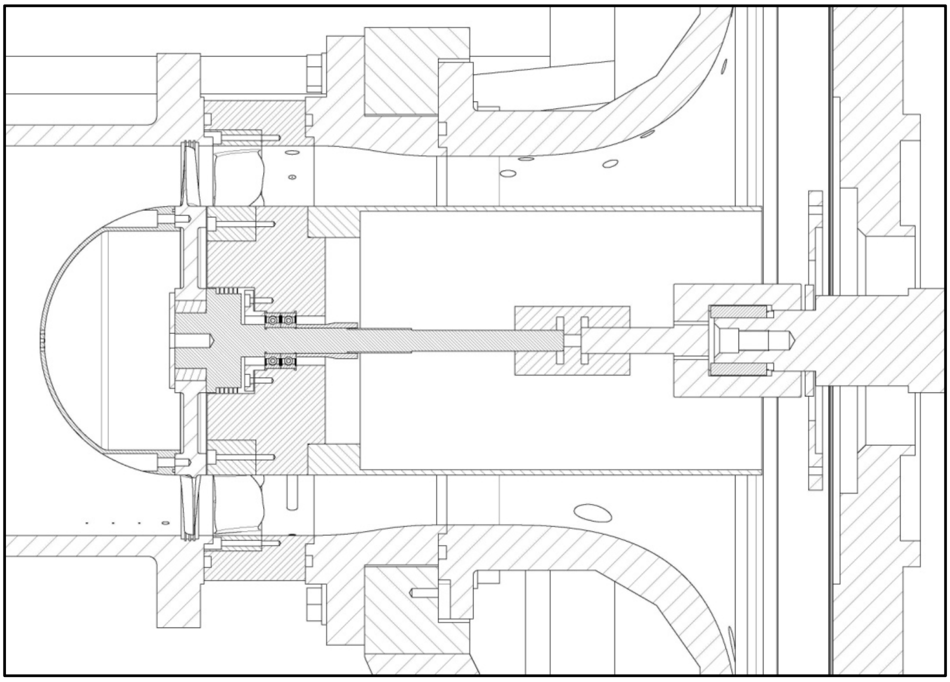

Fig. 5.30 Axial Compressor Configuration: Two 6202-2Z* Explorer Deep Groove Ball Bearings are supporting the Shaft.

A pair of SKF 6202-2Z Explorer single row, deep groove ball bearings with an inner diameter of 15 mm is supporting the shaft. Single row, deep groove ball bearings are particularly versatile. They are simple in design, non-separable, suitable for high speeds and are robust in operation, requiring little maintenance. Deep raceway grooves and the close conformity between the raceway grooves and the balls enable deep groove ball bearings to stand axial loads in both directions, in addition to radial loads, even at high speeds.
Single row deep groove ball bearings are the most widely used bearing type. They are manufactured by SKF for a wide range of sizes.

Single row deep groove ball bearings have only limited ability to accommodate misalignment. Any misalignment will result in an increased bearing noise and reduced bearing service life or even to failure.

5.4.8 Casing

The casing geometry is already given by the existing ring configuration of the measurement section and therefore no casing needs to be designed. Fig. 5.31 shows the configuration for an axial compressor. The gap between the rotor blade tip and the casing, known as the tip clearance which is typically one percent of blade span, is 0.34 mm.

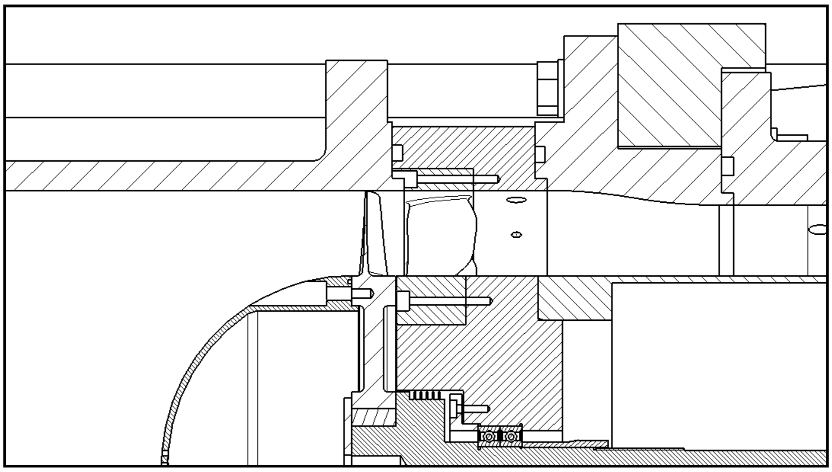

Fig. 5.31 Casing Geometry given by the already existing Rings of the Measurement Section.

The rotor structure and stress analysis for design speed discussed in chapter 4.5.1, predicts a maximal occurring deformation of 0.0498 mm. Compared to the designed tip clearance (1 % of blade span), this is 14.7 %. Nevertheless, during testing at only 12’000 RPM, the blades scratched the wall. It turned out to be a result of several effects and the casing was modified in order to prevent the blades from damage and to minimize the tip clearance at the same time. Details will be discussed later in chapter 5.6.1.

The maximal deformation occurring in the blisk is 0.0498 mm for the scaled down model. This makes 14.7% out of the designed tip clearance, which itself is 1% of blade span.

5.4.9 Coupling

The torque stemming from the *RIGI* shaft is transferred through the attachment to the coupling and by the coupling finally to the shaft and later to the rotor.
The components of the axial compressor are all designed for a rotational speed up to 25’000 RPM, including the coupling. Since this is a low torque case, it is not necessary to have a coupling able to transfer high torques.

The metal bellows coupling of the model *KHS 15* shown in Fig. 5.32 is highly balanced for a rotational speed of 25’000 RPM. It can transfer torques up to 15 Nm. It has a low mass moment of inertia and is corrosion free. A special conical clamping ring acts as a friction-locked shaft to collar connection. The clamping ring is controlled pressed against the conical hub through the specified tightening torque (Table 5.7). The initial gap width is reduced to zero. Hence, canting is not possible respectively an overload of the clamping ring is excluded. There are three force-off-threads next to the six bolts on each side of the coupling to facilitate the disassembling.

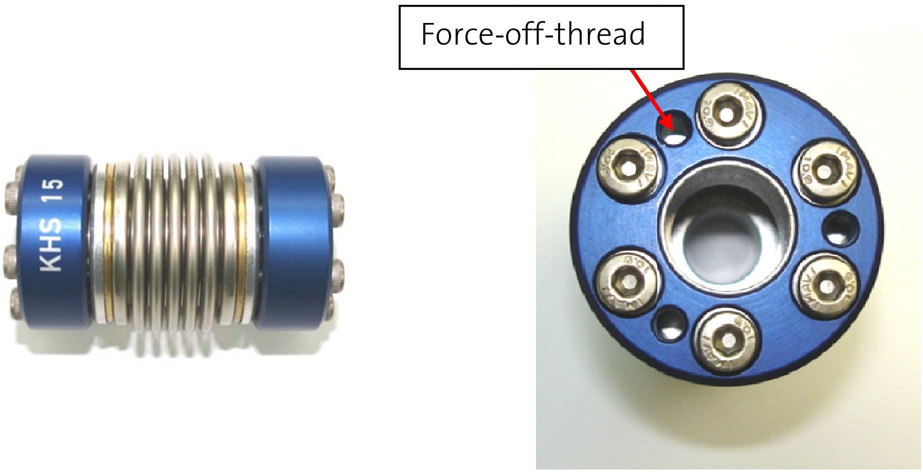

Fig. 5.32 Side and Front View of the Coupling KHS 15 with three Force-Off Threads on each side.

Table 5.7 and 5.8 show the specifications of the coupling *KHS 15*.

moment of inertia [10-3kgm2]	torsional stiffness [Nm/arcmin]	Max. shaft displacement [mm]		axial spring rate [N/mm]	lateral spring rate [N/mm]	mass [kg]	tightening torque of screws [Nm]
		axial ±	lateral				
0.03	2	0.5	0.1	20	90	0.15	3

Table 5.7 Technical Specifications of the Coupling KHS 15.

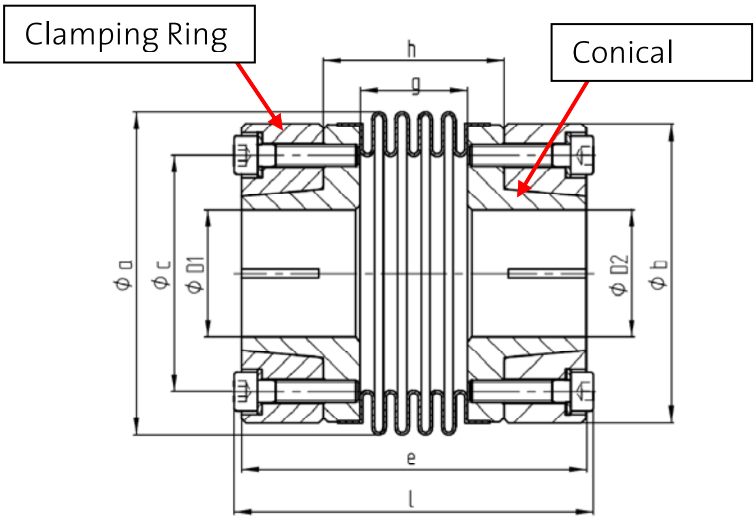

Fig. 5.33 Coupling Dimensions.

øa	øb	øc	e	6 x f	g	h	l	øD1	øD2
39.5	38	27	63	M4	18	32	66	12	15

Table 5.8 Geometry Specifications of the Coupling KHS 15.

From the scaling analysis of chapter 5.3 results a torque of approximately 2.5 Nm which acts on the shaft. As this coupling can transfer up to 15 Nm, the safety factor is 6.

However, the manufacturer guarantees an even higher safety factor as the following calculation for a shaft diameter of 12 mm shows.

To transfer 15 Nm of torque, a preload force of 711 N must be applied over the 6x M4 bolts (no safety factor considered).

The maximal preload force is 4425 N for a M4 bolt, based on a tightening torque of 3 Nm. This gives a safety factor of 6.22, consequently.
In other words, theoretically a 6.22 times bigger torque can be transferred by the coupling, hence 93 Nm. This is pretty high much higher than the specified 15 Nm. So, even with a safety factor of 2 a three times bigger torque can be transferred via the friction-locked shaft collar connection.

However, to reach these values, a clean and a greaseless surface of the shaft and the borehole must be ensured.

5.4.10 Rotor Balancing

The process of redistributing the mass attached to a rotating body in order to reduce vibrations arising from centrifugal forces is known as shaft balancing. Also known as rotor balancing.

A rotating shaft supported by ball bearings with an attached mass, such as in this case a compressor disk, is called a rotor. If the rotor centre of mass is not exactly on the bearing axis, a centrifugal force will be transmitted via the bearings to the casing. The horizontal and vertical components of this force are periodic shaking forces that can travel through the casing to creating serious vibrational problems for adjacent components.
Any rigid shaft may be dynamically balanced by adding or subtracting a definite amount of mass at any convenient radius in each of the two arbitrary transverse cross sections of the rotor. The so-called balancing planes selected for this purpose are usually located near the ends of the rotor, where suitable shoulders or balancing rings have been machined to permit the convenient addition of mass (lead weights, calibrated bolts, and so on) or the removal of mass (by drilling or grinding). Long rotors, running at high speeds, may undergo appreciable elastic deformations. For such flexible rotors it is necessary to utilize more than two balancing planes.

In this case, the parts which should be balanced are the cone, the rotor blisk and the shaft. Fig. 5.34 shows these parts assembled together and indicates the two balancing planes, planes 1 and 2. The first plane is given by the shoulder of the rotor. The second plane goes through the cone, where the material is removed from the cone interior, since from an aerodynamic point of view it is not applicable to remove material from the surface. This implicates access to the second plane.

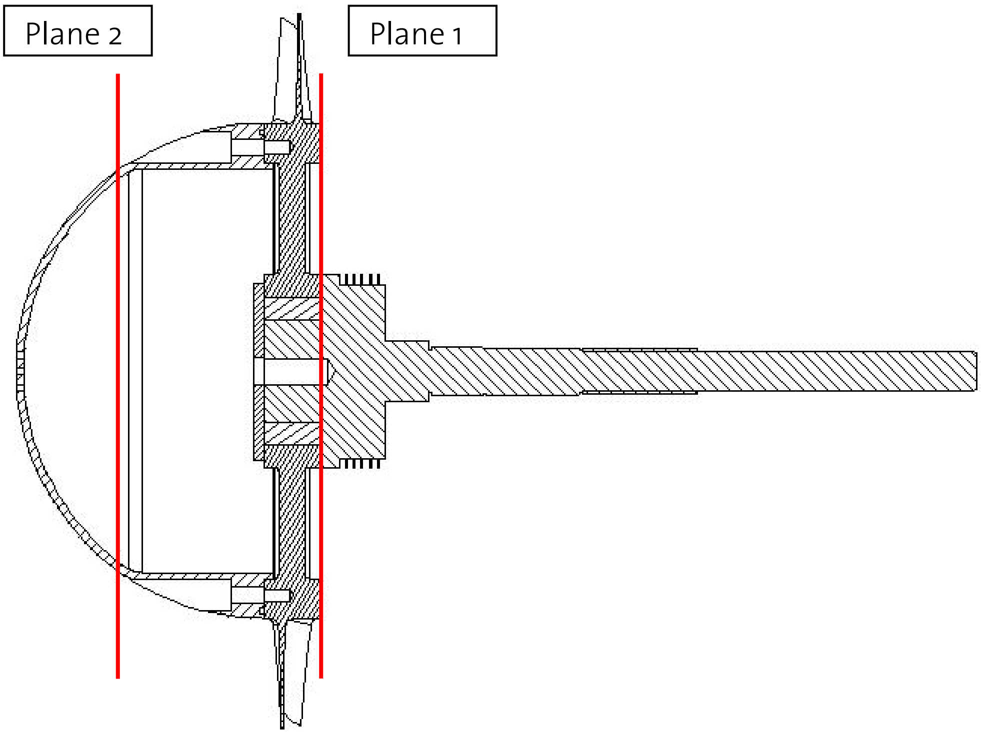

Fig. 5.34 Rotor-Shaft Assembly with Two Balancing Planes indicated.

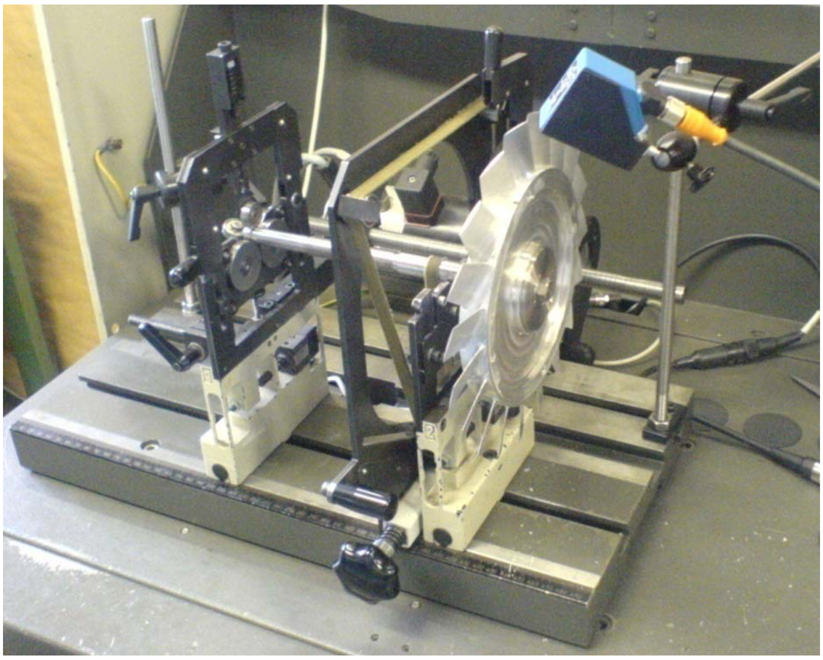

Fig. 5.35 Rotor-Shaft Assembly being balanced on a Schenck HS 10/CAB 690 Balancing System.

The rotor balancing has been performed by a high precision Schenck balancing system HS 10/CAB 690 that drives the rotor by a belt drive right next to the bearing seat as shown in Fig. 5.35. The assembly is supported at two locations. Of course, at the location of the bearing seat and at the very end of the shaft, the location of the coupling.
All the measurements were performed with very high accuracy at a rotational speed of 1'100 RPM, guaranteeing an up to 25'000 RPM balanced rotor.

The first static measurement showed a high rotor unbalance. It has been found that the cone is responsible for this unbalance and that the assembly, shaft with attached rotor blisk is very well balanced. Therefore, it has been decided to use the shaft with the attached rotor blisk as an auxiliary system, in order to balance first the cone separately. There also two balancing planes were necessary as can be seen in Fig. 5.36. One of them is the same as the one for the entire assembly. The new plane is located on the cone frontal area.

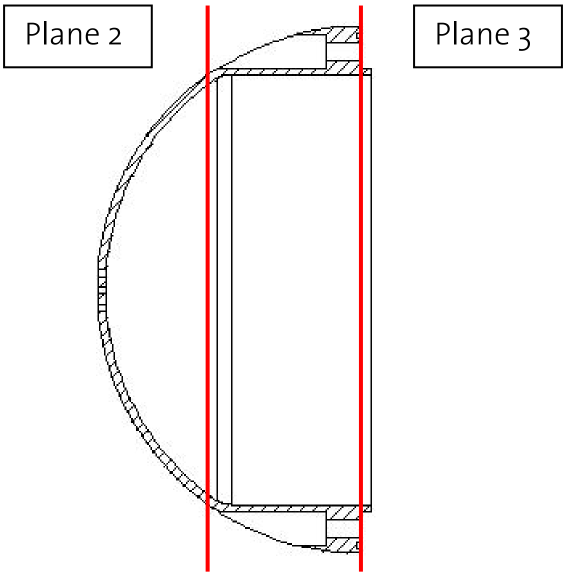

Fig. 5.36 Cone with Two Balancing Planes indicated.

It is difficult to turn the cone out of aluminium on a lathe, resulting in an unbalanced body. A lot of grinding was therefore necessary at plane 2, at the internal surface of the cone, shown in Fig. 5.37. The problem there was the thin wall thickness of 2 mm. Therefore, the grinding was done in each balancing step on a large area until the cone was balanced. At plane 3, no grinding was necessary, since drilling was possible. Thus, holes were drilled and a couple of tungsten screws in were added.

Fig. 5.37 Cone grinded from Inside at Location of the Balancing Plane 2 and drilled at Location of Balancing Plane 1.

After the high quality cone balancing, the cone was fixed by the four M5 screws to the rotor blisk, with the sealing O-ring in between. Loctite was also used for locking the screws. Four rapid prototyping inserts were glued into the four counter bore holes on the cone surface.

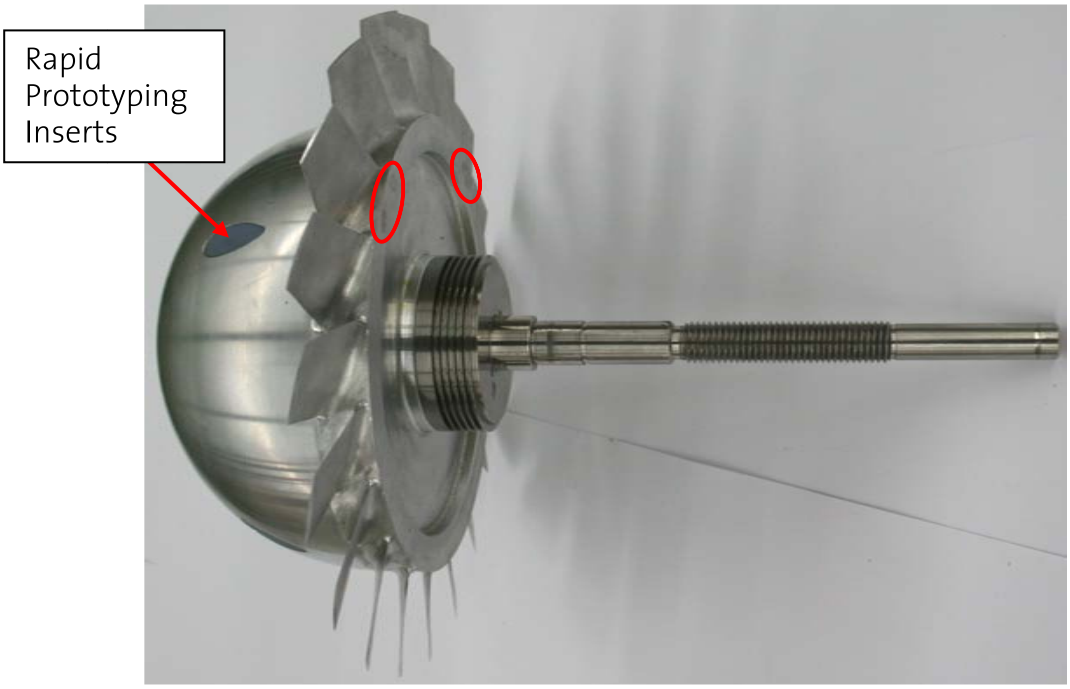

Fig. 5.38 Rotor grinded for Dynamic Balancing at Location of Balancing Plane 1.

In the final step the entire rotor-cone system is balanced by grinding the rotor blisk shoulder at plane 1 as shown in Fig. 5.38.

With this accurate balancing, the dynamic balancing at two planes is within a tolerance of 3 gmm, measured in quality grade G 2.5 according to DIN ISO 1940-1. The tolerance is computed by the Schenk system after entering values for weight, design speed and quality grade based on the following equations:

Rotor	
Mass	m = 2.75 kg
Design speed	n = 22'000 RPM
Requested quality grade	g = G 2.5

Table 5.9 Rotor Balancing Specifications.

Tolerable specific unbalance *e*:

$$e = g\left[\frac{30}{\pi \cdot n} \cdot 10^3\right] = 1.085\ g \cdot mm/kg \qquad \text{(Eq. 5.24)}$$

Tolerable unbalance *U*:

$$U = m \cdot e = 3\ gmm \qquad \text{(Eq. 5.25)}$$

The high quality class G 2.5 is necessary for this sort of application, due to the high design speed of 22'000 RPM. Any unbalance at that high speed may create serious vibration problems.

The Schenck system needs to be fed with the rotor dimensions and the location of the two balancing planes in order to perform the balancing. These values are entered according to Fig. 5.39 showing a rotor, supported at two locations.

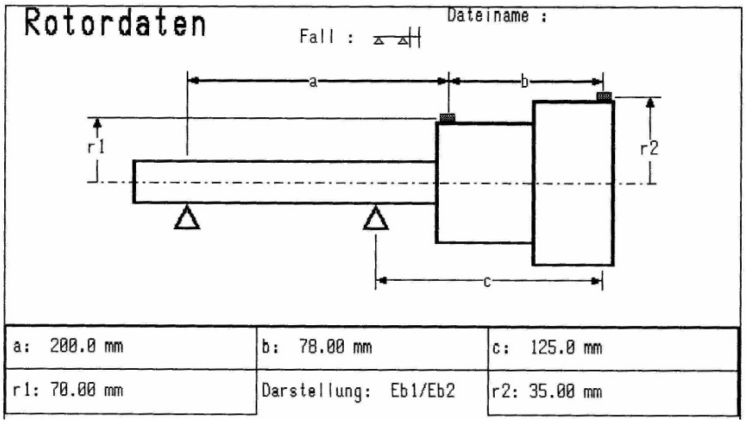

a: 200.0 mm
b: 78.00 mm
c: 125.0 mm
r1: 70.00 mm
Darstellung: Eb1/Eb2
r2: 35.00 mm

Fig. 5.39 Schenck Balancing System Rotor Model.

Fig. 5.40 shows the results for the two balancing planes and indicates the location of the unbalance in each plane. The unbalance in each plane is within the tolerance. This guarantees a balanced rotor operation at design speed of 22’000 RPM.

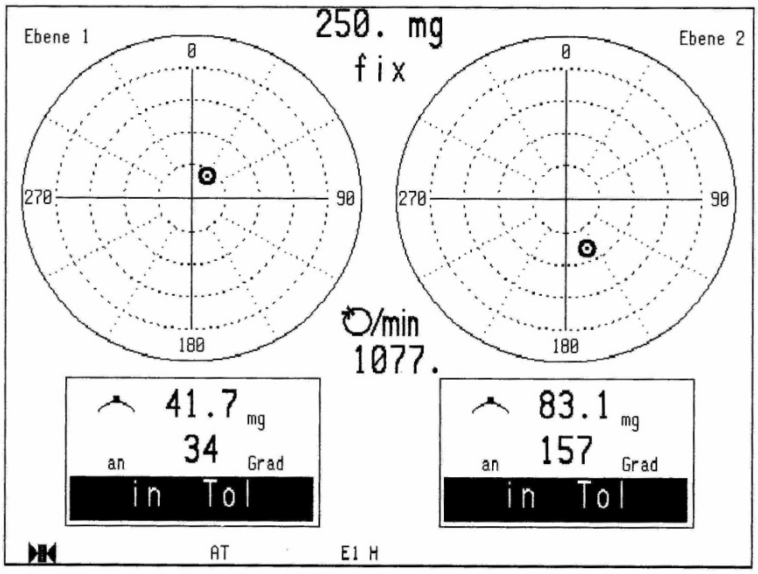

Fig. 5.40 Location of Unbalance at Balancing Plane 1 and 2.

5.4.11 Assembly Instructions

This chapter briefly explains how the axial fan is assembled.

1. Warm up the stator inner ring on a portable hotplate until the bore hole is wide enough for mounting of the two bearings inside the stator inner ring.

2. Attach the adjusted M3 screw for the axial accelerometer fixation to the counter bore shown in Fig. 5.41 and fix the axial accelerometer (type KS-95B.10).

3. Fix the bearings axially by screwing the bearing fixation flange to the stator inner ring.

4. The stator outer ring is mounted and fixed on a drilling machine and concentrically aligned by an alignment tool which is clamped in the drill chuck as shown in Fig. 5.42. Then the two rings are screwed together by the four struts, without fastening them. The inner ring is centred by fastening the struts while keeping an eye on the alignment tool, whereas always two neighbouring struts are fastened simultaneously and then the other two directly opposed. This procedure is followed until all four struts are well tightened as shown in Fig. 5.43.

Up to now, one unit is assembled together. The next steps explain how to assemble the individual parts (Fig. 5.44) of the shaft-rotor assembly depicted in Fig. 5.45.

5. Put the feather keys into the two grooves in the shaft.

6. Warm up the rotor blisk on a portable hotplate until the bore hole diameter is enlarged enough. (Don’t forget gloves).

7. Quickly stripe the rotor blisk with the right orientation over the shaft without to cant.

8. Fix the rotor blisk axially with the rotor axial fixation by fastening the left-hand-thread screw.

9. Screw the already balanced cone to the rotor.

10. Glue the four cone inserts with the two component glue Araldyte.
11. If any part changes are made, the balancing should be repeated. For further details about the balancing procedure, the reader is referred to chapter 5.4.10.

Now the two assemblies are ready and have to be brought together in order to obtain a simple and easy to use axial compressor configuration as shown in Fig. 5.46.

12. Feed the shaft-rotor assembly through the bearings up to where bearing sits.
13. Stripe the bearing fixation bush over the shaft until it reaches the bearing inner ring.
14. Screw the left-handed M14 nut up to the bearing fixation bush.
15. Use a screw wrench with a long lever arm to slowly screw the M14 nut. During this process the bearings are striped controlled over the bearing seat without any hammering or canting.
16. Fix the two radial accelerometers (KS94B.10) with the adjusted M3 screws.
17. Put a mark on the shaft at a distance of exactly 26.5 mm from the end.
18. Stripe the coupling of the type KHS 15 over the shaft up to the mark and fasten it by the six M4 screws with a tightening torque of 3 Nm.
19. Put a mark on the *RIGI* shaft attachment exactly at 26.5 mm from the end.
20. Feed the attachment through the coupling up to the mark and fasten it by the six M4 screws with a tightening torque of 3 Nm.

The axial compressor assembly is now almost completed and ready to be integrated into the test section (*RIGI*) for assembling the further parts.

21. The next step is to jack up the measurement section frame vertically in order to integrate the so far assembled compressor configuration and to install all the rings. This is done by the big crane in the hall.

22. Before screwing all the bolts together in order to fix the rings, it should be checked whether the rotor tip clearance is homogeneously distributed, using shims. Keep in mind that the cables for the accelerometer have to be fed outside through the shroud. Therefore make also sure that the radial accelerometer in the middle of the other two accelerometers points towards the three prepared holes in the shroud in order to prevent these cables from touching the shaft. This leads to a direct cable connection from the hub end to the shroud, as shown in Fig. 5.47.

23. Position the measurement section frame horizontally while taking care of the free hanging *RIGI* shaft attachment.

24. Feed each of the three accelerometer cables through a bored M8 screw first and then through the prepared holes in the impeller shroud and finally also through the hub.

25. Screw the three cables to the three accelerometers while holding the hub.

26. While still holding the hub, install the three brass cable run inside the hub, without tightening them definitively.

27. Stripe the hub over the shaft and fix it to the stator inner ring with four M5 screws after tightening the sensor cables inside. The cable run inside the hub must be positioned above the radial accelerometer in the middle of the other two accelerometers in order to prevent the appropriate cables from touching the shaft.

28. Tighten the screws of the cable run.

29. Screw the three M8 screws into the impeller shroud and seal them.

30. To ensure a proper and safe docking on the *RIGI* shaft, the RIGI shaft attachment must be exactly positioned in the middle and therefore concentrically aligned to the hub.

The axial compressor assembly as shown in Fig. 5.48 is finished and is ready to be attached to the test rig (*RIGI*).

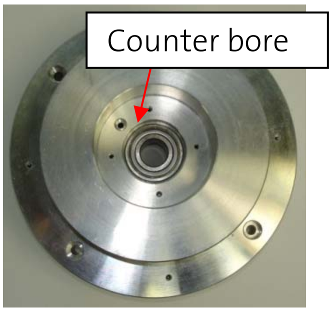

Fig. 5.41 M3 Counter Bore Hole for Axial Accelerometer Fixation.

Fig. 5.42 Stator Outer Ring mounted on a Drilling Machine for Alignment.

Fig. 5.43 Concentrically aligned Stator Ring Configuration.

Fig. 5.44 Individual Parts of the Rotor-Shaft Assembly.

Fig. 5.45 Rotor-Shaft Assembly.

Fig. 5.46 Ready to be integrated: Axial Compressor Assembly.

Fig. 5.47 The Three Accelerometer Cables are fed through the Impeller Shroud and connected to the M12 Module.

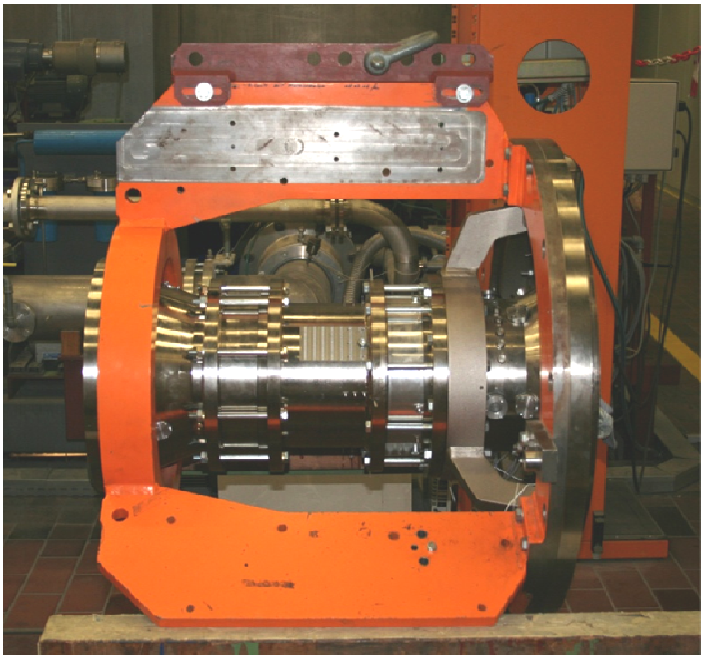

Fig. 5.48 Finished Assembly of the Axial Compressor Configuration.

5.4.12 Disassembly Instructions

Disassembling is pretty straight forward compared to assembling. Therefore only the disassembling of the bearings is discussed in this chapter. For this task, a couple of parts and tools as shown in Fig. 5.49 are manufactured to allow a controlled dismounting of the bearings and to prevent the bearing seats on the shaft from being damaged.

Fig. 5.49 Tool for Bearing Disassembly.

Keep on disassembling until an assembly remains as shown in Fig. 5.46. Then follow the procedure below.

1. Make sure that the hub is screwed to the stator inner ring.
2. Screw a M14 nut up to the middle of the thread on the shaft.
3. Stripe the bush over the shaft so that it is supported by the M14 nut.
4. Screw the quadratic aluminium plate (Fig. 5.49) with four M4 screws to the hub end.
5. Screw the big M14 bolt into the aluminium plate until the bolt fits into the bush.
6. Use a screw wrench with a long lever arm to slowly screw down the M14 bolt, which is pressing the bush on the M14 nut. During this procedure the bearings are striped controlled over the bearing seat without any

hammering or canting. Make sure, the shaft-rotor assembly does not fall down.

7. The axial compressor assembly is now split into two assemblies again. To remove the bearings from the stator inner ring, disassemble the stator assembly first.

8. Install the stator inner ring on a press and push the bearings slowly out of the casing.

5.5 Measurement Facilities

Two separate data acquisition systems record data during operation measured by installed sensors. Performance data is acquired in order to monitor and to control the operating conditions of the facility. The existing acquisition system is expanded in order to capture the performance and the safety of the axial compressor configuration.

5.5.1 Performance

To characterize the performance of the axial compressor, the pressure up and down stream of stage is measured. In order to do this, additional pressure measuring points are applied into the test section for wall static pressure measurements. Four locations are placed in series in front of the rotor, each includes four holes equally distributed in circumferential direction and the pressure is averaged pneumatically. This way, also a statement can be made about the change in pressure at the wall in front of the rotor. The last measurement location is placed downstream of the stator, where the wall static pressure is pneumatically averaged over eight equally spaced measurement holes. Fig. 5.50 shows the tubes of to the five pressure measurement locations. These five tubes are connected to a pressure scanner (type Netscanner 9816), which is a part of the existing data acquisition system, so that only a few changes are necessary in order to monitor the pressure signals.

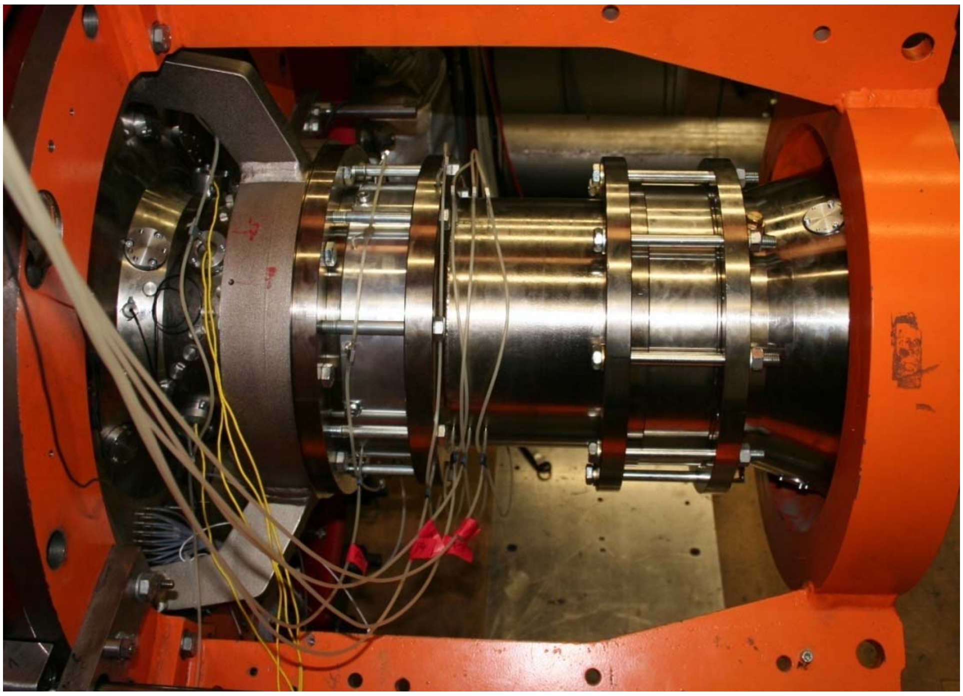

Fig. 5.50 Tubing for Pneumatic Pressure Measurements.

Additionally to the wall static pressure measurements, two platforms are designed up and downstream of the stage to install an existing aerodynamic probe FRAP system to allow a radial traverse to be measured (Fig. 5.51).

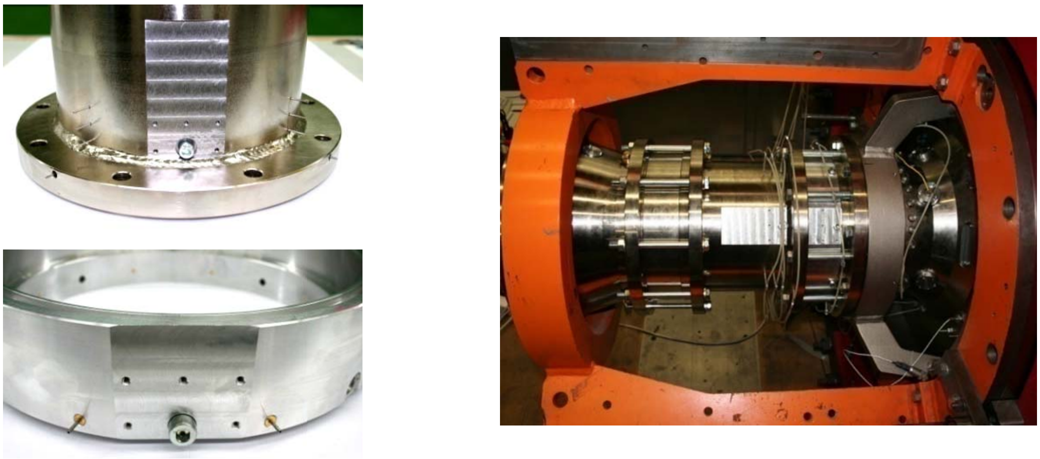

Fig. 5.51 A Platform is designed on Two different Rings, in front and behind the Stage to install an existing aerodynamic Probe FRAP System.

5.5.2 Vibrations

Vibrations are usually a reason for failure in turbomachinery design. There is a need to understand the causes of vibrations and to develop techniques to prevent them. Here, three miniature accelerometers of the type KS-94/95B.10 (Fig. 5.52a) are installed in the casing near the bearings to capture all vibrations during testing. Two of them capture vibrations in radial direction, mounted orthogonally relative to each other, and the third sensor captures vibrations in axial direction, as shown in Fig. 5.52b.

Fig. 5.52 a) Accelerometer KS-94/95B.10. b) Accelerometer Mounting Arrangement.

The used accelerometers piezoelectric. They generate an electric charge signal proportional to vibration acceleration. The active element of the accelerometers consists of a ceramic material with piezoelectric properties. Piezoelectric accelerometers are widely used as the most applied device for measuring absolute vibration. Compared to the other types of sensors, piezoelectric accelerometers have several advantages:

- Extremely wide dynamic range, low output noise - suitable for shock measurement as well as for almost imperceptible vibration
- Excellent linearity over their dynamic range
- Wide frequency range, high frequencies can be measured
- No moving parts - no wear
- Self-generating - no external power required
- Acceleration signal can be integrated to provide both velocity and displacement

Table 5.10 summarizes the specifications of the miniature accelerometers. It can be seen that the range is quite high in order to capture all possible critical vibrations in the system.

Miniature Accelerometers KS94B.10 KS95.10	
Output	ICP® compatible voltage output
Piezo system	Shear design
Voltage sensitivity	10 mV/g ±5%
Range	±600 g
Destruction limit	8000 g
Operating temperature	-20 °C / 120 °C
Weight without cable	2.4 gr
Case material	Aluminium / Stainless Steel
Connection	Sub miniature M3
Mounting	M3 thread in base

Table 5.10 KS94B.10 KS95.10 Miniature Accelerometers Specifications.

It is known that choosing an optimum mounting arrangement significantly improves the accuracy. The sensors are attached to the casing by a M3 bolt, so that they can be easily removed if needed. This leads to best performance, particularly at high frequencies. The accelerometer base and the test object should have clean, flat, smooth, unscratched and burr-free surfaces. A scratched accelerometer base can be applied to a lapping plate for restoration of flatness. If lapping is not possible, other machining processes such as grinding, spot facing, milling, turning, etc., can produce acceptably flat mounting surfaces. It is also important to provide a stiff mechanical connection between the sensor and the source of vibration. Metal sheet or plastic parts and other thin and flexible components are not appropriate for accelerometer mounting.

To monitor the vibrations, the sensors are connected to the already in the acquisition system existing vibration monitor M12, shown in Fig. 5.53.

The cables are lead along the hub in order to prevent from touching the rotating shaft and fed through existing holes in the impeller shroud in as shown in Fig. 5.54 and 5.55.

Fig. 5.53 Already existing rack-mounted M12 Module.

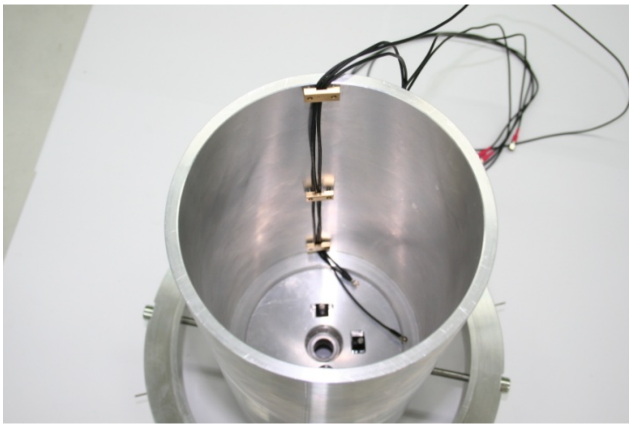

Fig. 5.54 Cable Run along the Hub.

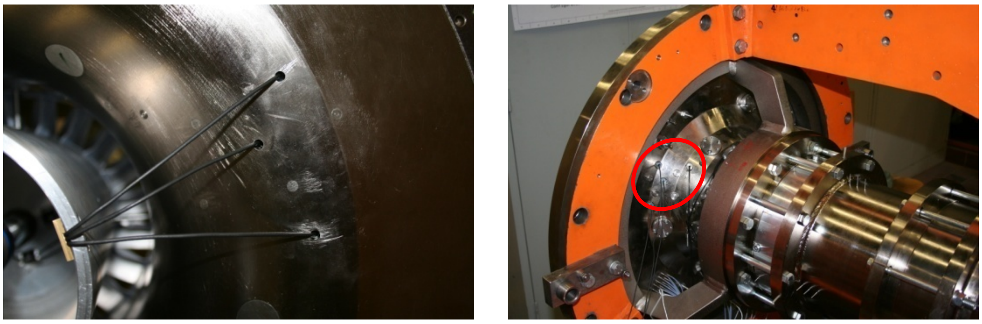

Fig. 5.55 The Three Cables are lead along the Hub and fed through existing Holes in the Impeller Shroud.

5.6 Testing

The subject of this section is to present the first experimental results and mainly to highlight the problems faced during testing.

The first test run was dedicated to slowly warm up the bearings, prior to the high speed operation. This procedure is strongly recommended by the bearing manufacturer in order to allow the grease to achieve its appropriate viscosity and therefore prevent the bearings from damage. During this warming up procedure, the correct rig functionality is checked while keeping an eye on the accelerometer signals. The three sensors showed at all rotational speeds a distinct peak at the angular frequency of the shaft. It is assumed to be a result of an existing unbalance in the system.
At relatively low speeds, the compressor seems to perform well. Therefore, the warming up procedure is continued and the first two speed lines are measured at 10'000 and 12'000 RPM. The stall condition is detected by four down stream installed fast response pressure sensors. In Fig. 5.56, only the measured speed line at 12'000 RPM is compared with CFD. The measured speed line at 10'000 RPM is not shown at this point, since the flow is not stable at all at this relatively low speed. The measured speed line shows the same trend as predicted by CFD, but is shifted towards lower mass flow rates. The choking condition is not captured at all. A possible explanation is that the flow chokes somewhere else in the facility at these relatively low speeds.

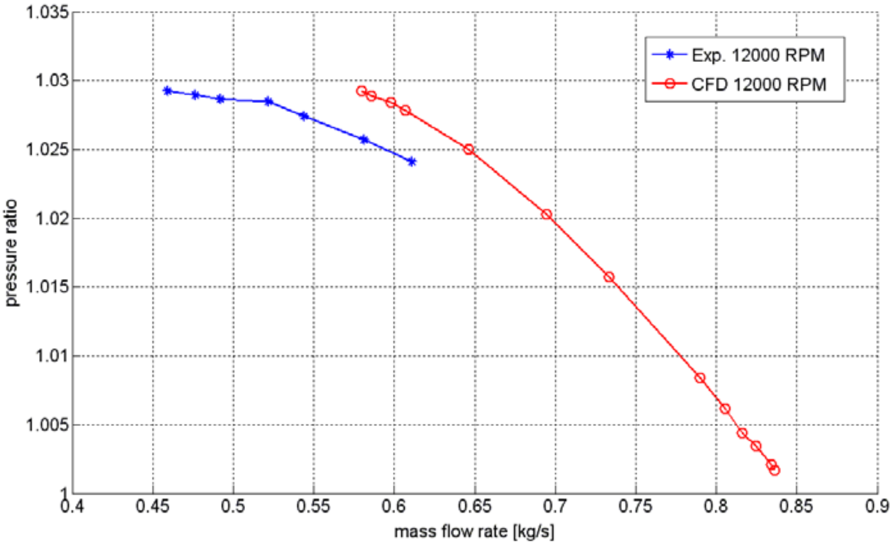

Fig. 5.56 Speed Line at 12'000 RPM: Comparison of Measurements with CFD.

While attempting to reach a rotational speed of 14’000 RPM, the blades started to touch the casing and hence the testing is stopped. A closer look at the blades and the casing emphasis this. The blades did indeed touch the casing.

The rotor stress analysis at design speed discussed in chapter 4.5 predicts a deformation of 0.0498 mm. Compared to the designed tip clearance (1 % of blade span), this is less than 14.7 %. It turned out to be a result of several effects:

- While assembling, it could be observed, that the tip clearance is not uniform, varying within ±0.075 mm. This is on the one hand because of a non-uniform blade length, and on the other hand, a result of the loose fitting seen between the rings during assembling the measurement section. Therefore the stator outer ring is centred as good as possible using shims in the rotor tip gap. But nevertheless, it seems that the weight of 478 kg of the entire measurement section, leading to a slight movement of the rings, due to the clearance, probably during the assembly lifting process by the crane. This can explain why the scratching mainly has happened on one location of the casing.

- Another reason can be the radial clearance of the bearings. This also leads to a tip clearance decrease. This effect actually would go hand in hand with the misalignment of the two shafts, where probably the full capacity of the bearing clearance is used.

5.6.1 Casing Modification

In order to avoid the blades to scratch the metal of the casing and to keep a minimal tip clearance, an abradable layer out of wax is placed in the casing around the rotor blades. First, the properties of the beeswax available in the lab are tested on grooved metal parts and a strategy for manufacturing the abradable layer is mapped out. The wax turned out to have excellent properties to do the job. It is easy to obtain a groove filled with homogenous wax and it is very difficult to scratch the entire or parts of the wax at once off the groove. Instead, swarf similar structures are removed, exactly as desired. Like this, the wax can also be machined, which was also successfully tested on a turning lathe.

A groove as shown in Fig. 5.57 is machined into the casing surrounding the rotor. It is not just a simple rectangular channel, it contains additional slots, to allow the wax, which is ideally a uniform mass, to stick hard to the metal and to prevent the wax from falling off.

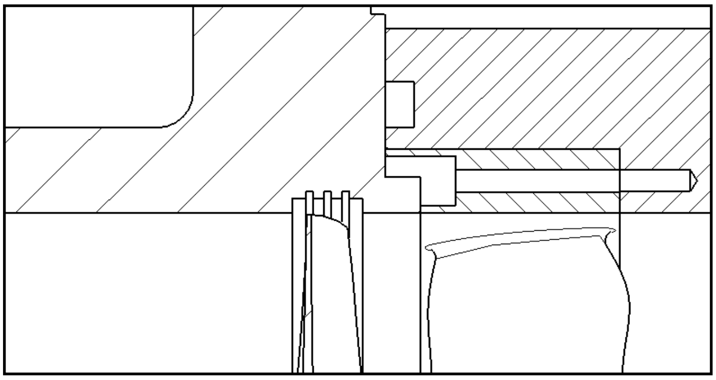

Fig. 5.57 A Groove for a Wax Layer is machined into the Rotor Casing.

Fig. 5.58 shows the casing with the channel filled with wax. It looks like a series of wax nuggets. The reason for this is the way the hot wax is filled into the channel. It must be done gradually in order to obtain a good homogeneity. Wax is filled at one location until overflow. Then a waiting time of about 30 seconds is necessary before turning the casing a few degrees to add again more melted wax. While filling in hot wax at the new location, the layer inside the channel at the interface to the neighbouring location gets melted again and mixes with the new filled in wax. This procedure is continued until the entire groove is filled with wax, leading to a homogeneous distribution.

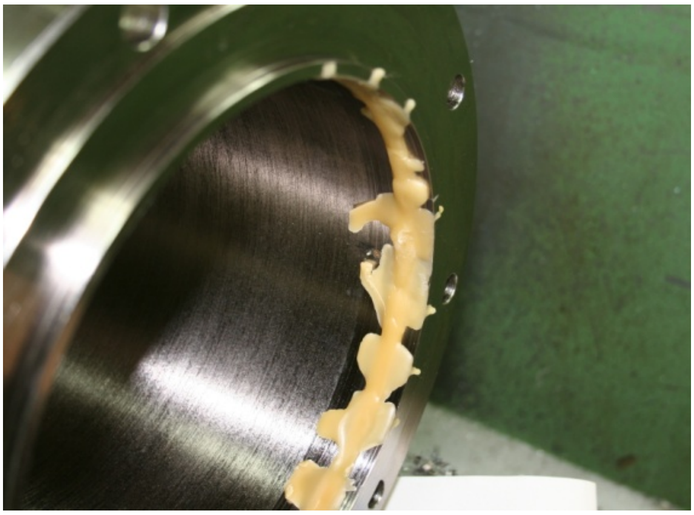

Fig. 5.58 The Groove is filled bit by bit with Wax.

The next step is to remove the overflowed wax. To do so, the casing is installed on a turning lathe and the wax is turned down with a very high accuracy. Only 0.1

mm is turned at once with constant feed motion. This prevents the wax from falling off the channel and gives nice swarf (Fig. 5.59).

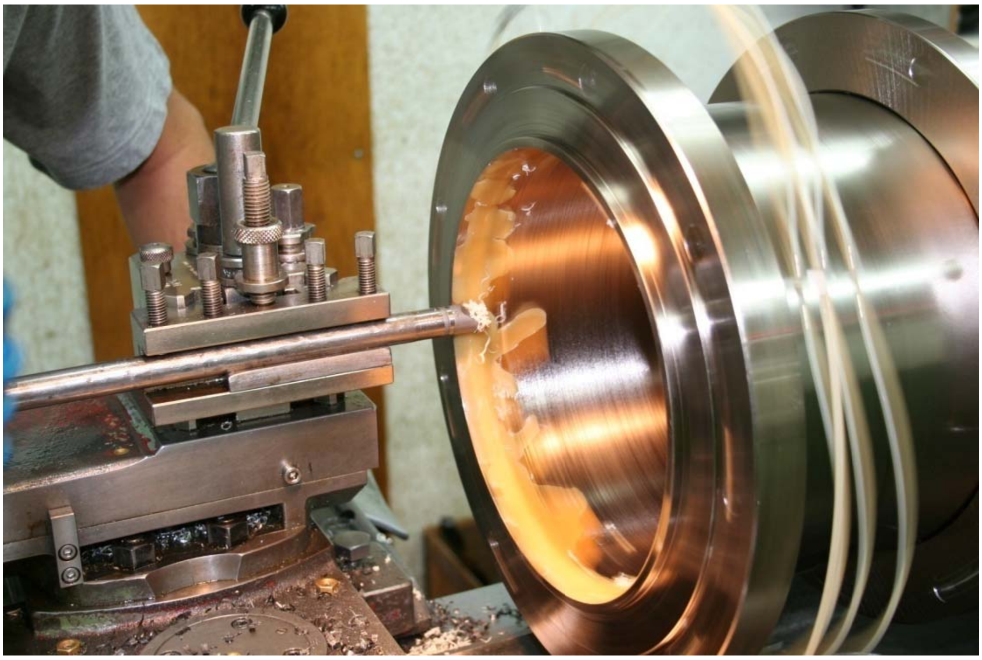

Fig. 5.59 The unnecessary Wax is turned down the Casing Diameter.

Fig. 5.60 Successful Integration of an Abradable Wax Layer into the Rotor Casing.

Fig. 5.60 shows the casing with the homogeneous abradable wax layer as designed. The rotor blades can therefore touch the wax without getting damaged, so the tip gap can be kept as small as possible.

While the wax layer protects the blades from probable damages, it is still not ideal to have the blades touching the casing, since this means the blades undergo a deflection of the size of the tip gap. It is obvious that the main reasons stem from the loose fitting between the several rings and the misalignment of the two shafts. The latter can only be corrected by shaft alignment. But the loose fittings between the rings must be accepted and lived with, except for the fitting given by the stator outer ring. There the fitting was not satisfying, which caused some of the stator blades to brake near the tip. The reason for this is the way the stator ring is screwed to the two rings. On purpose, a gap of 0.5 mm is left between the stator ring and the surround stator outer ring, in order to prevent any assembling problem. It turned out to be not an ideal design. Although the rapid prototyped stator blisk edge is giving the right fitting, it is still a weak material, compared to the stainless steel of the subsequent rings. It happened that these rings pressed with their heavy weight on the stator edge. Obviously, due to the 0.5 mm gap between the stator and the wall, the stator blisk gets deformed and therefore cracks in the blades occurred, causing some of them to brake. Therefore, the geometry of the stator ring is changed in order to prevent any play between the two rings. But this results in each case in a long manual finishing of the stator blisk, until it fits and can be screwed to the two rings. The reason for this is the non-uniform diameter of the stator ring, since the four struts are causing it to deform at their area of attack. These changes are only implemented in the stator ring out of the transparent material, which resulted into an excellent fit for the subsequent ring. The fitting problem still existed as long as the tests were performed with the blue stator ring, but it could be more or less fixed, by very tight fastening of the bolts that are fixing the several rings together.

5.6.2 Bearing Failure

After the abradable wax layer is added in the casing around the rotor and the rotor centred as good as possible, a second test run is started. Again, the same bearing warming up procedure is followed. The rotational speed of 14’000 RPM is achieved without any occurring problems. The compressor worked very nicely and the accelerometers showed a distinct peak the angular frequency of the shaft that did not exceed 8g. After a couple minutes, suddenly a bang could be heard and immediately all the vibrations were gone. It was obvious that the bearings must have failed. It seemed that they had to undergo huge forces and suddenly they have given up, failed and rotated freely. This explains the disappeared vibrations measured by all three accelerometers. Hence, the test run was stopped again. The bearings failed and the compressor was disassembled again.

Fig. 5.61 The failed Bearings still inside the Stator Inner Ring.

Fig. 5.61 shows the bearings still inside the stator inner ring. Sooty particles are covering the bearings and the colour of the bearing inner ring is turned into brown. It seems that, the steel reached temperatures around 260°C. Fig. 5.62a gives insight to the contact area between the two bearings. There the same inner ring as before is partially blue and partially brown. This perhaps means that at this location, the steel has reached temperatures up to 300°C. The other bearing didn't show any colour changes and was also totally intact, not like the colourful one.

Fig. 5.62b shows the damaged bearing from inside. It can be seen that the cage is totally deformed and almost one chunk. Even the balls are charred. The pictures have been sent to SKF to determine the reason for the failure. But unfortunately, the bearing condition did not allow any conclusions to be made. The high temperatures are assumed to be a result of the cage deformation and the involved friction at 14'000 RPM and not a result from the forces acting on the bearings.

Fig. 5.62 Failed Bearings after Disassembling: a) Contact Surface b) Bearings from inside.

At least the abradable wax layer performed very well. Fig. 5.63 shows a swarf at a blade tip after disassembling, exactly as desired. The wax channel was no further harmed and showed excellent properties.

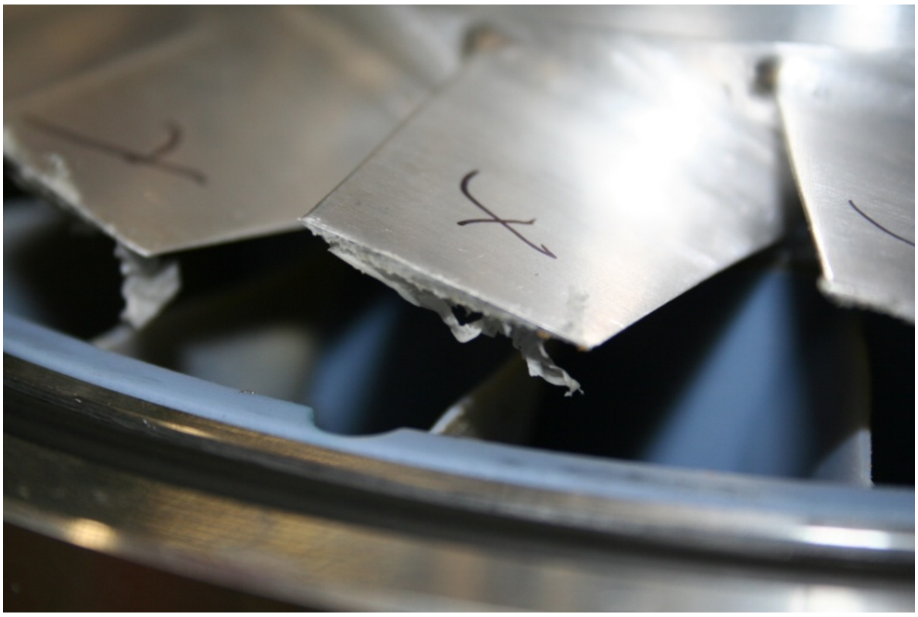

Fig. 5.63 Successful Abradable Layer Functionality: As desired, only swarfs can be found at blade tip.

Although the blades were indeed protected from being damaged and the tip clearance was kept minimal, still the rotor tip deflection is big enough, causing the blades to touch the abradable wax layer.

After analyzing the bearing damage and the possible forces that could have been acting on the bearings and causing them to fail, only one scenario could be thought of: the two shafts are misaligned. This assumption cannot be approved since the current test rig design does not allow any alignment verifications to be made.

It has been realized, that the impeller shroud - hence the entire measurement section frame - is aligned relatively to the impeller sitting on the shaft with an accuracy of 0.2 mm. Already such a misalignment is fatal and can never be compensated by the coupling. Finally, no statement can be made about the misalignment. It can be less or even much more than 0.2 mm.

Before attempting to align the shaft or doing any major design modifications, a different bearing type is tried in a third test run. This time only one self-aligning ball bearing of the type SKF 1202 ETN9 with a grease of the type LGWA 2/0.4 as shown in Fig. 5.64 is used. The design of self-aligning ball bearings is such that angular misalignment between the outer and the inner rings can be accommodated without any negative effect on bearing performance. To do so a new bearing fixation flange was machined and the bore hole of the stator inner ring enlarged.

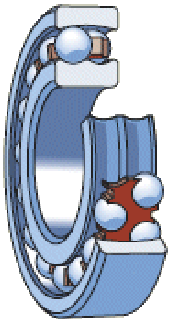

Fig. 5.64 Ball Bearing of the Type SKF 1202 ETN9.

The third test with the new bearing configuration (Fig. 5.65) is not successful at all. Already at low speeds the rotor is very noisy, the vibration levels are high and a lot of frequencies are stimulated simultaneously, no longer only one distinct peak at the angular frequency of the shaft. Also, the cone is warm after stopping the test run.

Shaft alignment is therefore unavoidable and necessary before running any further tests.

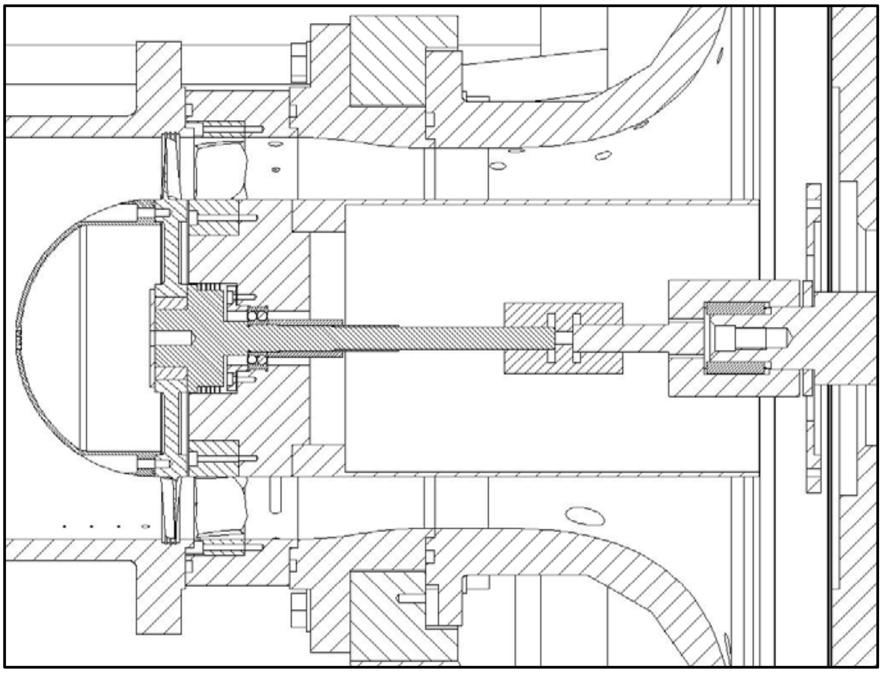

Fig. 5.65 Axial Compressor Configuration with one self-aligning ball bearing of the type SKF 1202 ETN9 supporting the shaft.

Chapter 6

Summary and Conclusions

A high through-flow fan with a low pressure ratio for a high altitude application is designed and tested. This fan is supposed to be working continuously at 21 km providing a pressure ratio of 1.01 to 1.05 at a volume flow rate of 6 to 7.5 m^3/s equivalent to mass flow rate of about 0.6 kg/s. Due to the low density of air (0.08 kg/m^3) at high altitude (21'000 km), the fan would be operating at relatively low Reynolds number ($3.88 \cdot 10^5$).

In a first step a fan inlet duct is designed in order to benefit from an existing wind (7 – 40 m/s) at high altitudes. Starting from a cylindrical tube that turns the flow, the optimizations lead us to a kidney-shaped fan inlet duct. This design greatly reduces the flow separation and a much more uniform exit flow can be provided.
The optimized duct generates a total pressure loss of 2.3 Pa compared to the preliminary design, where 4.6 Pa are lost. Therefore, with the advanced design, the initial pressure loss is reduced by more than 50%. At first sight, 4.6 Pa of total pressure loss are almost nothing compared to common compressor applications. But since the design pressure ratio of the fan is only 1.02 and the ambient pressure at 21'000 km altitude is only 5'000 Pa, only a pressure increase of 100 Pa is achieved. Here, a total pressure loss of 4.6 Pa makes 4.6 % of the pressure increase and has therefore to be considered and tried to be minimized, since the compressor underlies a power limitation set by the battery equipment of the airship, which does not allow to draw more energy to run the compressor at its design point, while accepting the efficiency loss resulting from the wind.

A general turbomachinery design always starts with a zero-dimensional analysis where the fan characteristics are specified. In addition to pressure ratio and mass flow rate, the fan needs to operate at a low input power (about 1 kW) and is supposed to be as light as possible with an external diameter of 60 cm, due to structure limitations. The fan has only one single stage (rotor and stator blades) due to its relatively low pressure ratio and in order to minimize the costs, complexity and weight. The next design step is the 1-D meanline design. The forced vortex approach has been applied for rotor blade preliminary design while free vortex design has been used for stator blade. The fan characteristics including the degree of reaction, diffusion factor, etc. have been all designed to be within the accepted range. After computing the flow angles, a NACA profile is chosen and the meanline design is continued by calculating the angles at the blade hub and tip. In a next design step, 2-D design, a commercial tool (AXCAD) is applied to create the full rotor/stator blade geometry. The blades are defined by several cross-sections, mainly at hub, 25 %, 50, %, 75 % of span and at tip. In between, the cross-sections are interpolated.

Based on the existing 2-D design of a one stage axial fan, the design is validated and further optimized using CFD. While the rotor flow field looks fine, the stator needs to be modified in order to reduce the separations at hub and tip as well as to reduce losses. By changing the incidence and stagger angle at hub and tip and by applying a lean and a sweep to the stator blades, the hub corner separation can be significantly suppressed and the tip separation is reduced. A compressor characteristic (compressor map) for both, the original and optimized design is computed in order to compare the CFD designs together and with experiments. With the optimized stator row, the stall condition is shifted to a higher pressure ratio and lower mass flow rate and therefore the stall margin is enhanced. At the design speed (7000 RPM), a pressure ratio up to 1.08 can be achieved before the compressor stalls. Compared to the stall condition of the original design at a pressure ratio of about 1.06, this gives an increase of 33 % equivalent to 100 Pa pressure rise. The stall margin is 3.9 % for the original design and 19.53 % for the optimized design. Hence, the stall margin is considerably improved by 15.63 %.

Additionally to the aerodynamic analysis, a rotor blisk structure and vibration analysis are performed to guarantee the mechanical integrity during operation at high altitude and also during testing with a model. In the case of the high altitude fan, the maximal occurring von Mises stress at design rotational speed (7'000 RPM) is $\sigma_{vmax} = 7.123 \cdot 10^7$ Pa, leading to a safety factor of 4.733. The maximal occurring von Mises stress in the scaled model at 25'000 RPM is $\sigma_{vmax} = 1.216 \cdot 10^8$ Pa. Hence, even at a rotational speed of 25'000 RPM, which is 14% higher than the design speed of 22'000 RPM, a safety factor of 3.45 is guaranteed.

The maximal operating speed range is 116.7 Hz for the high altitude fan and 366.7 Hz for the scaled down model. For both cases, the vibration analysis shows that the first six, and hence all further eigenfrequencies are located considerably above the maximal operating speed range and cannot be excited during operation.

Together with the CFD analysis, this is the base for the subsequent manufacturing of a model to validate the fan design.

A scaled down model of the axial fan is manufactured and integrated for testing into an already existing radial compressor test rig facility (*RIGI*) at the turbomachinery laboratory (ETH Zurich). All necessary measurement facilities are already offered by *RIGI* and therefore only a set of accelerometers are additionally installed. Most of the parts are manufactured in the LSM workshop. Only the rotor and stator blisk as well as the cone and some features are manufactured externally. An economic way to manufacture the stator blisk is rapid prototyping. The manufacturing time is reduced to only maximum one day instead of two months (aluminium), as it can be ordered next door in the Institute of Robotics and Intelligent Systems. The other advantage is the reduced cost. The cost of such a blisk is about a tenth of the one made of aluminium. This way, flexibility and a compressed design-to-manufacturing cycle is achieved. Therefore, instead of having a full stator blisk attached to the casing and aligning the shaft, a replaceable rapid prototyped stator blisk is screwed to an aluminium inner and outer ring, which are already concentrically aligned to each other by four struts. Like this, only the struts are carrying all the weight and the stator blisk is automatically aligned by fitting. The bearings supporting the shaft are located inside the stator inner ring.

The shaft is machined out of stainless steel containing several features and therefore undergoes a long manufacturing process. The rotor is shrunk on the shaft and fixed axially. The shrink fit doesn't allow any relative motion between the shaft and the rotor blisk up to a rotational speed of 26'500 RPM, which affects the balance positively. The cooling holes in the shaft and in the cone as well as the labyrinth sealing machined into the shaft are considered for ventilation in order to cool the bearings. This is possible due to pressure equalization through the hub from the high pressure region behind the stator and the inlet of the compressor. Due to the design of *RIGI* and the existing limited accessibility, the length of the hub cannot be extended to the housing of *RIGI*. The air is pushed through the bearings, then through the holes in the shaft and finally injected into the compressor inlet flow through the holes in the cone. Like this, there is almost no leakage flow occurring between the rotor and stator that would negatively impact the system efficiency.

The shaft is with 22.3 cm very long. To avoid overhang effects, the bearings are located as near as possible to the rotor blisk. A pair of SKF 6202-2Z Explorer single row, deep groove ball bearings with an inner diameter of 15 mm is supporting the shaft.

Two speed lines are measured for 10'000 and 12'000 RPM. The operation at 10'000 RPM is not stable, probably due to the relatively low rotational speed (design speed for scaled model is 22'000 RPM). At 12'000 RPM the operation is stable and the pressure ratios predicted by CFD are captured, but at lower mass flow rates. While attempting to reach 14'000 RPM, the bearings suddenly fail. The root cause is found to be a misalignment between the two shafts. A further attempt is in progress to achieve a full alignment of shafts.

The current work is the first attempt to integrate an axial fan or compressor into the existing test rig *RIGI*, already used for centrifugal compressors. As a starting point, results of the current work indicate that *RIGI* test facilities can be also used for axial fan and compressor testing purposes.

Chapter 7

Future Work

The scale down model testing was failed at rotational speeds higher than 12’000 RPM. This is believed to be due to the misalignment of the shaft and overloading of the bearings. Even using a Self-Aligning Roller Bearing did not help to fix the problem. As a result, to run the designed axial fan at higher rotational speed, a sufficient alignment is quite critical and needs to be considered. Using a stronger coupling and bearing is also recommended.

As already discussed in chapter of manufacturing and testing, the current design of the test rig facilities allows a radial traverse measurement upstream and downstream of the compressor stage using FRAP technology. Therefore, there is a possibility to provide more data regarding the flow behaviour through the stage, which can be used for further numerical and optimization studies.

The current work is the first attempt to integrate an axial fan or compressor into the existing test rig *RIGI*, already used for centrifugal compressors. As a starting point, results of the current work indicate that *RIGI* test facilities can be also used for axial fan and compressor testing purposes.

Chapter 8

References

Abhari, R.S., Prof. Dr., Lecture Notes *Turbomachinery Design*, WS 2005/2006 ETH Zurich.

Abhari, R.S., Prof. Dr., Lecture Notes *Aerospace Propulsion*, SS 2006 ETH Zurich.

Abhari, R.S., Prof. Dr., **Wettstein** H.E., *Gas Turbine Mechanics and Design*, SS 2006 ETH Zurich.

Angst + Pfister, *Gesamtkatalog*, 2007.

ANSYS Europe Ltd., *User Guide*, 2007.

Beheshti, B. H., **Teixeira**, J. A., **Ivey**, P. C., **Ghorbanian**, K., **Farhanieh**, B., *Parametric Study of Tip Clearance - Casing Treatment on Performance and Stability of a Transonic Axial Compressor*, ASME Journal of Turbomachinery, Vol. 126, pp. 527–535, 2004.

Bossard, *Gesamtkatalog*, 2007.

Cameron, J. D., **Gendrich**, C. P., **Morris** S. C., **Corke**, T. C., *A Transonic Axial Compressor Facility for Fundamental Research and Flow Control Development*, AIAA Aerospace Sciences Meeting and Exhibit, 9 - 12 January 2006, Reno, Nevada

Cumpsty, N. A., *Compressor Aerodynamics*, 2004.

Dixon, S.L., *Fluid Mechanics, Thermodynamics of Turbomachinery*, 1998.

Dubbel, *Taschenbuch für den Maschinenbau*, 21. Auflage, 2005.

Gontsov, N. G., **Marinova**, O. A., **Tananaev**, A. V., *Turbulent Flow around a Bend in a Circular Pipe,* Power Technology and Engineering, Vol. 18, No. 12, pp. 596 - 602, 1984.

Gossweiler, C., *On Probes and Measuring Techniques for Fast- Response Flow Measurement Using Piezo-Resistive Pressure Transducers*, PhD Thesis ETH Nr. 10253, 1993.

Grotjans, H., **Menter**, F.R., *Wall functions for general application CFD codes*, 1998

Horlock, J.H., *Axial Flow Compressors,* 1958.

INA, *Technisches Taschenbuch*, 2007.

Johannsen AG, *Katalog-Nr. 7.0*, 2007.

Kerrebrock, J.L., *Aircraft Engines and Gas Turbines*, 1992.

Kleiser, L., Lecture Notes *Turbulent Flows*, WS 2005/2006 ETH Zurich.

Launder, B.E., **Spalding**, D.B., *The numerical computation of turbulent flows*, 1974.

Lakshminarayana, B., Fluid Dynamics and Heat Transfer of Turbomachinery, 1995.

SKF, *Hauptkatalog*, Publikation Nr. 5000, 2007

Sörgel, G., *Grundlagen der Turbomaschinen, Lehrheft 1&3,*Technische Universität Dresden, 19xx.

Appendix

Calculation of Rotor-Shaft Shrink Fit

```
delta_R=30*10^(-6); %Passung

R20=0.020;
R77=0.077;

ausdehn_koeff=23.4*10^(-6);              % HABA-50: www.haba.ch
T0=23;
Ealu=7*10^10;
Estahl=21.5*10^10;
alpha_alu=1127;
alpha_stahl=3217;
beta_alu=682;
beta_stahl=1852;
valu=0.34;
vstahl=0.3;

p=1;
for t=0:100:27000
   N(p,1)=t;
   p=p+1;
end

[m,n]=size(N);

for i=1:m
   omega=N(i)*2*pi/60;
   A=[1, 1/R20^2, -1; 1, 1/R77^2, 0; R20/Ealu*(1 - valu), -1/(Ealu*R20)*(1 + valu), -
1*R20/Estahl*(1 - vstahl)];
   b=[(alpha_alu-alpha_stahl)*omega^2*R20^2; alpha_alu*omega^2*R77^2;
delta_R + omega^2*R20^2*(R20/Estahl*(vstahl*alpha_stahl-beta_stahl)-
R20/Ealu*(valu*alpha_alu-beta_alu))];
```

```
    x=A^(-1)*b;

    sigma_r_w=x(3,1) - alpha_stahl*omega^2*R20^2;
    sigma_phi_w=x(3,1) - beta_stahl*omega^2*R20^2;
    sigma_r_s=x(1,1)+ x(2,1)/R20^2 - alpha_alu*omega^2*R20^2;
    sigma_phi_s=x(1,1)- x(2,1)/R20^2 - beta_alu*omega^2*R20^2;
    u_w=R20/Estahl*(sigma_phi_w-vstahl*sigma_r_w);
    u_s=R20/Ealu*(sigma_phi_s-valu*sigma_r_s);

    data(i,1)=sigma_r_w;
    data(i,2)=u_w;
    data(i,3)=u_s;
    data(i,4)=sigma_phi_w;
    data(i,5)=sigma_r_s;
    data(i,6)=sigma_phi_s;

end

Fuegetemp=T0+(2*delta_R+2*R20/1000)/(ausdehn_koeff*(2*R20-0.35*10^(-6)));

%% Create axes
axes1 = axes('FontSize',14);
title(axes1,'\it{normal stress for press fit}');
xlabel(axes1,'RPM');
ylabel(axes1,'normal stress    \sigma_r');
hold(axes1,'all');

%% Create plot
plot1=plot(N,data(:,1),'LineWidth',2);
text1=text(3000,-2*10^7,['Assembly Temperature = ',num2str(Fuegetemp),'
°C'],'FontSize',14);
text1=text(3000,-2.5*10^7,['delta R = ',num2str(delta_R),' m'],'FontSize',14);
```

Calculation of Labyrinth Sealing

```
Dsp=60/1000; % [m]
C=0.6;
delta2=C*Dsp/1000+0.00025; % [mm]
delta=0.5/1000; % [m]
t=2.5/1000; % [m]
```

```
dicke=0.5/1000; % [m]
z=5;

k_ue=1.75;
mue_sp=0.745;

Asp=pi*Dsp*delta;

pr=1.05;
p1=1.01325*10^5;
p2=p1*pr;
rho1=1.204;

msp=k_ue*mue_sp*Asp*sqrt((p2^2-p1^2)/(z*p2*(1/rho1)));
```

Calculation of Scaling Analysis

```
scale=[1,2,2.676,3,4,5,6,7,8,9,10,11,12,13,14,15]';
[m,n]=size(scale);

r_ht=0.69;      % hub to tip ratio
ro1=0.3;
ri1=ro1*r_ht;
rm1=(ro1+ri1)/2;

u1tip=219.9115;      % ATTENTION!!!!!!!!!!!! THIS GIVES a N1 of 7000 RPM !!!!!!!!!!
N1=u1tip/(2*pi*ro1)*60;

nc=0.7;
np=nc;          % compressor efficiency=isentropic efficiency=polytropic efficiency
p1=5000;
pr=1.05;          % pressure ratio
deltap=pr*p1-p1;     % [Pa]

m1=0.6;
R=287;
A1=pi*(ro1^2-ri1^2);
gamma=1.4;
T01=216.69; %273.15-56.46;
```

```
a=m1*sqrt(R*T01)/(p1*A1*sqrt(gamma));
b=(gamma-1)/2;
i=1;
Max(i)=0;
delta(i)=1;

while (delta(i)>10e-10 || delta(i)<-10e-10)
  i=i+1;
  Max(i)=a*(1+b*Max(i-1)^2)^(-0.5);
  delta(i)=Max(i)-a/sqrt(1+b*Max(i)^2);
end

k=1;
Mau(k)=0;
delta(k)=1;

while (delta(k)>10e-10 || delta(k)<-10e-10)
  k=k+1;
  Mau(k)=2*pi*N1*rm1*(1+(gamma-1)/2*Mau(k-1))^(0.5)/(60*sqrt(gamma*R*T01));
  delta(k)=Mau(k)-2*pi*N1*rm1*(1+(gamma-
1)/2*Mau(k))^(0.5)/(60*sqrt(gamma*R*T01));
end

R=287;
p2=100000;
T021=293.15; %273.15+20;
gamma=1.4;
cp=1005;

h1=21500;                 % height [m]
T01=216.69;                % free stream temperature [K]: -56.46°C
                      % constant for h>11km
Ts=110.4;
Tref=273.15;              % reference temperature [K]
muref=1.716e-005;              % reference dynamic viscosity [Kg/ms]

mu1=muref*(T01/Tref)^(3/2)*((Tref+Ts)/(T01+Ts));     % dynamic viscosity [kg/ms]
mu2=1.827e-005;

rho1=p1/1000/(0.2869*((T01-273.15)+273.1));           % density [kg/m^3]
rho2=p2/(R*T021);%1.283;

for t=1:1:m
```

```
   ro2(t,1)=ro1/scale(t,1);
   ri2(t,1)=ri1/scale(t,1);
   rm2(t,1)=(ro2(t,1)+ri2(t,1))/2;
   A2(t,1)=pi*((ro2(t,1))^2-(ri2(t,1))^2);

   m2(t,1)=Max(i)/sqrt(R*T021)*p2*A2(t,1)*sqrt(gamma)*sqrt(1+(gamma-
1)/2*Max(i)^2);
   N2(t,1)=Mau(k)/(2*pi*rm2(t,1)*(1+(gamma-
1)/2*Mau(k))^(0.5))*(60*sqrt(gamma*R*T021));

   cx1=m1*R*T01*(1+(gamma-1)/2*Max(i)^2)^(-1)/(p1*A1);
   cx2(t,1)=m2(t,1)*R*T021*(1+(gamma-1)/2*Max(i)^2)^(-1)/(p2*A2(t,1));
% cx2_test=m2(t,1)/rho2/A2(t,1);    %test successfull

   u1=2*pi*N1*rm1/60;
   u2(t,1)=2*pi*N2(t,1)*rm2(t,1)/60;

   v1=sqrt(u1^2+cx1^2);
   v2(t,1)=sqrt(u2(t,1)^2+cx2(t,1)^2);

%     Mau2_test(t,1)=u2(t,1)/sqrt(gamma*R*T021);     % test successfull

   c1=0.0713;    % chord
   c2(t,1)=c1/scale(t,1);    % chord

   Re1=rho1*c1*v1/mu1;                          % Reynolds number
   Re2(t,1)=rho2*c2(t,1)*v2(t,1)/mu2;

   P1spec=cp*T01/nc*(pr^((gamma-1)/gamma)-1);
   P2spec(t,1)=cp*T021/nc*(pr^((gamma-1)/gamma)-1);

   pr_new=(T01/T021*(pr^((gamma-1)/gamma)-1)+1)^(gamma/(gamma-1));
   deltap_new=p2*(pr_new-1);

   P2spec_new(t,1)=cp*T021/nc*(pr_new^((gamma-1)/gamma)-1);

   P1=cp*T01/nc*(pr^((gamma-1)/gamma)-1)*m1;
   P2(t,1)=cp*T021/nc*(pr^((gamma-1)/gamma)-1)*m2(t,1);
   P2_new(t,1)=cp*T021/nc*(pr_new^((gamma-1)/gamma)-1)*m2(t,1);

   % Drehmoment Berechnung, basierend auf Buch Kerrebrock S. 280

   rm11=rm1;
   rm12=rm1;
```

```
   rm21(t,1)=rm2(t,1);
   rm22(t,1)=rm2(t,1);

   beta11=atand(u1/cx1);
   beta12(t,1)=atand(u2(t,1)/cx2(t,1));
   Ctheta11=0;  %axial inlet flow
   Ctheta12(t,1)=0;  %axial inlet flow
   Ctheta21=T01*cp/u1*(pr^(((gamma-1)/gamma)*(1/np))-1);
   Ctheta22(t,1)=T021*cp/u2(t,1)*(pr^(((gamma-1)/gamma)*(1/np))-1);
   % here pr has been used, since pr_new gives a different value for beta22
   % compared to beta2 that means that the pressure ratio must remain constant
   % to have thesame blade geometry

   beta21=atand((u1-Ctheta21)/cx1);
   beta22(t,1)=atand((u2(t,1)-Ctheta22(t,1))/cx2(t,1));

% Drehmoment Welle [Nm]
   Mn1=m1*[rm12*Ctheta21-rm11*Ctheta11];   %Drehmoment auf Welle [Nm]
   Mn2(t,1)=m2(t,1)*[rm22(t,1)*Ctheta22(t,1)-rm21(t,1)*Ctheta12(t,1)];

   P_shaft1=2*pi*N1/60*Mn1;
   P_shaft2(t,1)=2*pi*N2(t,1)/60*Mn2(t,1);

   P1euler=m1*u1*Ctheta21;
   P2euler(t,1)=m2(t,1)*u2(t,1)*Ctheta22(t,1);

   Ctheta22_output1(t,1)=P2(t,1)/(2*pi*N2(t,1)/60)/(m2(t,1)*rm2(t,1));
   beta22_output1(t,1)=atand((u2(t,1)-Ctheta22_output1(t,1))/cx2(t,1));

   Ctheta22_output2(t,1)=P2_new(t,1)/(2*pi*N2(t,1)/60)/(m2(t,1)*rm2(t,1));
   beta22_output2(t,1)=atand((u2(t,1)-Ctheta22_output2(t,1))/cx2(t,1));

   data1(t,1)=2*ro1;                       data1(t,13)=Mn1;
   data1(t,2)=2*ri1;                       data1(t,14)=P_shaft1;
   data1(t,3)=N1;                          data1(t,15)=P1euler;
   data1(t,4)=Re1;
   data1(t,5)=m1;                          data2(t,1)=scale(t,1);
   data1(t,6)=cx1;                         data2(t,2)=2*ro2(t,1);
   data1(t,7)=u1;                          data2(t,3)=2*ri2(t,1);
   data1(t,8)=v1;                          data2(t,4)=N2(t,1);
   data1(t,9)=beta11;                      data2(t,5)=Re2(t,1);
   data1(t,10)=beta21;                     data2(t,6)=m2(t,1);
   data1(t,11)=P1;                         data2(t,7)=cx2(t,1);
   data1(t,12)=P1spec;                     data2(t,8)=u2(t,1);
```

```
    data2(t,9)=v2(t,1);
    data2(t,10)=beta12(t,1);
    data2(t,11)=beta22(t,1);
    data2(t,12)=beta22_output1(t,1);
    data2(t,13)=beta22_output2(t,1);
    data2(t,14)=P2(t,1);
    data2(t,15)=P2_new(t,1);
    data2(t,16)=P2spec(t,1);
    data2(t,17)=P2spec_new(t,1);
    data2(t,18)=Mn2(t,1);
    data2(t,19)=P_shaft2(t,1);
    data2(t,20)=P2euler(t,1);
end
```

Calculation Blade Thickness distribution

```
rht=0.69;
dtip=0.003;              % Parameters to be entered %
dhub=0.009;
rt=0.3;

rh=rt*rht;
rm=(rh+rt)/2;

rRigi=0.224/2;
scale=rt/rRigi;

% r=A+B/(d/2)^2

yp1=rt-rt*rht;
xp1=dtip/2;
yp2=0;
xp2=dhub/2;
ypm=rm-rh;

y1_00=0*yp1;
y1_05=0.05*yp1;
y1_10=0.10*yp1;
y1_25=0.25*yp1;
y1_50=0.50*yp1;
y1_75=0.75*yp1;
y1_100=1*yp1;

B=xp2^2*xp1^2*(yp2-yp1)/(xp1^2-xp2^2);
A=yp1-B/xp1^2;

n=0;
```

```
for d=dtip:0.0001:dhub;

   n=n+1;
   r1(n)=A+B/((d/2)^2);
   x1(n)=d/2;
end

dmean=2*sqrt(B/(ypm-A));
d1_00=2*sqrt(B/(y1_00-A));
d1_05=2*sqrt(B/(y1_05-A));
d1_10=2*sqrt(B/(y1_10-A));
d1_25=2*sqrt(B/(y1_25-A));
d1_50=2*sqrt(B/(y1_50-A));
d1_75=2*sqrt(B/(y1_75-A));
d1_100=2*sqrt(B/(y1_100-A));

d1(1,2)=d1_00;                              d1(1,1)=0.0;
d1(2,2)=d1_05;                              d1(2,1)=0.05;
d1(3,2)=d1_10;                              d1(3,1)=0.10;
d1(4,2)=d1_25;                              d1(4,1)=0.25;
d1(5,2)=d1_50;                              d1(5,1)=0.50;
d1(6,2)=d1_75;                              d1(6,1)=0.75;
d1(7,2)=d1_100;                             d1(7,1)=1;


% Computation for scaled down model
dtip2=dtip/scale;
dhub2=dhub/scale;
rt2=rt/scale;
rh2=rt2*rht;
rm2=(rh2+rt2)/2;

yp1=rt2-rt2*rht;
xp1=dtip2/2;
yp2=0;
xp2=dhub2/2;
ypm2=rm2-rh2;

y2_00=0*yp1;
y2_05=0.05*yp1;
y2_10=0.10*yp1;
y2_25=0.25*yp1;
y2_50=0.50*yp1;
y2_75=0.75*yp1;
```

```
y2_100=1*yp1;

B=xp2^2*xp1^2*(yp2-yp1)/(xp1^2-xp2^2);
A=yp1-B/xp1^2;

n=0;
for d=dtip/scale:0.0001:dhub/scale;
   n=n+1;
   r2(n)=A+B/((d/2)^2);
   x2(n)=d/2;
end

dmean2=2*sqrt(B/(ypm2-A));
d2_00=2*sqrt(B/(y2_00-A));
d2_05=2*sqrt(B/(y2_05-A));
d2_10=2*sqrt(B/(y2_10-A));
d2_25=2*sqrt(B/(y2_25-A));
d2_50=2*sqrt(B/(y2_50-A));
d2_75=2*sqrt(B/(y2_75-A));
d2_100=2*sqrt(B/(y2_100-A));

d2(1,2)=d2_00;                          d2(1,1)=0.0;
d2(2,2)=d2_05;                          d2(2,1)=0.05;
d2(3,2)=d2_10;                          d2(3,1)=0.10;
d2(4,2)=d2_25;                          d2(4,1)=0.25;
d2(5,2)=d2_50;                          d2(5,1)=0.50;
d2(6,2)=d2_75;                          d2(6,1)=0.75;
d2(7,2)=d2_100;                         d2(7,1)=1;


% Plotting in [mm]
plot(x1*1000,r1*1000);
hold on;
plot(-x1*1000,r1*1000);
hold on;
plot(x2*1000+20,r2*1000);
hold on;
plot(-x2*1000+20,r2*1000);
```

Calculation Forced Vortex Design

```
pr=1.05;
rht=0.7;
utip=150;
residual=1e-6;
increment=1000;
rt=0.3;
rh=rt*rht;
rm=(rh+rt)/2;

omega=utip/rt;

T01=216.69;
m1=0.6;
gamma=1.4;
cp=1005;
rho=0.08;
A=pi*(rt^2-rh^2);

nc=0.8;
P1=cp*T01/nc*(pr^((gamma-1)/gamma)-1)*m1;

a=P1/(m1*omega*rm^2);%66.25;
cx_av=m1/rho/A;%41.45;

i=1;
k=2285;

  term1(i)=-sqrt(2)/(3*a^2)*(k-a^2*rt^2)^(3/2);
  term2(i)=-sqrt(2)/(3*a^2)*(k-a^2*rh^2)^(3/2);
  integral(i)=term1(i)-term2(i);
  delta(i)=m1/(2*pi*rho)-integral(i);

fertig=false;

while (abs(delta(i))>residual && fertig==false)
  i=i+1;
  counter(i)=i;

  term1(i)=-sqrt(2)/(3*a^2)*(k-a^2*rt^2)^(3/2);
  term2(i)=-sqrt(2)/(3*a^2)*(k-a^2*rh^2)^(3/2);
```

```
  integral(i)=term1(i)-term2(i);
  delta(i)=m1/(2*pi*rho)-integral(i);

  delta6=delta(i);
  integral6=integral(i);

  k=k+1/increment;

  if ((delta(i)/delta(i-1))<0)
    fertig=true;
  end
end

n=0;
for t=rh:0.01:rt
  n=n+1;
  r(n)=t;
  cx(n)=sqrt(2*k-2*a^2*r(n)^2);
  Ctheta(n)=a*r(n);
end

subplot(2,2,1);
plot(r,cx);
subplot(2,2,2);
plot(r,Ctheta);
subplot(2,2,3);
plot(counter,delta);
subplot(2,2,4);
text(0.3,0.8,['utip = ',num2str(utip)]);
text(0.3,0.6,['rht = ',num2str(rht)]);
text(0.3,0.4,['a = ',num2str(a)]);
text(0.3,0.2,['k = ',num2str(k)]);
axis off;
```